

UNIVERSITY OF CALIFORNIA

Los Angeles

Excitation and Nonlinear Evolution of the Modified Simon-Hoh  
Instability in an Electron Beam Produced Plasma Column

A dissertation submitted in partial satisfaction of the  
requirements for the degree  
Doctor of Philosophy in Electrical Engineering

By

Youichi Sakawa

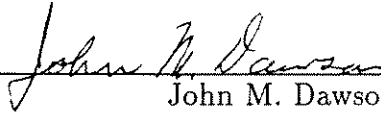
1992

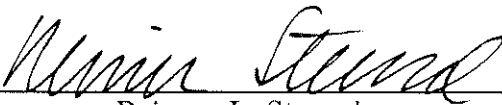
© Copyright by

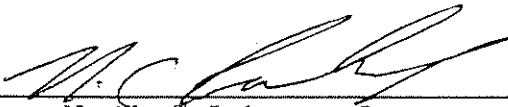
Youichi Sakawa

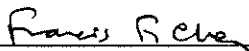
1992

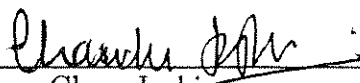
The dissertation of Youichi Sakawa is approved.

  
John M. Dawson

  
Reiner L. Stenzel

  
Neville C. Luhmann, Jr.

  
Francis F. Chen  
Committee Co-Chair

  
Chan Joshi  
Committee Co-Chair

University of California, Los Angeles

1992

This dissertation is dedicated to my wife Sayuri.

# Contents

|   |          |
|---|----------|
| Dedication . . . . .                          | iii      |
| List of Tables . . . . .                      | viii     |
| List of Figures . . . . .                     | xi       |
| Acknowledgements . . . . .                    | xii      |
| Vita . . . . .                                | xiii     |
| Abstract . . . . .                            | xv       |
| <b>1 Introduction</b>                         | <b>1</b> |
| <b>2 Experiments</b>                          | <b>4</b> |
| 2.1 Introduction . . . . .                    | 4        |
| 2.2 Experimental Apparatus . . . . .          | 5        |
| 2.3 DC Parameter Measurements . . . . .       | 8        |
| 2.3.1 Density Measurements . . . . .          | 8        |
| 2.3.2 Plasma Potential Measurements . . . . . | 14       |
| 2.3.3 Temperature Measurements . . . . .      | 16       |
| 2.4 Instability Measurements . . . . .        | 20       |
| 2.5 Wave Propagation Measurements . . . . .   | 30       |

|          |   |           |
|----------|---|-----------|
| 2.6      | Nonlinear Evolution Measurements . . . . .  | 33        |
| <b>3</b> | <b>Theory of the Modified Simon-Hoh Instability</b>                                       | <b>37</b> |
| 3.1      | Introduction . . . . .  | 37        |
| 3.2      | Review of Experimental Observation of Electrostatic Instabilities .                       | 38        |
| 3.3      | Physical Picture of the MSHI . . . . .  | 40        |
| 3.3.1    | Simon-Hoh Instability . . . . .   | 40        |
| 3.3.2    | Modified Simon-Hoh Instability . . . . .  | 42        |
| 3.4      | Fluid Theory of the MSHI . . . . .  | 42        |
| 3.4.1    | General Fluid Theory . . . . .  | 43        |
| 3.4.2    | MSHI Theory . . . . .   | 48        |
| 3.5      | Kinetic Theory of MSHI . . . . .  | 52        |
| 3.5.1    | Ion Cyclotron Oscillation ( $\Omega_i$ ) and Ion $E \times B$ Drift . . . . .             | 54        |
| 3.5.2    | Ion Rattle Oscillation ( $\Omega_R$ ) and $\Omega_i r$ Drift . . . . .                    | 54        |
| 3.6      | Comparison with Other Instabilities . . . . .   | 56        |
| 3.6.1    | Modified Two-stream Instability (MTSI) and Flutelike Drift<br>Instability (FDI) . . . . . | 56        |
| 3.6.2    | Anti-drift Mode . . . . .   | 58        |
| <b>4</b> | <b>Verification of the MSHI</b>   | <b>60</b> |
| 4.1      | Introduction . . . . .  | 60        |
| 4.2      | $v_{\theta i}$ Measurements . . . . .   | 61        |
| 4.3      | Orbit Calculation . . . . .   | 61        |
| 4.4      | Ion Mass Dependence of $f_1$ and $T_{i\perp}$ Measurements . . . . .                      | 66        |
| 4.5      | Finite Ion Larmor Radius Correction of Ion $E \times B$ Drift . . . . .                   | 67        |

|          |  |            |
|----------|--|------------|
| 4.6      | Biased End-plate Experiments . . . . .                       | 70         |
| 4.7      | Summary . . . . .  | 70         |
| <b>5</b> | <b>Transient Study of the MSHI</b>                           | <b>73</b>  |
| 5.1      | Introduction . . . . .                                       | 73         |
| 5.2      | Experiments . . . . .  | 75         |
| 5.2.1    | Ion Diffusion Measurements . . . . .                         | 75         |
| 5.2.2    | Instability Onset Measurements . . . . .                     | 79         |
| 5.2.3    | Instability Growth Measurements . . . . .                    | 82         |
| 5.3      | Discussion . . . . .   | 85         |
| 5.3.1    | Ion Diffusion Mechanisms . . . . .                           | 85         |
| <b>6</b> | <b>Nonlinear Evolution of the MSHI</b>                       | <b>92</b>  |
| 6.1      | Introduction . . . . .                                       | 92         |
| 6.2      | Particle Trapping Instability Theory . . . . .               | 93         |
| 6.3      | Verification of Particle Trapping Instability . . . . .      | 95         |
| 6.3.1    | $n_1$ Dependence of $f_2$ . . . . .                          | 96         |
| 6.3.2    | $\phi_1$ Measurements . . . . .                              | 96         |
| 6.4      | Mode Coupling . . . . .                                      | 100        |
| 6.5      | Summary . . . . .  | 100        |
| <b>7</b> | <b>Computer Simulations</b>                                  | <b>103</b> |
| <b>8</b> | <b>Conclusions</b>   | <b>113</b> |
| <b>A</b> | <b>Observation of Other Nonlinear Evolutions of the MSHI</b> | <b>115</b> |

|     |  |     |
|-----|--|-----|
| A.1 | Period Doubling Sequence and Energy Exchange . . . . . | 115 |
| A.2 | Strong Sideband Excitations . . . . .                  | 119 |
|     | Bibliography . . . . .                                 | 122 |



# List of Tables

|     |   |     |
|-----|---|-----|
| 2.1 | Typical experimental parameters . . . . .             | 10  |
| 2.2 | Wave numbers of instabilities . . . . .               | 32  |
| 7.1 | Measured and calculated oscillation periods . . . . . | 112 |

# List of Figures

|      |  |    |
|------|--|----|
| 2.1  | The experimental setup of the beam-plasma system . . . . .   | 6  |
| 2.2  | Axial magnetic field profiles . . . . .  | 7  |
| 2.3  | Dependence of the electron current collected at the grounded end-plate $I_p$ on the filament heating power $P_f$ . . . . . | 9  |
| 2.4  | Typical probe characteristics . . . . .  | 11 |
| 2.5  | (a) $I_p$ and (b) P dependence of $n_e$ , $n_i$ and $n_b$ . . . . .  | 13 |
| 2.6  | Magnetic field dependence of the radial profiles of $n_e$ , $n_b$ and $n_i$ .  | 15 |
| 2.7  | The radial profiles of $\Phi$ and $I_p$ dependence of $E_{r0}$ . . . . .   | 17 |
| 2.8  | $T_{i\perp}$ measurement . . . . .   | 18 |
| 2.9  | $T_{i\perp}$ and $\Delta\Phi$ versus $I_p$ . . . . .   | 19 |
| 2.10 | The radial position dependence of $T_{i\perp}$ . . . . .   | 20 |
| 2.11 | Typical instability frequency spectra . . . . .  | 21 |
| 2.12 | $I_p$ dependence of (a) instability frequencies, (b) $f_1/f_2$ and (c) amplitudes . . . . .                                | 23 |
| 2.13 | $I_p$ dependence of a sequence of the frequency locking . . . . .  | 24 |
| 2.14 | Ar pressure dependence of (a) instability frequencies, (b) $f_1/f_2$ , and (c) amplitudes . . . . .                        | 25 |

|      |   |    |
|------|---|----|
| 2.15 | Ion mass dependence of instability frequencies . . . . .  | 27 |
| 2.16 | Ion mass dependence of (a) $n_1$ VS $I_p$ and (b) $f_2$ VS $n_1$ . . . . .                                | 28 |
| 2.17 | Radial profiles of (a) frequencies and (b) amplitudes . . . . .   | 29 |
| 2.18 | Radial phase shift of $n_2$ . . . . .   | 31 |
| 2.19 | Nonlinear evolution of the instabilities (1) . . . . .  | 34 |
| 2.20 | Nonlinear evolution of the instabilities (2) . . . . .  | 35 |
| 3.1  | The physical picture of the SHI . . . . .   | 41 |
| 3.2  | Dispersion relation of the MSHI . . . . .   | 51 |
| 4.1  | (a) $I_p$ , (b) P, and (c) B dependence of $f_1$ , $f_{\theta i}$ , and $f_{Ei}$ . . . . .                | 62 |
| 4.2  | (a) Ion trajectory and (b) $v_\theta$ VS $v_r$ . . . . .  | 63 |
| 4.3  | (a) Initial ion position and (b) $I_p$ dependence of $v_{\theta max}$ . . . . .                           | 65 |
| 4.4  | (a) $M/m$ and (b) B dependence of effective ion $E \times B$ drift velocity                               | 68 |
| 4.5  | End-plate bias voltage dependence of (a) plasma potential and (b)<br>$f_1$ and $f_{1calc}$ . . . . .      | 71 |
| 5.1  | (a) Time variation of the ion saturation current and (b) ion profiles                                     | 76 |
| 5.2  | Time for $I_{is}$ to reach the steady state as a function of r . . . . .                                  | 77 |
| 5.3  | (a) Atomic mass and (b) neutral pressure dependence of the diffu-<br>sion velocities . . . . .            | 78 |
| 5.4  | Ar pressure dependence of the instability onset . . . . .   | 80 |
| 5.5  | Ar pressure dependence of the instability (a) onset time, (b) fre-<br>quency, and (c) amplitude . . . . . | 81 |
| 5.6  | $I_p$ dependence of the instability onset time $\tau_{onset}$ . . . . .                                   | 82 |
| 5.7  | Radial position dependence of the electron saturation current . . .                                       | 83 |
| 5.8  | End-plate bias voltage dependence of the $I_{es}$ . . . . .   | 84 |

|      |   |     |
|------|---|-----|
| 5.9  | End-plate bias voltage dependence of the instability onset and growth   | 86  |
| 5.10 | Ion temperature and ion mass dependence of the ion perpendicular diffusion coefficient . . . . .                  | 89  |
| 6.1  | Ar pressure dependence of (a) $f_2$ VS $I_p$ and (b) $f_2$ VS $n_1$ . . . . .                                     | 97  |
| 6.2  | $I_p$ dependence of (a) $\Delta\Phi$ and $\phi_1$ and (b) the calculated $f_{bounce}$ . .                         | 98  |
| 6.3  | Ion mass dependence of $\Delta\Phi$ and $\phi_1$ . . . . .  | 99  |
| 7.1  | Electron and ion density plots (1) . . . . .  | 106 |
| 7.2  | Electron and ion density plots (2) . . . . .  | 107 |
| 7.3  | Time history of the potential fluctuation . . . . .   | 108 |
| 7.4  | Time histories of (a) electron and (b) ion density fluctuations together with the potential fluctuation . . . . . | 109 |
| 7.5  | Potential fluctuations measured by three probes separated 90 degrees each other . . . . .                         | 110 |
| 7.6  | Ion trajectories . . . . .  | 111 |
| A.1  | $I_p$ dependence of (a) instability frequencies, (b) $f_1/f_2$ and (c) amplitudes . . . . .                       | 116 |
| A.2  | A sequence of an energy exchange between $M_{1/2n}$ mode and $M_{n+2}$ , $M_{s_{n+1}}$ modes . . . . .            | 118 |
| A.3  | Ar pressure dependence of a sequence of an excitation of the side-band modes . . . . .                            | 121 |

## Acknowledgements

The author is deeply indebted to many people for their valuable contributions to this work.

First of all, I would like to thank my advisor Professor Chan Joshi. His continued support and guidance have made this work possible.

I also would like to thank my co-advisor Professor Francis Chen for innumerable advice and suggestions.

I would thank Professors John Dawson, Reiner Stenzel and Neville Luhmann for agreeing to be on my committee and for their helpful suggestions.

On the experimental side, I wish to thank Dr. Garnick Hairapetian for his many good discussions. Special thanks also to Mr. Rick Savage who gave me a lot of useful suggestions for designing the experimental apparatus, to Dr. V. K. Jain and Dr. Yoneyoshi Kitagawa for their many good discussions.

On the theory and computer simulation side, I am very grateful to Dr. J. J. Su. Without him, I could not have started the computer simulation work. I would like to thank Dr. Predhiman Kaw for useful discussions and suggestions on kinetic theory and the mode-coupling theory. I would also thank Professor John Dawson and Dr. Tudor Johnston for many useful suggestions.

I am very thankful to Mr. Amit Lal, Dr. Chris Clayton, Mr. Ken Marsh, Dr. Warren Mori and Dr. Tom Katsouleas for their assistance and many useful suggestions. I also thank Mrs. Maria Guerrero and Miss Maria Serafica for their administrative support.

Finally, I offer my deepest gratitude to my wife Sayuri for her support.

## VITA

Youichi Sakawa

|               |  |
|---------------|--|
| July 28, 1961 | Born, Kyoto, Japan   |
| 1980 – 1984   | B.S., Electrical Engineering, Osaka University, Osaka, Japan.  |
| 1984 – 1986   | M.S., Electrical Engineering, Osaka University, Osaka, Japan.  |
| 1986 – 1987   | Rotary Foundation Scholarship  |
| 1987 – 1992   | Graduate Reseach Engineer, Department of Electrical Engineering , University of California, Los Angeles. |

## PUBLICATIONS

- V. K. Jain, Y. Sakawa, and C. Joshi  
Period Doubling and Eventual Chaos in an Electron Beam-Plasma System  
Bulletin of the American Physical Society, **33**, No. 9 (1988), 1877.
- C. Joshi. C. Clayton, K. Marsh, Y. Sakawa, R. L. Savage, Jr.  
Evidence for Periodic Breakup of a Radially Modulated 0.35  $\mu\text{m}$  Laser Beam due to Thermal Self-Focusing in a Plasma  
Bulletin of the American Physical Society, **33**, No. 9 (1988), 1994.
- C. Joshi. C. E. Clayton, K. Marsh, Y. Sakawa and R. L. Savage Jr.  
Evidence for Periodic Breakup of a Radially Modulated 0.35  $\mu\text{m}$  Laser Beam due to Thermal Self-Focusing in a Plasma  
Optics Communications **70**, 44 (1989).
- Y. Sakawa, C. Joshi, and V. K. Jain  
Observation of Chaos in a Strongly Magnetized Electron Beam  
Bulletin of the American Physical Society, **34**, No. 9 (1989), 1927.
- Y. Sakawa and C. Joshi  
Observation of Quasi-periodic Route to Chaos in an Electron Beam Driven Plasma  
Bulletin of the American Physical Society, **35**, No. 9 (1990), 2007.

- Y. Sakawa, J. J. Su, C. Joshi and P. K. Kaw  
Excitation and Nonlinear Evolution of the Modified Simon-Hoh Instability in an Electron Beam Produced Plasma Column  
Bulletin of the American Physical Society, **36**, No. 9 (1991), 2328.
- Y. Sakawa, C. Joshi, J. J. Su, P. K. Kaw, F. F. Chen and V. K. Jain  
Excitation of the Modified Simon-Hoh Instability in an Electron Beam Produced Plasma  
Phys. Fluids, in preparation.

## ABSTRACT OF THE DISSERTATION

# Excitation and Nonlinear Evolution of the Modified Simon-Hoh Instability in an Electron Beam Produced Plasma Column

by

Youichi Sakawa

Doctor of Philosophy in Electrical Engineering

University of California, Los Angeles, 1992

Professor Chan Joshi, Co-Chair

Professor Francis F. Chen, Co-Chair

An intermediate frequency ( $f_{ci} < f < f_{ce}$ ) electrostatic instability has been observed in an electron beam produced, cylindrical plasma column. We have identified this instability as a new instability, the Modified Simon-Hoh instability (MSHI), which has an instability mechanism similar to the Simon-Hoh instability (SHI). This instability can occur in a cylindrical collisionless plasma if a radial DC electric field exists and if this radial DC electric field and the radial density gradient are in the same direction. The origin of the DC electric field is found to be the difference between the ion and the electron radial density profiles. In such a plasma if the ions are essentially unmagnetized but if the electrons are magnetized, a velocity difference in the  $\theta$  direction can arise because of the finite ion Larmor radius effect. This leads to a space charge separation in the  $\theta$  direction. The consequent azimuthal electric field  $E_{\theta 1}$  and the enhancement of the density perturbation by the  $E_{\theta 1} \times B_0$  velocity occur in the same manner as in the SHI.



The instability frequency is decided by the ion azimuthal drift velocity. We have investigated this new instability through experiments, theory and 2D computer simulations.

We believe that a finite amplitude modified Simon-Hoh instability is driven modulationally unstable by ion trapping effects leading to the excitation of  $M_2$  mode and the sideband modes  $M_s$ . The final state can be a new periodic oscillation, the mode-locked state with  $f_2 = f_s = f_1/2$ . Such a periodic state is likely to be further modulationally unstable to a low-frequency  $M_3$  mode which will then migrate and perhaps mode-lock at  $f_2/2$  and so on. Thus, what at first sight appears to be a simple period doubling route of chaos follows a rather complex path starting at the low-frequency modulational end and finally mode-locking at the sub-harmonic.

# Chapter 1

## Introduction

Plasmas abound in turbulence as is evident from measurements on laboratory, fusion, space and astrophysical plasmas. However, the transition from a simple unstable equilibrium dominated by linearized instabilities with predictable thresholds,  $k$ -value, frequencies, growth rates, etc. to a turbulent state in the plasma is generally very complex. This is undoubtedly because compared to other systems with infinite degrees of freedom (such as a hydrodynamic fluid, for example) a plasma has a richer variety of collective modes of oscillation and a greater number of nonlinear coupling mechanisms (some examples of the latter are particle trapping, hydrodynamic nonlinearities, nonlinear resonant wave-particle interactions, harmonic generation, wave breaking, etc.). Furthermore, in plasma experiments one is typically unable to control the plasma parameters with enough precision so that the subtle phenomena near the transition to turbulence may be studied. The result has been that whereas the recent developments in nonlinear dynamics

and transition from order to chaos via the various well-known routes such as successive period doubling, intermittency, two-frequency mechanisms, etc., has led to a variety of experiments in fluids dynamics, chemical reactions, nonlinear optics, laser physics, electronics, etc. there has been no study of comparable detail in the case of waves in plasmas.

The work discussed in this thesis arose from an experimental program at UCLA designed to understand the evolution of a plasma from one coherent state into turbulence. The plasma system chosen for this study is an electron beam produced, and magnetically confined plasma column. In the regime where the neutral gas pressure is low and the exciting electron beam current is small, such a plasma column is seen to be unstable to one mode. This new unstable mode is called the “modified Simon-Hoh instability” (MSHI), which has an instability mechanism similar to the Simon-Hoh instability (SHI). This instability can occur in a cylindrical collisionless plasma if a radial DC electric field exists and if this radial DC electric field and the radial density gradient are in the same direction. The origin of the DC electric field is found to be the difference between the ion and the electron radial density profiles. In such a plasma if the ions are essentially unmagnetized but the electrons are magnetized, a velocity difference in the  $\theta$  direction can arise because of the finite ion Larmor radius effect. This leads to a space charge separation in the  $\theta$  direction. The consequent azimuthal electric field  $E_{\theta 1}$  and the enhancement of the density perturbation by the  $E_{\theta 1} \times B_0$  velocity occur in the same manner as in the SHI. The instability frequency is decided by the ion azimuthal drift velocity.

The specific process which leads to an eventual turbulent spectrum in the

plasma is the evolution of the MSHI through a series of modulational instabilities involving ion trapping effects.

An interesting aspect of the present system is that the evolution of the frequency spectrum of the unstable modes has many similarities to the usual frequency doubling and the two-frequency routes to chaos in simple nonlinear oscillators. The detailed behavior is, however, much more complicated, involving interaction between many modes whose “physics” is at present only qualitatively understood.

We believe that such a scenario leading to a turbulent state in a plasma may be generic to plasmas and applicable to many systems involving excitation of coherent modes.

At the outset it must be stated that the work described in this thesis is still very open-ended. The main contribution of our work is to document in detail a plasma instability through experiments and explain it through theory and computer simulations. The nonlinear behavior of this instability is experimentally documented but as yet not fully understood. It presents a ripe topic for future work.

# Chapter 2

## Experiments

### 2.1 Introduction

As stated earlier the ultimate goal of this project is to understand the evolution of turbulence in one particular plasma system. In our case the plasma system is an electron beam ionized plasma column confined by an axial magnetic field. Such a plasma is found to be extremely quiescent with thermally induced density fluctuations, which are nearly 70 dB lower in amplitude than the peak instability amplitude and close to the intrinsic noise level of the signal analyzer. The idea is to excite a single coherent unstable mode in such a plasma and then to follow its subsequent nonlinear evolution through wave particle and wave-wave interactions into a turbulent state. In order to follow this nonlinear evolution the plasma parameters have to be controlled with extreme precision. As will be seen later in our beam-plasma system, at low neutral gas pressures and a low beam density, we were able to excite a single low frequency unstable plasma mode. This

mode has been named the modified Simon-Hoh instability. There are no other usual collective oscillations in our plasma such as the electron plasma and electron cyclotron oscillations in the experimental parameter range. In fact, most of this thesis is about the detailed experimental observation and documentation of this new, rather remarkable, unstable mode and its theoretical interpretation. This mode is robust in the sense that it is seen to persist over a very broad parameter range without any interference from other fluid-like modes. Its nonlinear interaction is mainly with plasma particles through trapping and other kinetic modes of the plasma.

We now discuss the experimental apparatus and the experimental results of excitation and nonlinear evolution of electrostatic instabilities.

## 2.2 Experimental Apparatus

Figure 2.1 shows the experimental setup of our beam-plasma system. A 1 cm full-width half-maximum (FWHM) diameter Gaussian electron beam is injected axially into one end of a 10 cm diameter, 180 cm long stainless steel vacuum vessel, immersed in a DC magnetic field of up to 320 G. The distance between the electron gun and a grounded endplate target (1.2 cm diameter) defines the interaction region to be 80 cm. Figure 2.2 shows axial profiles of the magnetic fields. In the interaction region  $\Delta B/B$  is less than 3 %. Most of our measurements are conducted at  $B = 160$  G ( $I_m = 13$  A). Argon gas is used for most of our measurements, at a pressure range of  $5 \times 10^{-6}$  torr to  $5 \times 10^{-5}$  torr, with a vacuum base pressure of  $4 \times 10^{-7}$  torr. We also tried Xe, Kr,  $N_2$  and He to determine the

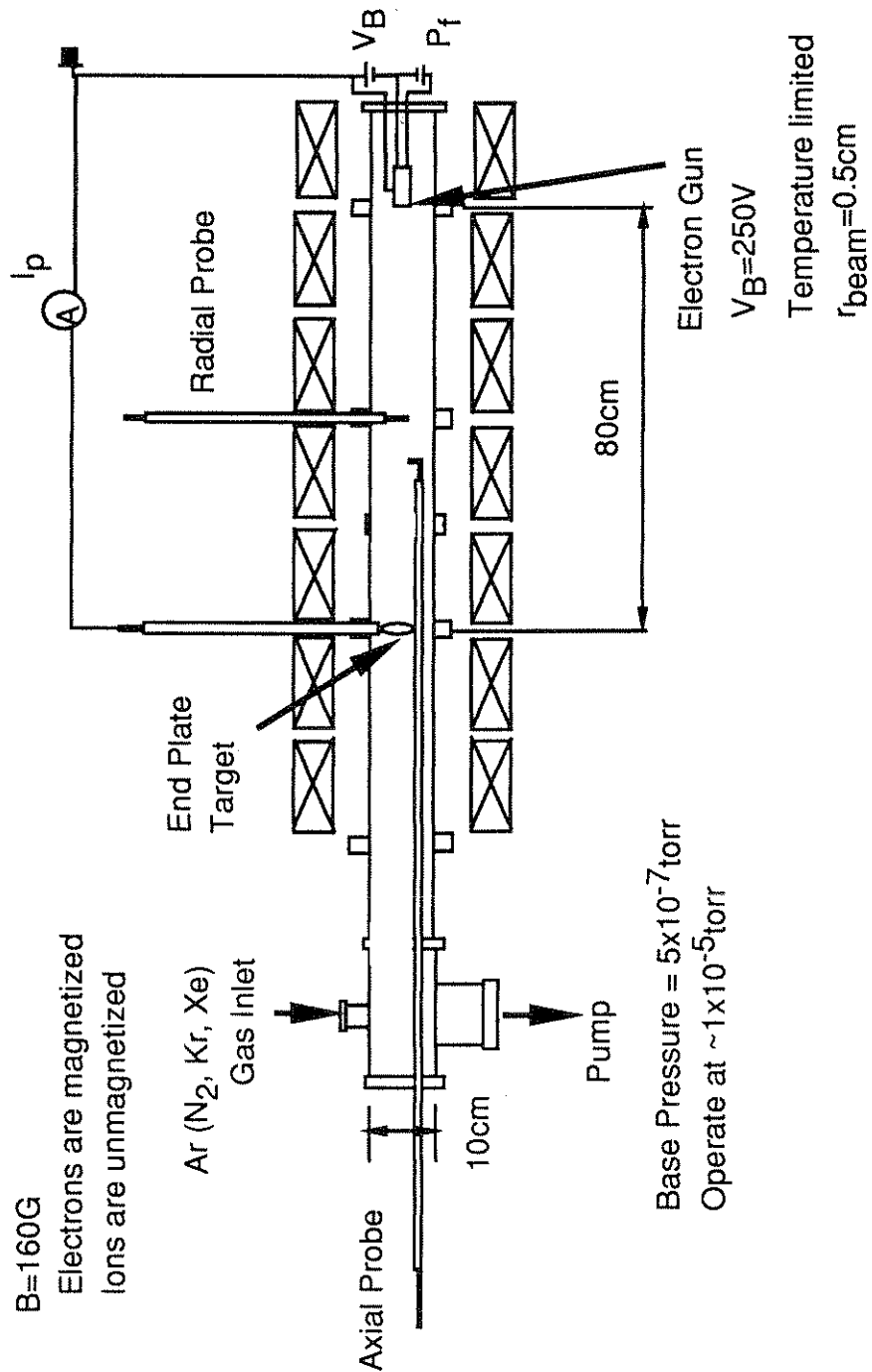


Figure 2.1: The experimental setup of the beam-plasma system. The plasma is produced by collisional ionization of the neutral gas by the electron beam. The emissive probe, the one-sided probe and the energy analyzer are not shown.

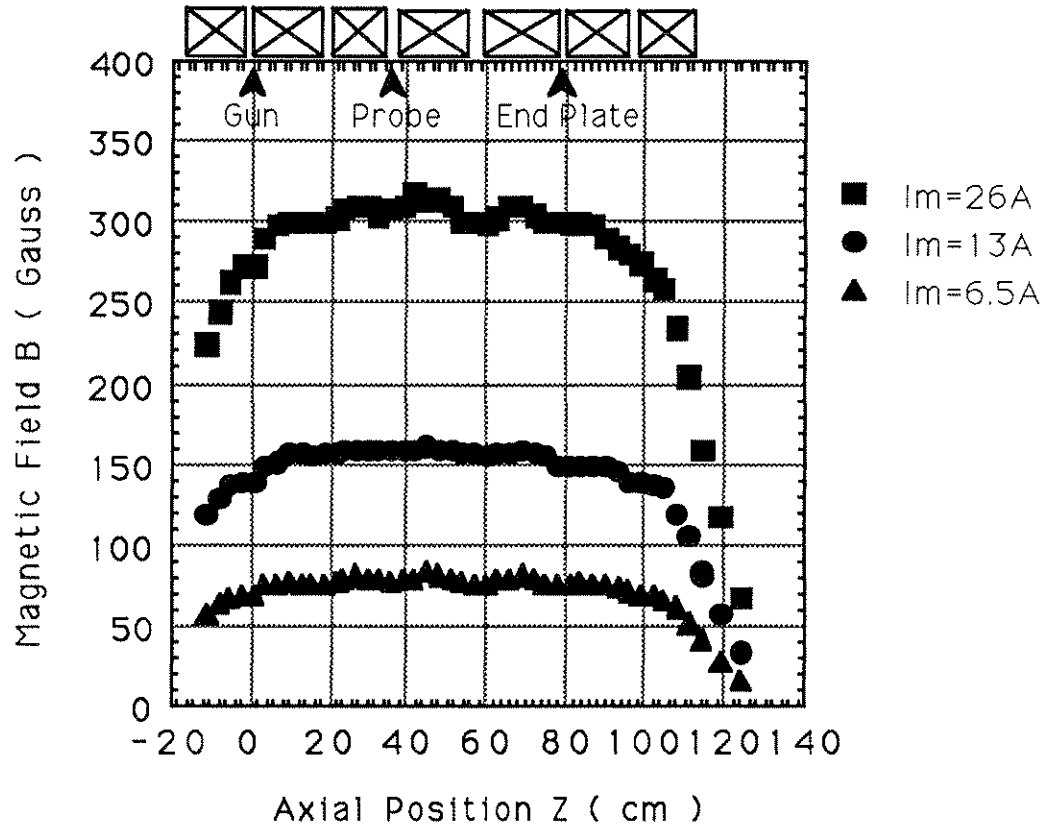


Figure 2.2: Axial magnetic field profiles. In the interaction region  $\Delta B/B$  is less than 3 %. Most of our measurements are conducted at  $B = 160\text{ G}$  ( $I_m = 13\text{ A}$ ).



ion mass dependence of the instabilities.

Electrons are emitted from a directly heated spiral tungsten filament cathode which is biased negative to a grounded anode. Electrons are accelerated through a 1 cm diameter hole of the anode and collected by a grounded endplate target. Figure 2.3 shows the electron beam current at the endplate target ( $I_p$ ) as a function of the filament heating power ( $P_f$ ) for three beam acceleration voltages ( $V_B$ ).  $V_B$  is variable up to 500 V.  $I_p$  is governed by temperature limited emission at lower  $P_f$ , and governed by space-charge limited emission at higher  $P_f$ . Experiments were performed at  $V_B = 250$  V,  $I_p = 10 \sim 1000$   $\mu$ A, which is in the temperature limited emission region.

## 2.3 DC Parameter Measurements

Table 2.1 summarizes typical experimental parameters. The measurements of several of these will be discussed in detail later in this thesis.

### 2.3.1 Density Measurements

Beam and plasma densities are measured by the Langmuir probes. Most of our density measurements were conducted with a cylindrical probe (0.5 mm in diameter and 2 mm in length). Since the typical gas pressures are low, probe characteristics show a clear distinction (a pronounced knee) between the ion saturation current ( $I_{is}$ ), the beam electron current ( $I_{beam}$ ) and the electron saturation current ( $I_{es}$ ). Figure 2.4 shows probe characteristics measured by a 2 mm x 2 mm disk probe (0.05 mm in thickness). When the probe is normal to the gun, we

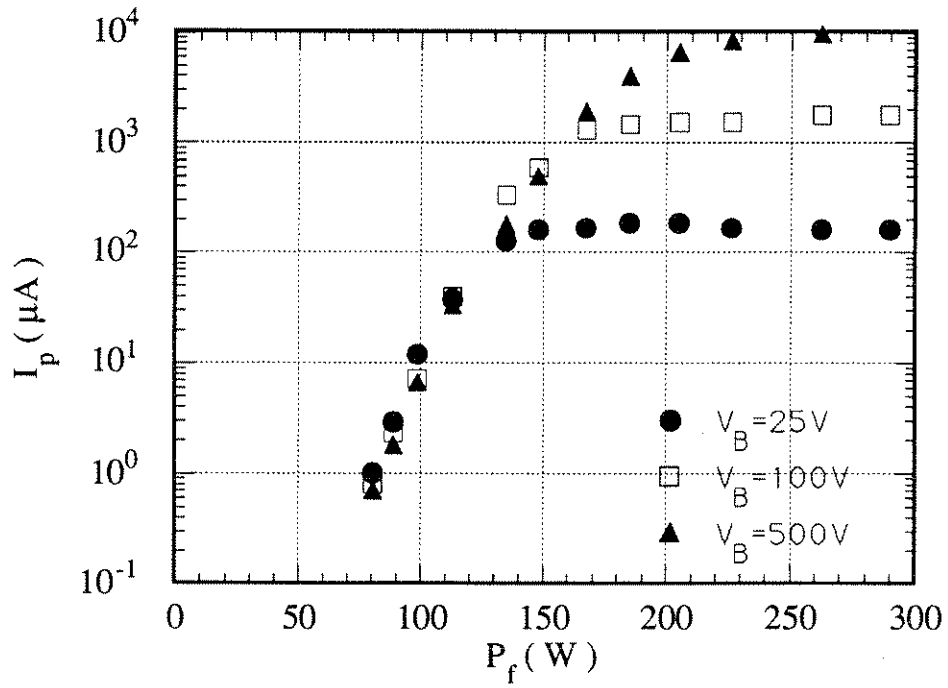


Figure 2.3: Dependence of the electron current collected at the grounded end-plate  $I_p$  on the filament heating power  $P_f$ .  $I_p$  is governed by temperature limited emission at lower  $P_f$ , and governed by space-charge limited emission at higher  $P_f$ . Experiments were performed at  $V_B = 250\text{ V}$ ,  $I_p = 10 \sim 1000\ \mu\text{A}$ , which is in the temperature limited emission region.

---

|                  |   |
|------------------|---|
| Gas used         | Ar (He, N <sub>2</sub> , Kr, Xe)                  |
| Pressure         | $P = 5 \times 10^{-6} \sim 5 \times 10^{-5}$ torr |
| Magnetic field   | $B = 40 \sim 280$ G                               |
| Endplate current | $I_p = 10 \sim 1000$ $\mu$ A                      |
| Beam voltage     | $V_B < 500$ V                                     |

for Ar  $2 \times 10^{-5}$  torr,  $I_p = 100$   $\mu$ A,  $V_B = 250$  V,  $B = 160$  G

|                                   |   |
|-----------------------------------|---|
| Beam density                      | $n_b \approx 10^6$ cm <sup>-3</sup>   |
| Plasma density                    | $n_p \approx 10^8$ cm <sup>-3</sup>   |
| Electron temperature              | $T_e \approx 4$ eV  |
| Ion parallel temperature          | $T_{i\parallel} > 0.03$ eV  |
| Ion perpendicular temperature     | $T_{i\perp} \approx 5$ eV   |
| DC radial electric field          | $E_{r0} \approx 4.7$ V/cm   |
| Plasma potential difference       | $\Delta\Phi \approx 5.0$ V  |
| Measured instability frequency    | $f_1 = 48.25$ kHz (m = 1: measured)   |
| Ion cyclotron frequency           | $f_{ci} = 6.1$ kHz  |
| Ion plasma frequency              | $f_{pi} = 330$ kHz  |
| Electron ExB frequency            | $f_{E \times B} = 940$ kHz (m = 1)  |
| Electron diamagnetic frequency    | $f^* = 3.0$ MHz (m = 1)   |
| Azimuthal phase velocity          | $\omega_1/k_{\theta 1} = 1.3 \times 10^5$ cm/s ( $k_{\theta 1} = 2$ cm <sup>-1</sup> )      |
| Axial phase velocity              | $\omega_1/k_{z1} = 8.3 \times 10^6$ cm/s ( $k_{z1} \approx 0.03$ cm <sup>-1</sup> )         |
| Ion acoustic velocity             | $c_s = 3.1 \times 10^5$ cm/s  |
| Electron thermal velocity         | $v_{the} = 1.2 \times 10^8$ cm/s  |
| Collision frequency               |   |
| Electron-neutral elastic[2]       | $\nu_{en} = 6.6 \times 10^4$ Hz   |
| Ion-neutral charge exchange[2, 3] | $\nu_{in} = 2.2 \times 10^2 \sim 2.9 \times 10^3$ Hz  |
| Electron-ion[4]                   | $\nu_{ei} = 2.5 \times 10^2$ Hz   |
| Collision mean-free-path          |   |
| Electron-neutral elastic[2]       | $\lambda_{en} = 1.8 \times 10^3$ cm ( $\sigma_{en} = 8.4 \times 10^{-16}$ cm <sup>2</sup> ) |
| Ion-neutral charge exchange[2, 3] | $\lambda_{in} = 1.7 \times 10^2$ cm ( $\sigma_{in} = 9.0 \times 10^{-15}$ cm <sup>2</sup> ) |
| Electron-ion[4]                   | $\lambda_{ei} = 5.4 \times 10^5$ cm   |
| Electron Debye length             | $\lambda_D = 0.15$ cm at center<br>1.5 cm at r = 2 cm                                       |
| Larmor radius                     |   |
| Electron                          | $\lambda_{Le} = 0.04$ cm  |
| Ion                               | $\lambda_{Li} = 12.5$ cm ( $T_{i\perp} = 5$ eV)   |

---

Table 2.1: Typical experimental parameters

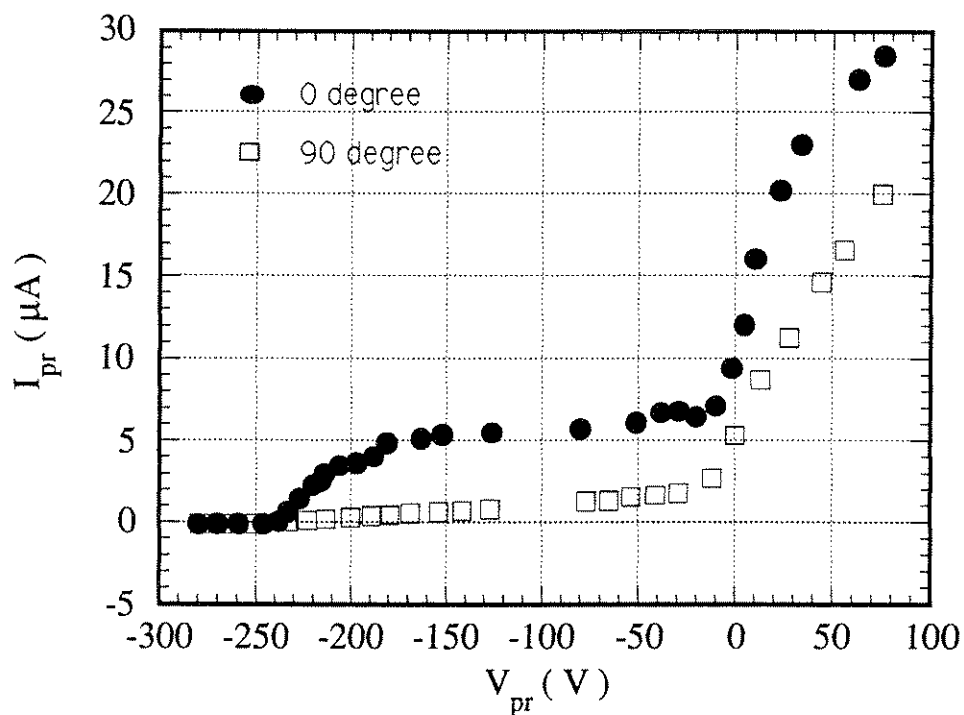


Figure 2.4: Probe characteristics measured by a 2 mm x 2 mm disk probe (0.05 mm in thickness). The beam acceleration voltage  $V_B$  is 250 V in this measurement. For  $V_{pr} < -250$  V, only the ion saturation current is collected; for  $V_{pr} > 0$  V, the contribution is mainly from the plasma electrons; a clear beam electron component is observed for  $-250$  V  $< V_{pr} < 0$  V when the probe is normal to the gun (closed circle); when the probe is 90 degrees to the gun (open square), a very small beam component collected by the probe area of 0.05 mm thickness x 2 mm length is observed.

observe a clear beam component with the probe biased more negative with respect to the beam acceleration voltage,  $V_B$ , which is 250 V in this measurement. The beam density is measured by this beam current. When the probe is 90 degrees to the gun, a very small beam component collected by the probe area of 0.05 mm thickness x 2 mm length is observed.

In a magnetic field, the electron saturation current is reduced due to the reduced diffusion coefficient across the field[1]. Therefore, the absolute magnitude of  $n_e$  is not reliable. However, as long as B is constant, the relative magnitudes of  $n_e$  (as a function of radius r or beam current  $I_p$ , etc.) are thought to be correct. On the other hand,  $n_i$  is overestimated in our measurement due to the thick sheath effect[1]. Since we have to bias the probe more negative with respect to  $V_B = 250$  V to collect ions, we have applied the probe voltage  $V_{pr} = -280$  V. With such a large bias voltage, we expect to have an effective probe surface area larger than the actual probe size because of the thick sheath. If we extrapolate the ion current at the plasma potential, we find nearly an order of magnitude lower current compared with the current at  $V_{pr} = -280$  V. Because of these uncertainties in both the electron and ion density measurements by probe, we cannot determine the plasma densities from probe measurements alone. On the other hand the absolute value of the difference between the electron and ion densities ( $n_e - n_i$ ) can be obtained from the measurement of the plasma potential  $\Phi$ . Since the relative radial profiles of the densities are thought to be correct, we adjust the peak density of the electrons and ions to fit the measured potential profiles.

Figure 2.5(a) shows the dependencies of  $n_e$ ,  $n_i$  and  $n_b$  on  $I_p$  taken at a radius of 0.2 cm. The Ar pressure (P) dependences of  $n_i$ ,  $n_e$  and  $n_b$  with a constant  $I_p$

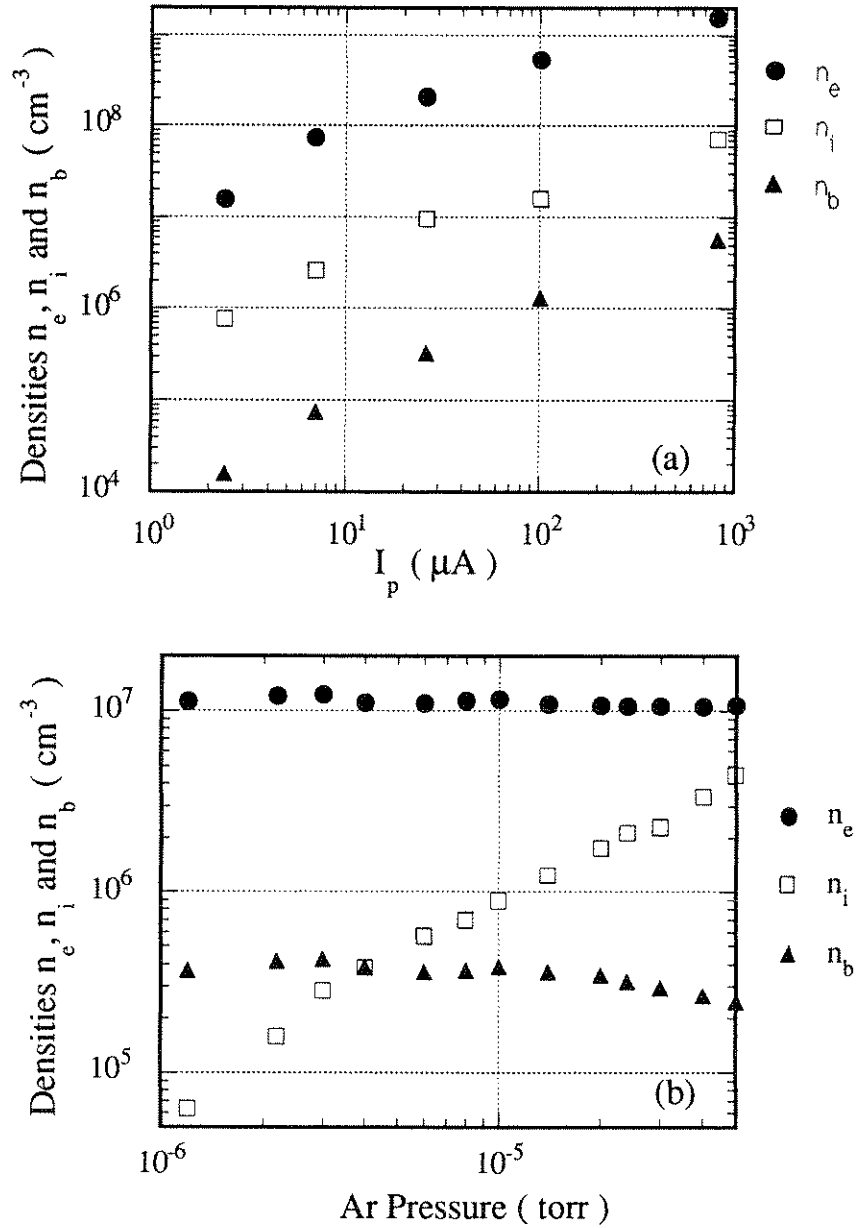


Figure 2.5: (a) The dependencies of  $n_e$  (closed circle),  $n_i$  (open square) and  $n_b$  (closed triangle) on  $I_p$ . Ar  $1 \times 10^{-5}$  torr,  $B = 160$  G,  $r = 0.2$  cm. (b) The pressure (P) dependence of  $n_e$ ,  $n_i$  and  $n_b$  with a constant  $I_p$  taken at the center of the beam.  $n_i$  is proportional to P, while  $n_e$  and  $n_b$  are nearly constant with P.  $I_p = 50 \mu\text{A}$ ,  $B = 160$  G.

are shown in fig. 2.5(b). This measurement is taken at the center of the beam.  $n_i$  is proportional to P, while  $n_e$  and  $n_b$  are nearly constant with P. Obviously,  $n_i$  is not equal to  $n_e$ . As will be seen shortly this is thought to be due to the difference in the radial profiles of the electron and the ions.

The measured magnetic field (B) dependence of the radial profiles of  $n_i$ ,  $n_e$  and  $n_b$  are shown in fig. 2.6. At B = 160 G,  $n_e$  and  $n_b$  have 1.0 cm (FWHM) Gaussian profiles, while  $n_i$  shows a broad profile from the beam center to the chamber wall ( $r = 5$  cm). The  $n_e$  profile becomes broader at the lower B, while that of  $n_i$  is nearly unchanged with B. This is because ions are unmagnetized ( $r_{Li} \gg r_p$ , where  $r_{Li}$  is the ion Larmor radius and  $r_p = 0.5$  cm is the plasma size) even at B = 280 G, while electrons are weakly magnetized ( $r_{Le} \leq r_p$ , where  $r_{Le}$  is the electron Larmor radius) at the lower values of B but are strongly magnetized ( $r_{Le} \ll r_p$ ) for high values of B.

### 2.3.2 Plasma Potential Measurements

The difference between the  $n_e$  and  $n_i$  profiles implies the existence of a radial DC electric field,  $E_{r0}$ , which we deduced by measuring the radial profiles of the plasma potential,  $\Phi$ , with an emissive probe [1].  $\Phi$  is obtained from a measurement of the floating potential of an emissive probe (0.05 mm diameter tungsten wire) heated by a DC power supply. The I-V trace of the probe is taken to confirm that the emission current is much larger than the collection current, and the floating potential of the probe matches well with the plasma potential. The radial profiles of  $\Phi$  as a function of  $I_p$  are shown in fig. 2.7(a), and the calculated maximum

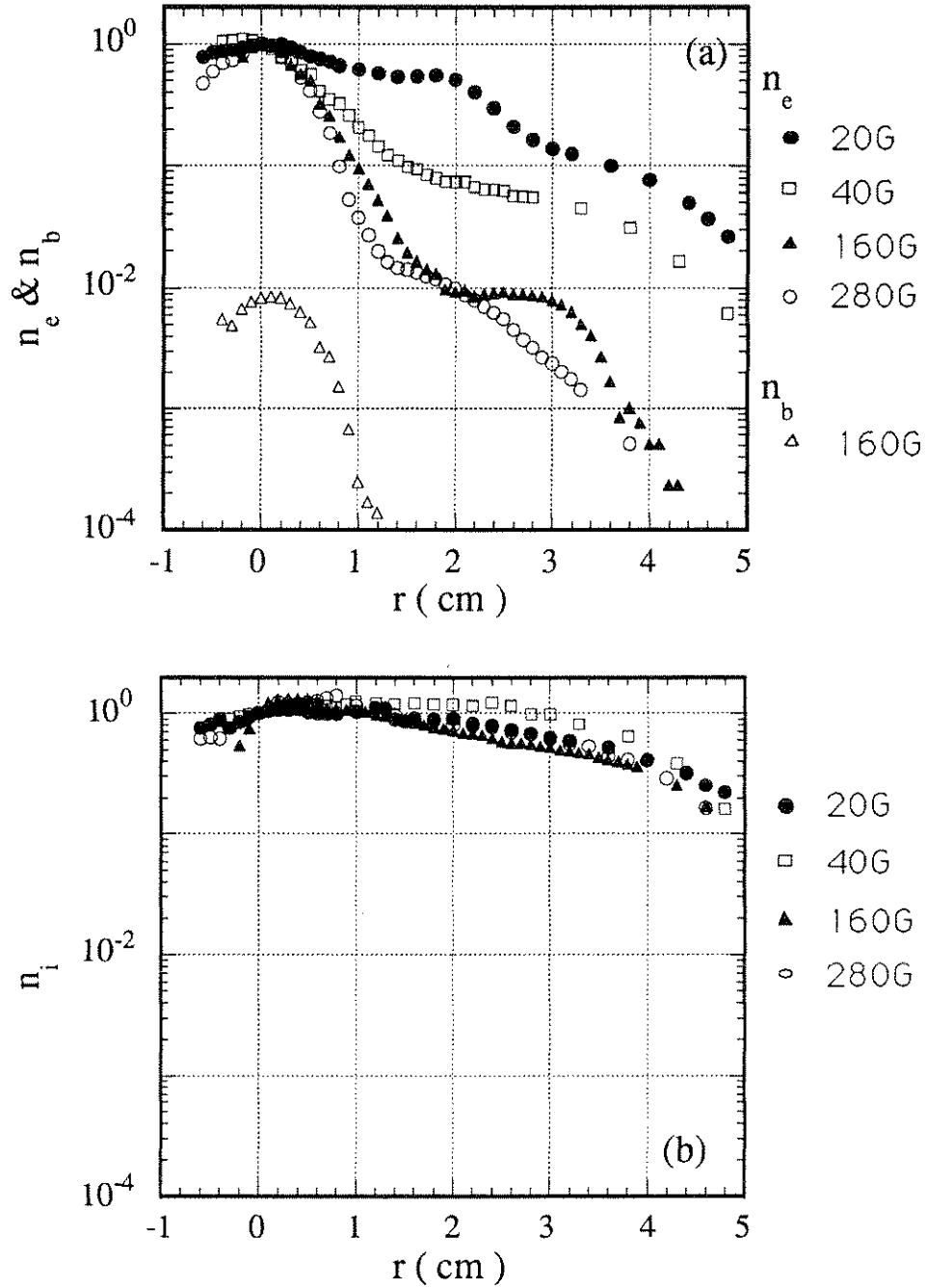


Figure 2.6: The measured magnetic field dependence of the radial profiles of (a)  $n_e$ ,  $n_b$  and (b)  $n_i$ . At  $B = 160$  G,  $n_e$  and  $n_b$  have 1.0 cm (FWHM) Gaussian profiles, while  $n_i$  shows a broad profile from the beam center to the chamber wall ( $r = 5$  cm). The  $n_e$  profile becomes broader at lower  $B$ , while that of  $n_i$  is nearly unchanged with  $B$ . Ar  $2 \times 10^{-5}$  torr,  $I_p = 500 \mu\text{A}$ .



$E_{r0}$  is shown in fig. 2.7(b). We find that  $E_{r0}$  increases monotonically with  $I_p$  and decreases with pressure  $P$ . The density difference  $n_e - n_i$ , calculated using Poisson's equation, is positive in the beam region and negative outside the beam. This is qualitatively consistent with the radial profiles of  $n_e$  and  $n_i$  measured using the Langmuir probes.

### 2.3.3 Temperature Measurements

The ion perpendicular temperature,  $T_{i\perp}$ , is measured by an energy analyzer which consists of two mesh grids and a collector plate. It is 1.5 cm in diameter and 1.25 cm long and faces radially inward on a radially movable shaft. The first grid is left to float to repel most electrons and pass ions. The collector plate is biased to  $V_c = -67.5$  V to collect ions and repel electrons. Figure 2.8 shows the measured collector current ( $I_c$ ) versus discriminator voltage ( $V_d$ ) and its derivative  $dI_c/dV_d$  for  $I_p = 1 \mu\text{A}$  (fig. 2.8(a)) and  $I_p = 7000 \mu\text{A}$  (fig. 2.8(b)).  $T_{i\perp}$  calculated from the e-folding bias voltage in the  $dI_c/dV_d$  curve is shown in fig. 2.9 as a function of  $I_p$ .<sup>1</sup> The DC plasma potential difference,  $\Delta\Phi$ , between  $r = 2.0$  cm and  $r = 0$  cm measured by the emissive probe is also shown in fig. 2.9. A good agreement between  $T_{i\perp}$  and  $\Delta\Phi$  is obtained.

The radial position dependence of  $T_{i\perp}$  is shown in fig. 2.10.  $T_{i\perp}$  is larger at the central region. Although the parallel component of the ion temperature was not measured, we expect  $T_{i\parallel}$  to be on the order of 0.03 eV (room temperature),

---

<sup>1</sup>Since the energy analyzer is not a directional energy analyzer, the measured  $T_{i\perp}$  might be overestimated due to an angular divergence of ions[5].

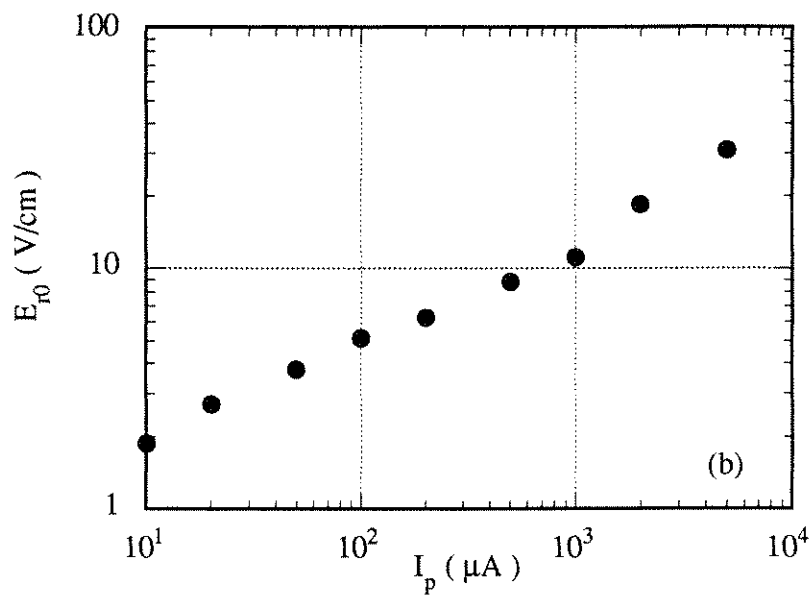
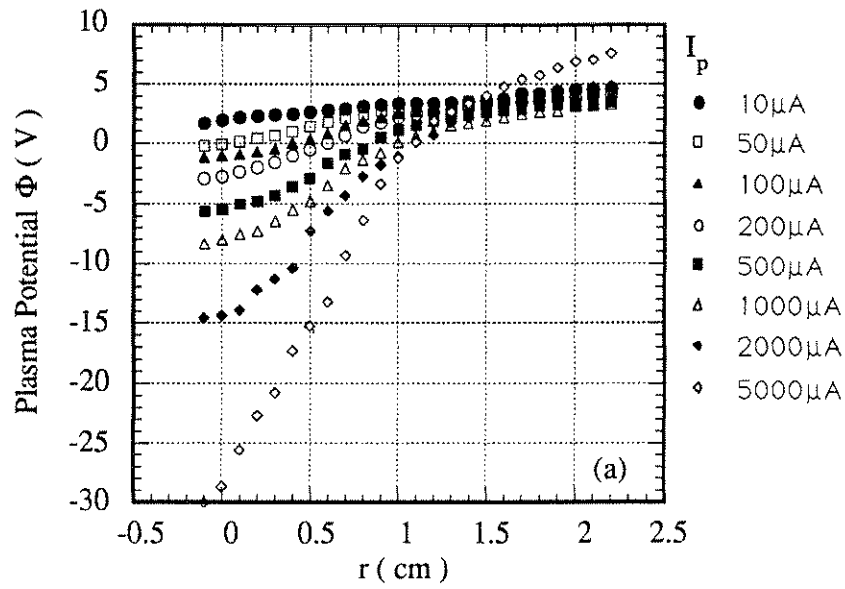


Figure 2.7: (a) The radial profiles of  $\Phi$  as a function of  $I_p$  measured by the emissive probe. Ar  $2 \times 10^{-5}$  torr,  $B=160$  G. (b)  $I_p$  dependence of the calculated maximum  $E_{r0}$  ( $r \approx 0.5$  cm).  $E_{r0}$  increases with  $I_p$ .

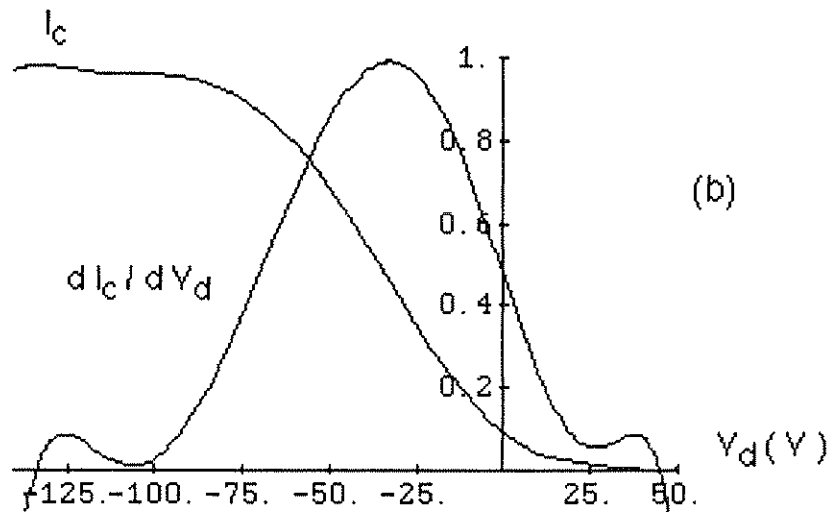
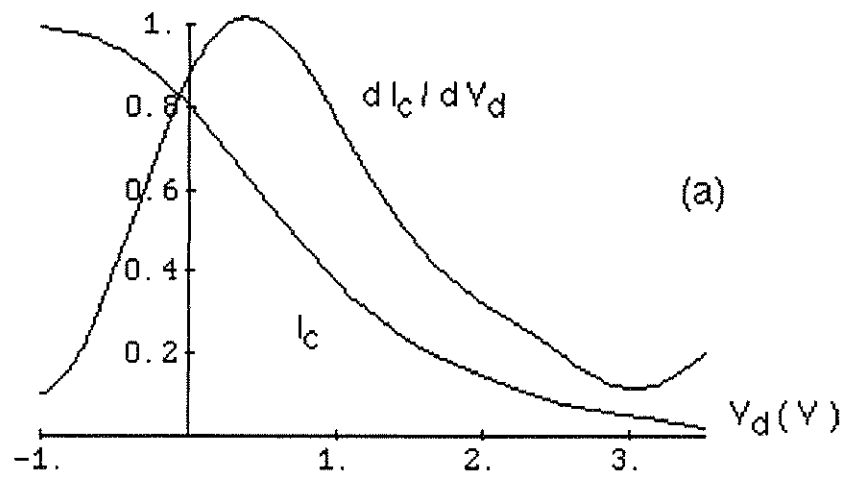


Figure 2.8: The measured energy analyzer collector current ( $I_c$ ) versus discriminator voltage ( $V_d$ ) and its derivative  $dI_c/dV_d$  for (a)  $I_p = 1 \mu\text{A}$  and (b)  $I_p = 7000 \mu\text{A}$ .

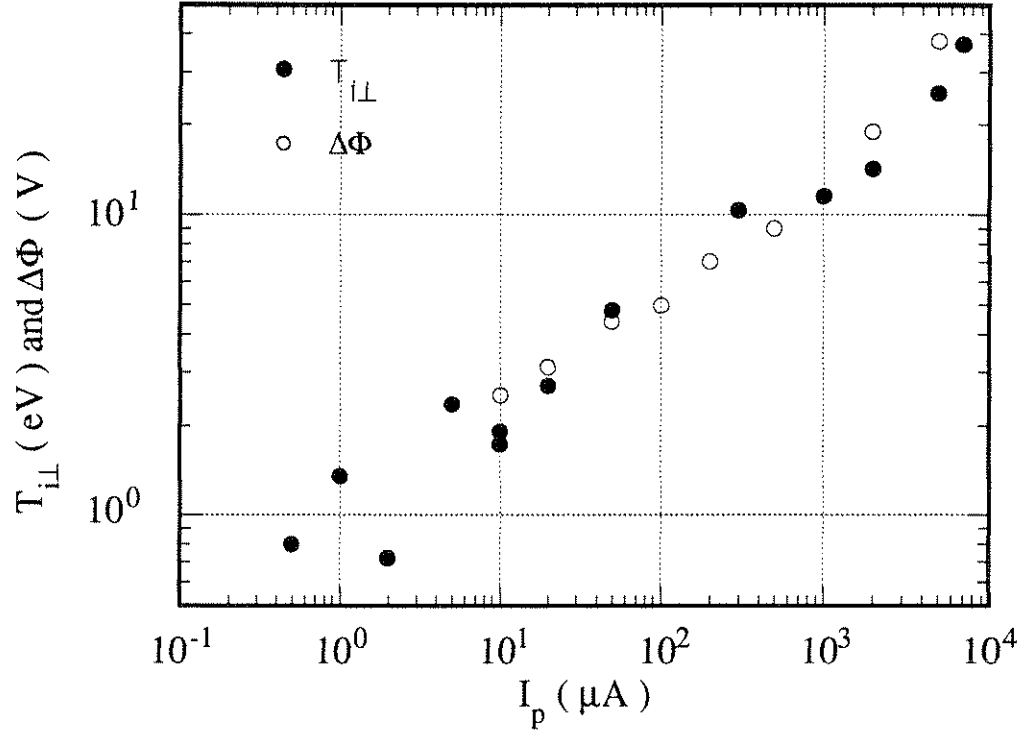


Figure 2.9: Dependence of  $T_{i\perp}$  on  $I_p$  (closed circle).  $T_{i\perp}$  is calculated from the e-folding bias voltage in the  $dI_c/dV_d$  curve shown in fig. 2.9. The DC plasma potential difference,  $\Delta\Phi$ , between  $r = 2.0$  cm and  $r = 0$  cm measured by emissive probe is also shown (open circle). A good agreement between  $T_{i\perp}$  and  $\Delta\Phi$  is obtained.

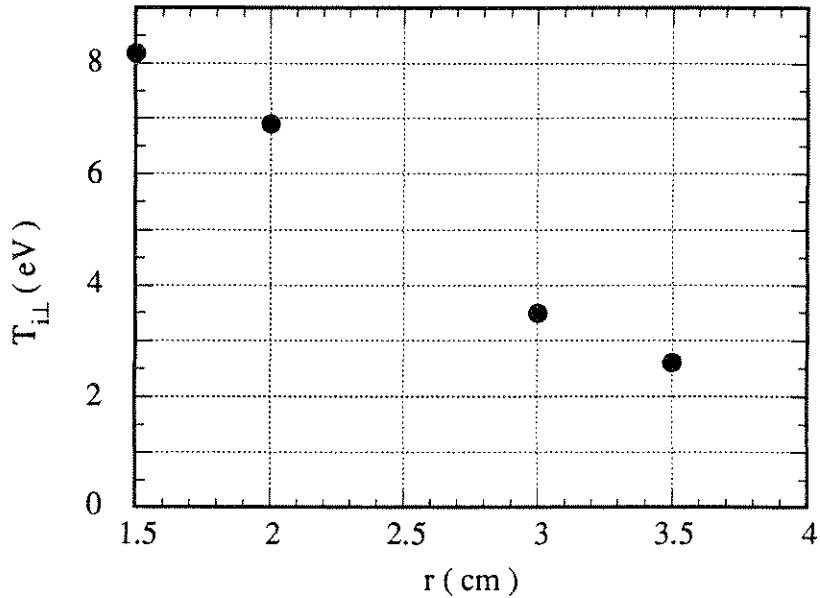


Figure 2.10: The radial position dependence of  $T_{i\perp}$ .  $T_{i\perp}$  is larger at the central region.

because of the very large electron-ion equilibrium time<sup>2</sup>. Therefore,  $T_{i\perp} \neq T_{i\parallel}$ .

The plasma electron temperature measured by the Langmuir probe is  $\sim 4$  eV.

## 2.4 Instability Measurements

By varying the experimental parameters, the gas pressure ( $P$ ) and the beam current ( $I_p$ ) being the most sensitive, a low frequency mode  $M_1$  with a frequency  $f_1$  between the ion cyclotron ( $f_{ci}$ ) and the ion plasma ( $f_{pi}$ ) frequencies ( $f_{ci} \ll f_{pi}$ ), is excited. Our mode measurements were made with unbiased, grounded cylindrical probes (0.5 mm in diameter and  $\sim 2$  mm in length). However, the same results, with much reduced amplitudes, can be obtained with probes biased to give the ion

<sup>2</sup>It might be possible to have  $T_{i\parallel} > 0.03$  eV because of (a) ion-ion scattering or (b) velocity-space instability[6]

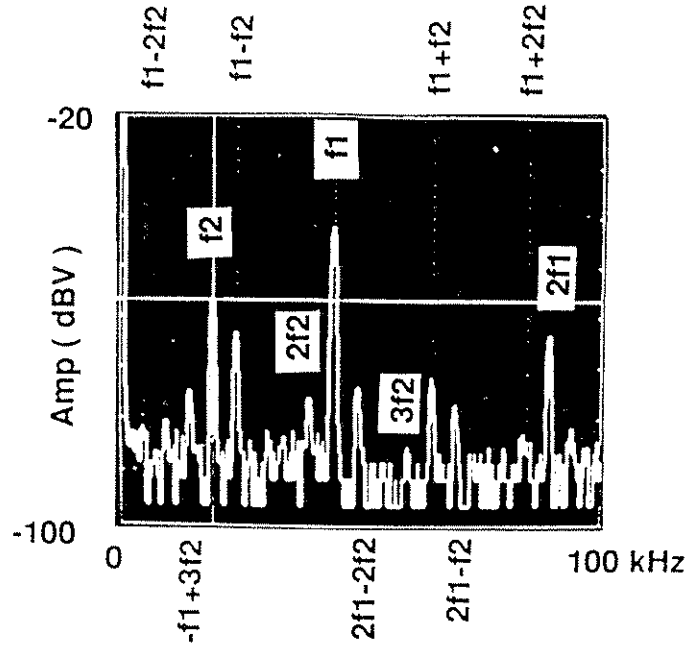


Figure 2.11: Typical instability frequency spectra.

saturation current. The real-time oscillating signals were recorded with a transient recorder (12 bits resolution and 2 MHz maximum sampling rate). The frequency spectra were obtained both by performing Fast Fourier Transforms (FFT) on each real-time signal and with a signal analyzer (Hewlett Packard model 3561A).

Figure 2.11 shows a typical frequency spectrum of the observed instabilities. Even though numerous frequency peaks appear, they are identified as two fundamental frequencies ( $f_1 = 44.25$  kHz and  $f_2 = 19.75$  kHz), their harmonic frequencies, and the various beat frequencies. In other words, the frequencies of these peaks are linear combinations of  $f_1$  and  $f_2$  given by  $f = m f_1 + n f_2$  ( $m, n = 0, \pm 1, \pm 2, \dots$ ). Here,  $f_{ci} = 6$  kHz,  $f_{pi} = 330$  kHz, and  $f_{ci} < f \ll f_{pi}$ .

We confirmed that no electron oscillations are excited in our experimental parameter region. When we increase the gas pressure above  $10^{-4}$  torr and the beam current above  $1000 \mu\text{A}$ , we could observe the electron plasma and cyclotron oscillations.

A plot of  $f_1$ ,  $f_2$  and  $f_s = f_1 - f_2$  versus  $I_p$  is shown in fig. 2.12(a). Since  $f_2$  has a stronger  $I_p$  dependence than  $f_1$ , the ratio  $f_1/f_2$  decreases with  $I_p$ , as shown in fig. 2.12(b). When  $f_1/f_2$  is 3, 2 or 1.5 ( $f_1/f_2 = 1.5$  implies  $f_1/f_s = 3$ ) we observe frequency locking. The amplitudes of  $M_1$ ,  $M_2$  and  $M_s$ , which are defined as  $n_1$ ,  $n_2$  and  $n_s$  respectively, are shown in fig. 2.12(c). We see that  $n_1$  increases monotonically with  $I_p$ , except for  $I_p = 3 \sim 4.2 \mu\text{A}$ , where  $M_2$  and  $M_s$  start growing from noise level. Furthermore,  $n_2$  is larger when  $f_1$  and  $f_2$  are locked. Larger  $n_2$  peaks appear at  $I_p = 25 \mu\text{A}$  and  $55 \mu\text{A}$  which correspond to  $f_1/f_2 = 3$  and 2, respectively. At  $I_p = 53.9 \mu\text{A}$ ,  $M_1$  and  $M_2$  are locked at  $f_1/f_2 = 2$ . At  $I_p > 74 \mu\text{A}$ ,  $M_1$  and  $M_2$  are unlocked and  $f_2$  is now larger than  $f_1/2$ . The largest locking region occurs when  $f_1/f_2 = 1.5$  as can be seen from fig. 2.12. Here  $f_2$  is now larger than  $f_s$ . Both  $M_2$  and  $M_s$  disappear at  $I_p = 410 \mu\text{A}$ . However,  $M_1$  is coherent at  $I_p > 410 \mu\text{A}$ .

A sequence of frequency spectra and frequency locking for an  $I_p$  scan is shown in fig. 2.13. Frequency locking at  $f_1/f_2 = 3.5$  (fig. 2.13(a)), 3 (fig. 2.13(d)) and 2 (fig. 2.13(e)) are observed. As previously mentioned, when two frequencies are locked,  $n_2$  increases. The  $f_1/f_2 = 2$  locking interval is longer than for 3.5 or 3, lasting from  $I_p = 30 \mu\text{A}$  to  $80 \mu\text{A}$ , above which  $M_2$  disappears. When  $M_1$  and  $M_2$  are unlocked, we find beat-frequency components. However, each component is coherent and we don't observe chaotic spectra in this sequence.

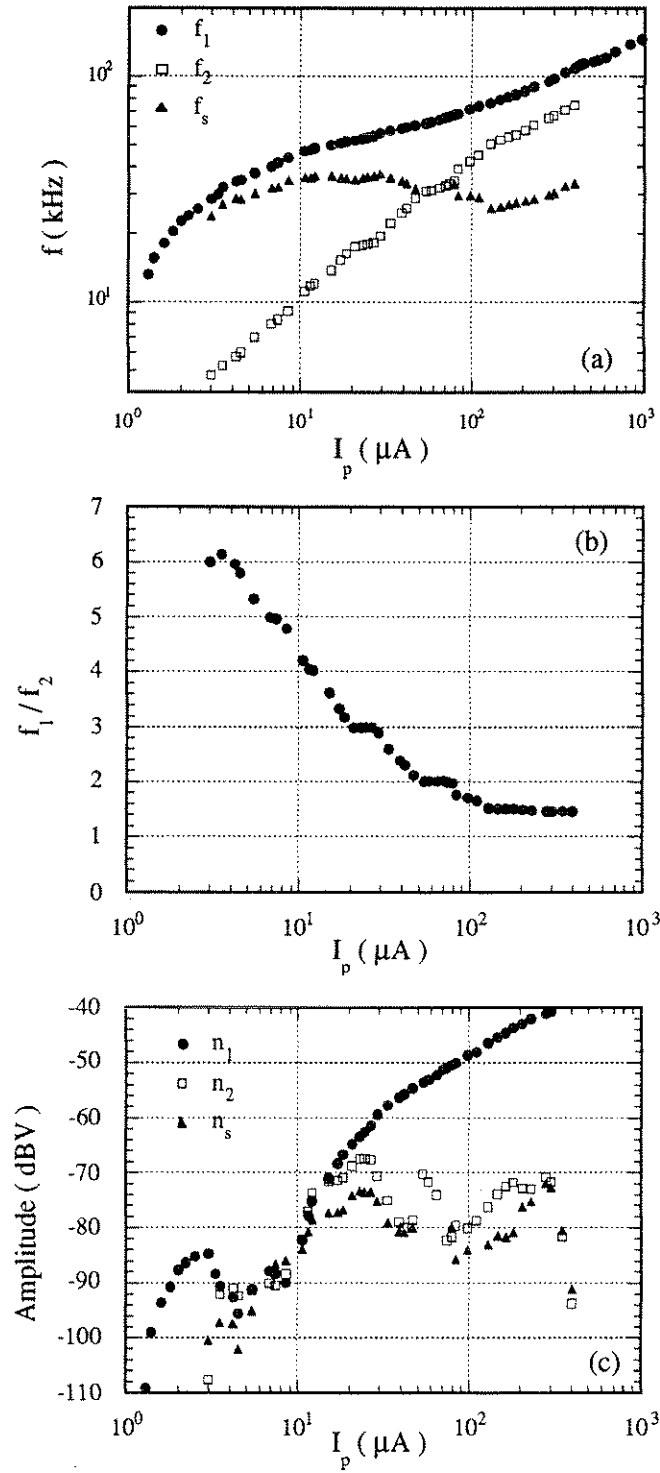


Figure 2.12:  $I_p$  dependence of (a) instability frequencies, (b)  $f_1/f_2$  and (c) amplitudes. Ar  $1 \times 10^{-5}$  torr,  $r = 0.3$  cm.



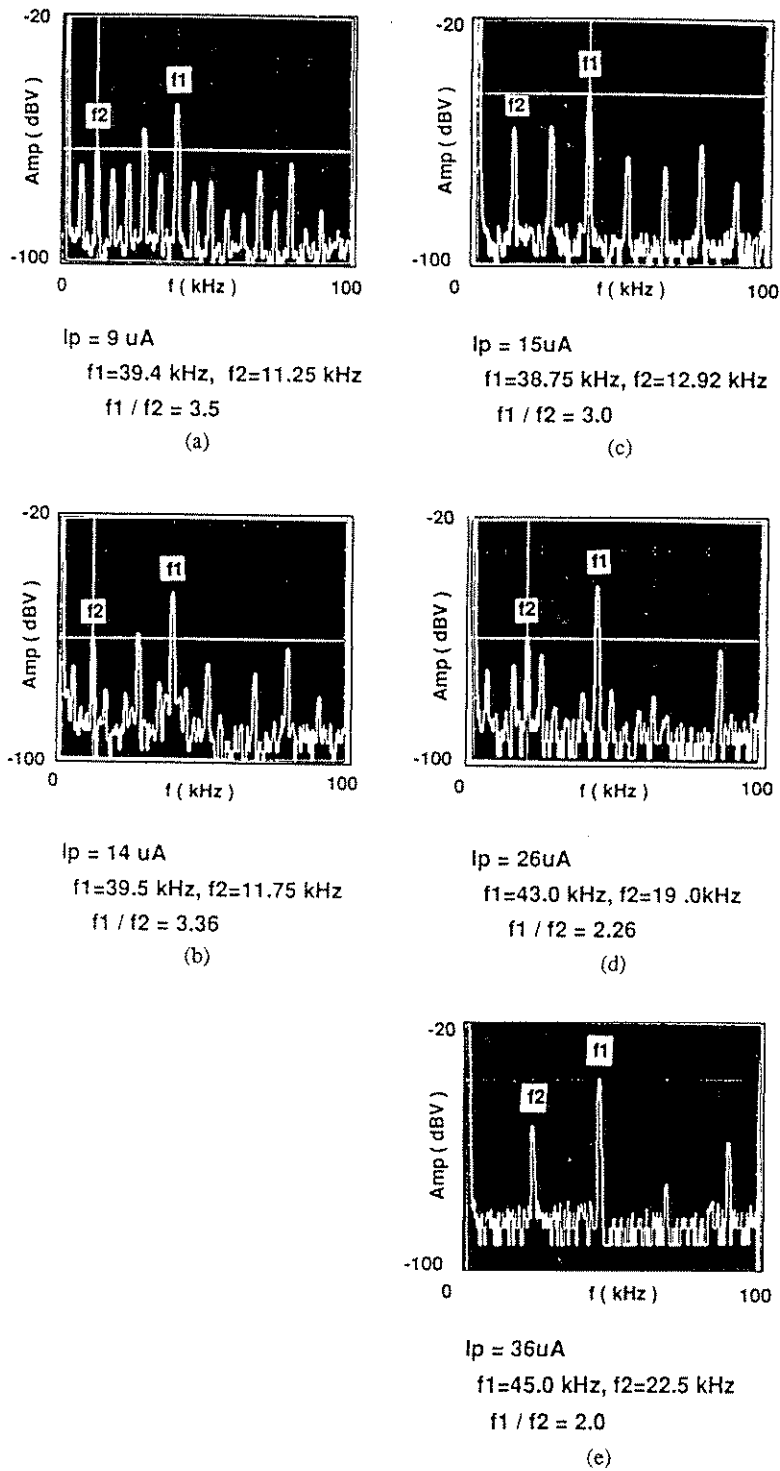


Figure 2.13:  $I_p$  dependence of a sequence of the frequency locking.  $\text{Ar } 2 \times 10^{-5}$  torr,  $r = 0.5 \text{ cm}$ .

The frequency locking sequence is also observed during pressure scans. Figure 2.14(a) shows the Ar pressure dependence of  $f_1$  and  $f_2$ . In this measurement,  $I_p$  was kept constant. Therefore  $n_b$  and  $n_e$  are nearly constant, while  $n_i$  is proportional to P (see fig. 2.5(b)). Figure 2.14(b) shows  $f_1/f_2$  versus P. Clear frequency locking at  $f_1/f_2 = 3, 2.5$  and  $2$  is observed. Comparing fig. 2.14(a) with (b), we see that  $f_2$  increases with P when no frequency locking occurs. In fig. 2.14(c),  $n_1$  and  $n_2$  are plotted versus argon pressure. Initially  $n_1$  increases with P, then starts decreasing at  $5 \times 10^{-5}$  torr. At this pressure, the frequency spectrum of  $M_1$  becomes broader, and the signal to noise ratio becomes smaller. Above  $7 \times 10^{-5}$  torr, the system is turbulent and we can no longer distinguish the frequency peaks of  $M_1$  and  $M_2$ . Therefore, in the region where  $M_1$  and  $M_2$  are coherent,  $n_1$  increases monotonically with P. On the other hand,  $n_2$  is determined mainly by the  $f_1/f_2$  ratio, as mentioned before. Figure 2.14(c) shows that an  $n_2$  peak exists at  $f_1/f_2 = 3$  and again at  $f_1/f_2 = 2$ .

The ion mass dependence of  $f_1$  and  $f_2$  versus  $I_p$  is shown in fig. 2.15(a). In fig. 2.15(a),  $f_1$  is replotted versus atomic mass ( $A_i$ ) for various  $I_p$  values. It is clear that  $f_1$  has  $1/\sqrt{M_i}$  dependence, while  $f_2$  has no ion mass dependence.  $M_i$  dependence of  $n_1$  is shown in fig. 2.16(a). We see that  $n_1$  is larger for the heavier gases. In fig. 2.16(b), we plot  $f_2$  versus  $n_1$ . We find that  $f_2$  scales as  $\sqrt{n_1}$ .

Figure 2.17 shows the radial profiles of frequencies and amplitudes. Experimental parameters are chosen so that no frequency locking occurs. As shown in fig. 2.17(a), the frequencies are almost constant from the beam center to the chamber wall, suggesting that the instabilities are global modes. Figure 2.17(b) shows that the  $n_1$  and  $n_s$  peaks are at the beam edge, while the  $n_2$  peak is at the beam center. We

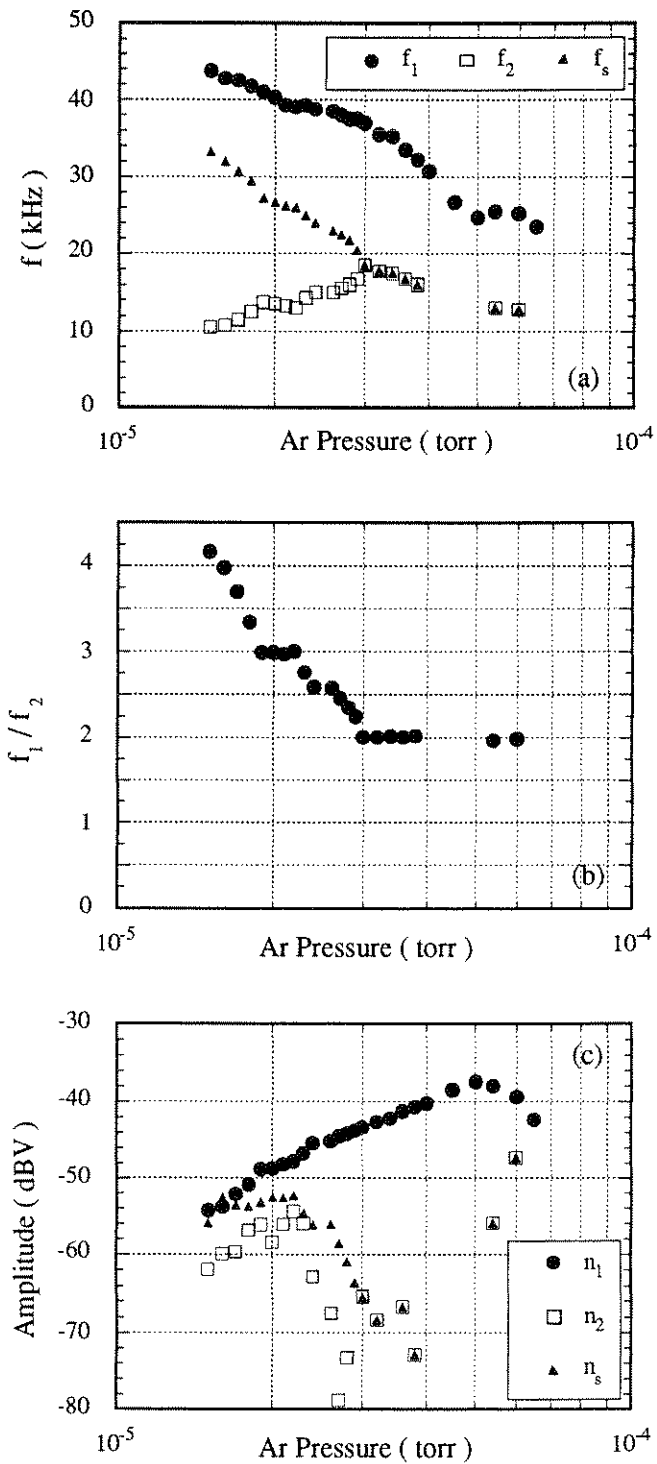


Figure 2.14: Ar pressure dependence of (a) instability frequencies, (b)  $f_1/f_2$ , and (c) amplitudes.  $I_p = 16 \mu\text{A}$ ,  $r = 0.5 \text{ cm}$ .

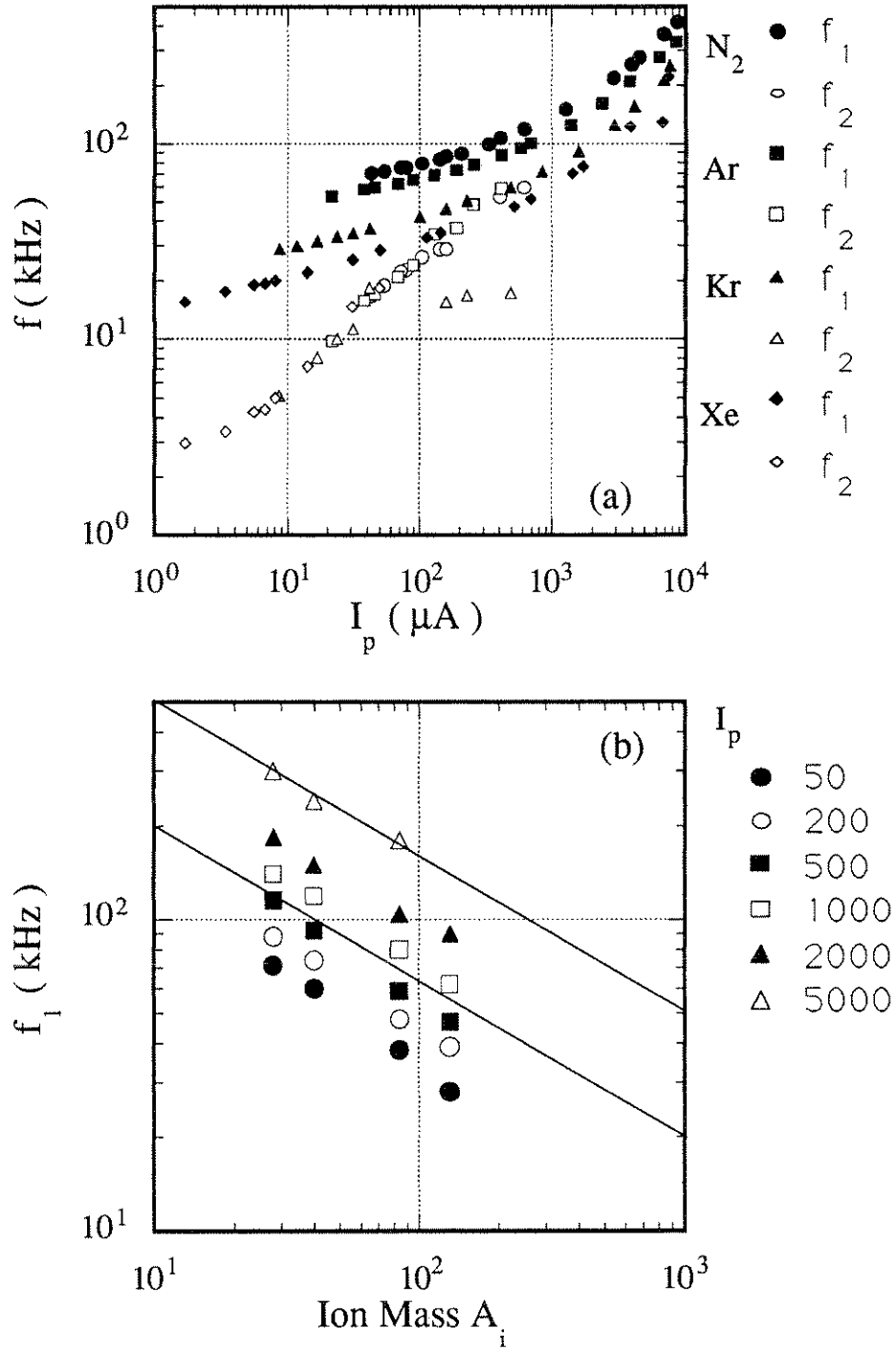


Figure 2.15: Ion mass dependence of instability frequencies. It is clear that  $f_1$  has  $1/\sqrt{M_i}$  dependence, while  $f_2$  has no ion mass dependence.  $P = 10^{-5}$  torr,  $r = 0.3$  cm.

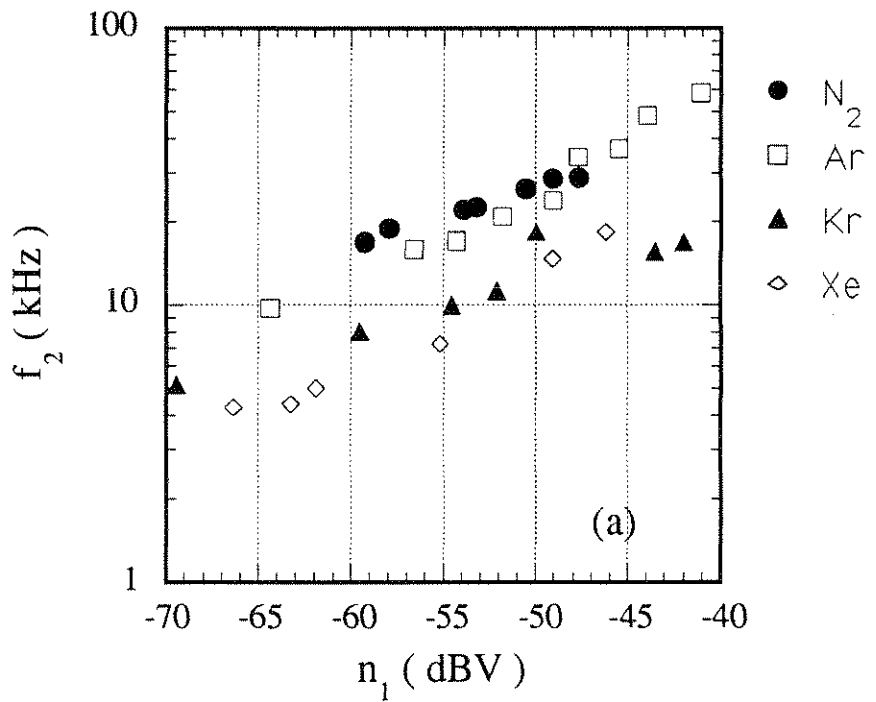
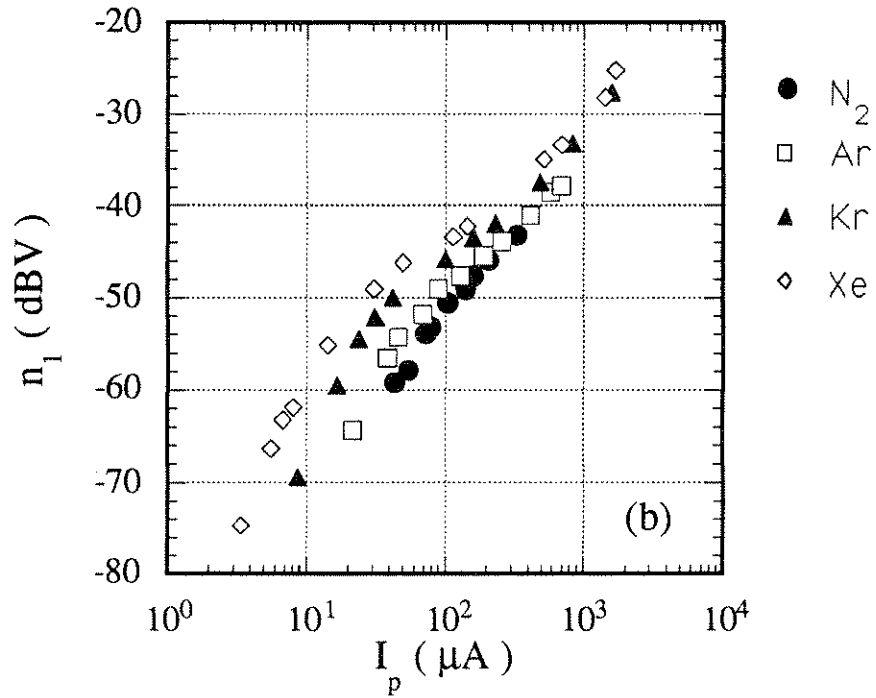


Figure 2.16: (a) Ion mass dependence of  $n_1$  VS  $I_p$ . We see that  $n_1$  is larger for the heavier gases. (b) Ion mass dependence of  $f_2$  VS  $n_1$ .  $P = 10^{-5}$  torr,  $r = 0.3$  cm.

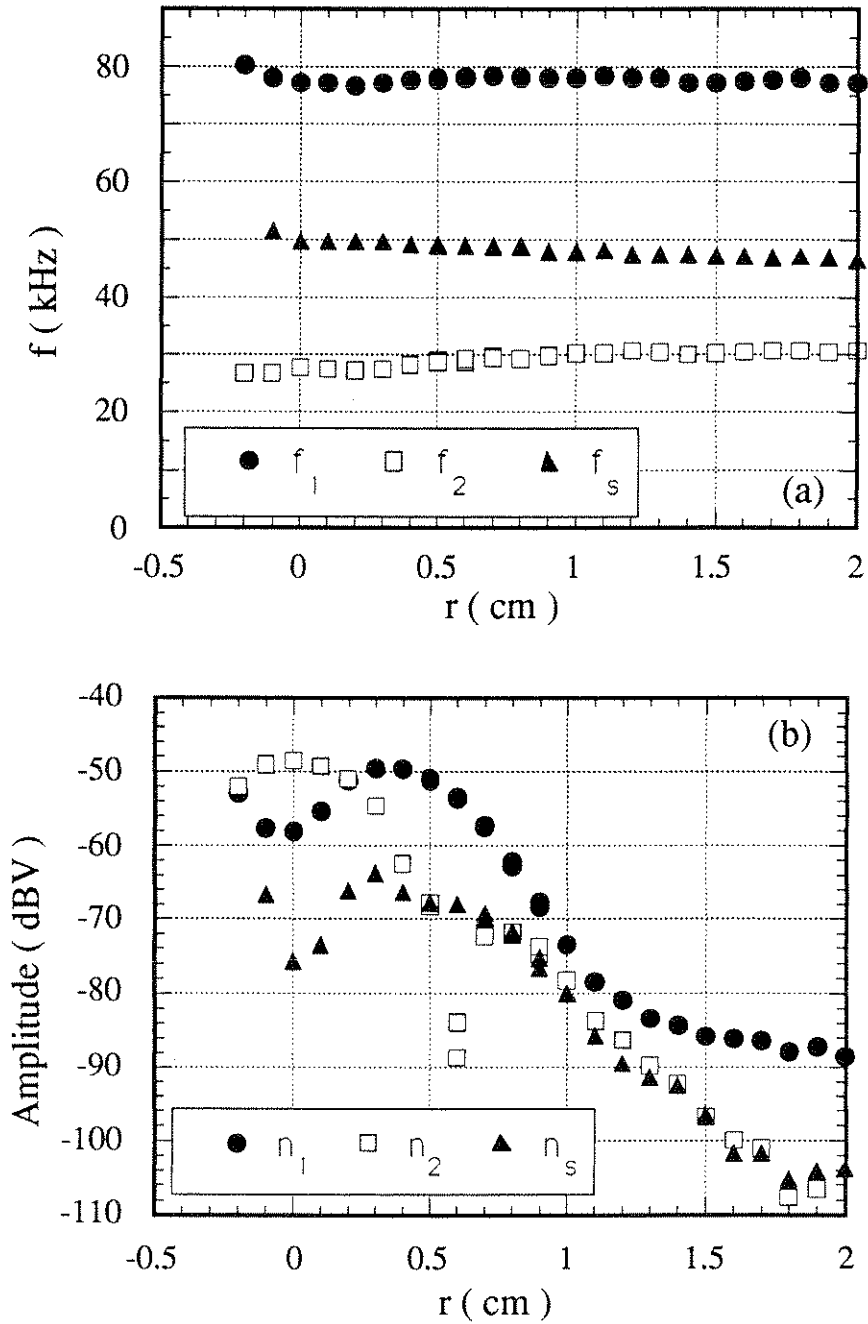


Figure 2.17: Radial profiles of (a) frequencies and (b) amplitudes. The  $n_1$  and  $n_s$  peaks are at the beam edge, while the  $n_2$  peak is at the beam center. Ar  $P = 1 \times 10^{-5}$  torr,  $I_p = 100 \mu\text{A}$ . The identical radial amplitude profiles are observed with a probe biased +30 V.

measured the radial profiles of  $n_1$ ,  $n_2$  and  $n_s$  for several experimental conditions by varying  $I_p$ , P, B,  $V_B$  and the gas species and with a positively biased (+30 V) probe. We observed the same profiles every time, with different amplitudes.

## 2.5 Wave Propagation Measurements

The azimuthal wave number of  $M_1$ ,  $k_{\theta 1}$ , was measured by three probes located at the same radial and axial position. From the phase difference between the probes, we concluded that  $M_1$  has the azimuthal mode number  $m = 1$  in the direction of the  $E \times B$  drift or electron diamagnetic drift. Thus,  $k_{\theta 1} = m/r_b = 2 \text{ cm}^{-1}$ . The  $k_z$  of  $M_1$  was determined by measuring the phase difference between the axially movable probe and the reference probe as a function of the axial position of the movable probe, to be of order  $k_{z1} \sim 0.03 \text{ cm}^{-1}$ .

Since  $n_1$  is larger than  $n_2$ , we need to use a low pass filter to measure wave numbers of  $M_2$ . An active filter which we used has a frequency response of  $V_{out}/V_{in}$  which falls 40 dBV (1/100) roughly 35 kHz from the cutoff frequency. The cutoff frequency of the filter is variable from 10 kHz to 30 kHz. The azimuthal and axial wave numbers of  $M_2$ ,  $k_{\theta 2}$  and  $k_{z2}$  respectively, were measured to be zero.

Figure 2.18(a) shows the phase shift between the radially movable probe and the reference probe as a function of the radial position of the movable probe. The reference probe is located at  $r = 0.7 \text{ cm}$  and the same axial position as the movable probe. A 180 degree phase jump was observed at  $r = 0.6 \text{ cm}$ . Figure 2.18(b) shows radial amplitude profiles of  $n_1$  and  $n_2$ , measured simultaneously with fig. 2.18(a). It is found that at the radial position where the jump in phase occurs,  $n_2$  shows

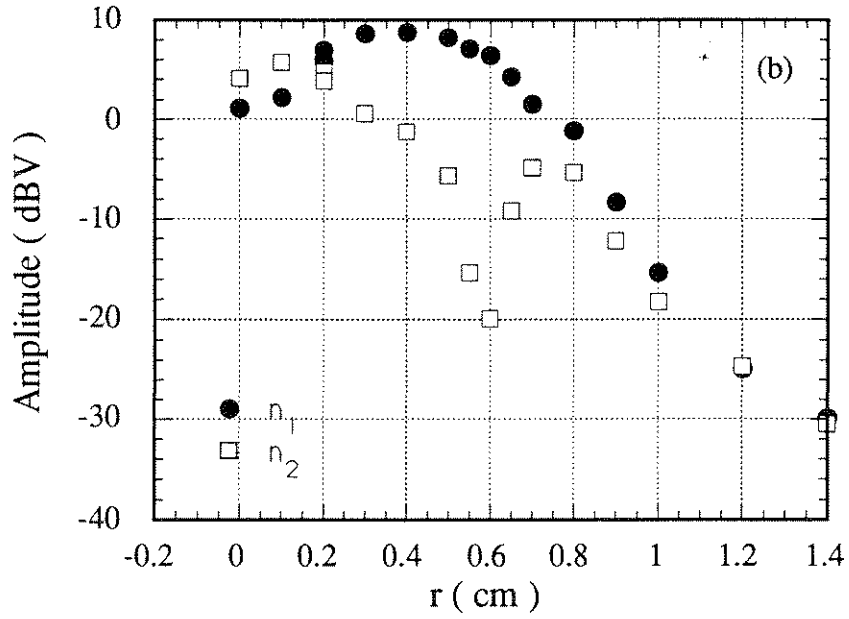
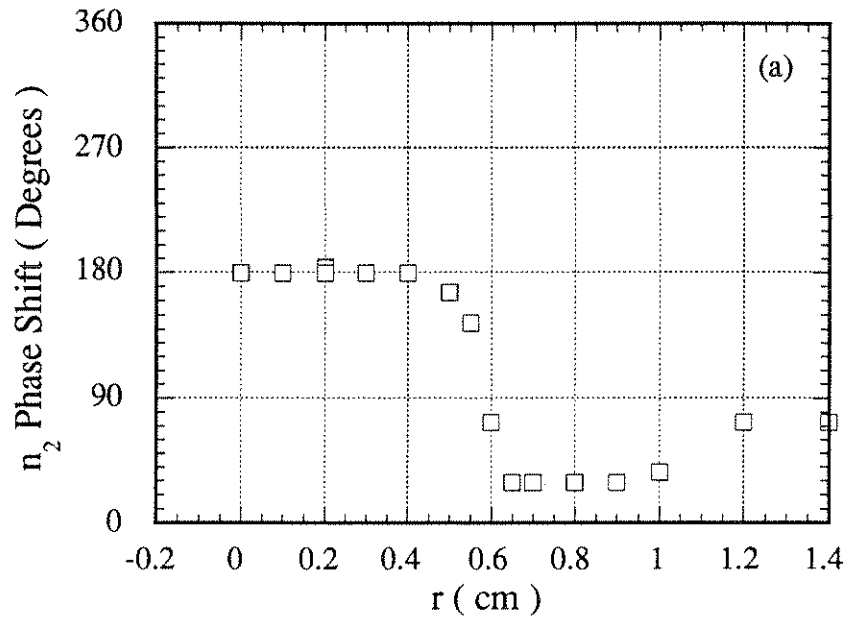


Figure 2.18: Radial phase shift of  $n_2$ .



- $M_1$  mode
  - $m = 1$  mode
  - $k_{z1} \approx 0.03 \text{ cm}^{-1}$
- $M_2$  mode
  - $m = 0$  mode
  - radially standing wave
  - $k_{z2} = 0$
- $M_s$  mode
  - $m = 1$  mode

Table 2.2: Wave numbers of instabilities

a dip in radial profile. We measured the phase shift and  $n_2$  profile simultaneously for several different experimental conditions, and observed the jump in phase and  $n_2$  dip at the same radial position every time. We could observe the identical  $n_2$  profile and the phase shift between two probes with +30 V bias case. One possible explanation is that  $M_2$  is a standing wave in radial direction and  $r = 0.6 \text{ cm}$  is the position where  $n_2$  is always zero.

Wave numbers of the side band mode,  $M_s$ , whose frequency is  $f_s = f_1 - f_2$ , were measured by choosing  $I_p$  and P so that  $f_s$  is lower than  $f_2$  and using the low pass filter. As a result of these measurements,  $k_{\theta s}$  is  $m = 1$  mode. Even when the frequency locking at  $f_1/f_2 = 3$  occurs,  $M_2$  is  $m = 0$  mode and  $M_1$  and  $M_s$  are  $m = 1$  modes. These results are consistent with the radial profiles of  $M_2$  and  $M_s$  shown in fig. 2.17, which shows an amplitude maximum of  $M_s$  peak at  $r = 0.3 \text{ cm}$  while that of  $M_2$  is at  $r = 0 \text{ cm}$ .

Table 2.2 summarizes the measured wave numbers.

## 2.6 Nonlinear Evolution Measurements

We have shown the excitation of the  $M_1$ ,  $M_2$  and  $M_s$  modes. When  $f_1/f_2$  is 4, 3, 2 or 1.5, we have observed the frequency locking phenomena. In this section we present a sequence of nonlinear evolutions when the frequencies are locked.

Figure 2.19(a) shows frequency spectra at  $f_1/f_2 = 3.13$ . In the figure  $f_1$  and  $f_2$  are unlocked, and many beat frequency components,  $mf_1 + nf_2$  ( $m, n = \pm 1, \pm 2, \dots$ ), are observed. Note that each component is coherent. When the plasma conditions are varied, the neutral density in this case,  $f_1$  and  $f_2$  are locked in frequency at  $f_1/f_2 = 3$  (fig. 2.19(b)). Once  $f_1$  and  $f_2$  are frequency-locked, a new mode,  $M_3$ , appears at a frequency  $f_3$  ( $f_3 < f_2, f_s < f_1$ ). This new mode grows and it is seen in fig. 2.19(c) for the  $f_3/f_2 = 2.28$  case. We also find beat frequency components,  $nf_2 + pf_3$  ( $n, p = \pm 1, \pm 2, \dots$ ). By varying the gas pressure slightly, we can control the frequency  $f_3$  with  $f_1$  and  $f_2$  locked in frequency. In fig. 2.19(d),  $f_3$  is now locked at  $f_3 = f_2/2 = f_1/6$ . Once  $f_3$  is locked, a new mode,  $M_4$ , emerges at a frequency  $f_4$  below  $f_3, f_2$ , and  $f_1$  (fig. 2.19(e)). We see that  $f_4$  is again frequency-locked with  $f_3, f_2$  and  $f_1$  (fig. 2.19(f)) and  $M_5$  appears at a frequency  $f_5$ . In fig. 2.19(g),  $f_5$  is locked at  $f_5 = f_4/2 = f_3/4 = f_2/8 = f_1/24$ . The nonlinear evolution which we have shown in fig. 2.19 is; (a) frequency locking between  $f_{n+1}$  and  $f_n$ , (b) an excitation of a new mode,  $M_{n+2}$ , at a frequency  $f_{n+2}$  ( $f_{n+2} < f_{n+1} < f_n$ ) ( $n = 1, 2, 3$ ). Finally when  $n > 3$ , any frequency unlocking can lead to a “chaotic looking” spectrum.

Figure 2.20(a) shows the case when  $f_1, f_2$  and  $f_3$  are locked while  $f_4$  and  $f_5$  are unlocked in frequency. We find a broadband background noise appears with

sharp  $f_1$ ,  $f_2$ , and  $f_3$  peaks. In fig. 2.19(b),  $f_1$  and  $f_2$  are also unlocked ( $f_1/f_1 = 3.12$ ).

We note that this spectral evolution can be controlled by changing either the neutral gas pressure or the electron beam current. Furthermore the appearance of each additional  $M_{n+2}$  mode requires smaller and smaller changes (increases) in either the pressure or the current. As we shall see later the physical origin of those  $M_{n+2}$  modes at present is not understood. The fact that they have a frequency  $f_{n+2} < f_{n+1} < f_n$  and that their frequencies can continuously track the frequency matching condition ( $f_{s_2} = f_1 \pm f_2$ ,  $f_{s_3} = f_1 \pm f_3$  and  $f_{s_{n+2}} = f_1 \pm f_{n+2}$  so on, where  $f_{s_{n+2}}$  is a sideband frequency of the  $M_{n+2}$  mode) implies that there must be a whole sea or continuum of kinetic ion modes which can be excited via the trapped particle modes (we discuss it in chapter 6), which gives rise to sideband modes to  $M_1$  at frequencies  $f_1 \pm f_b$  where  $f_b$  is the bounce frequency in the wave frame.

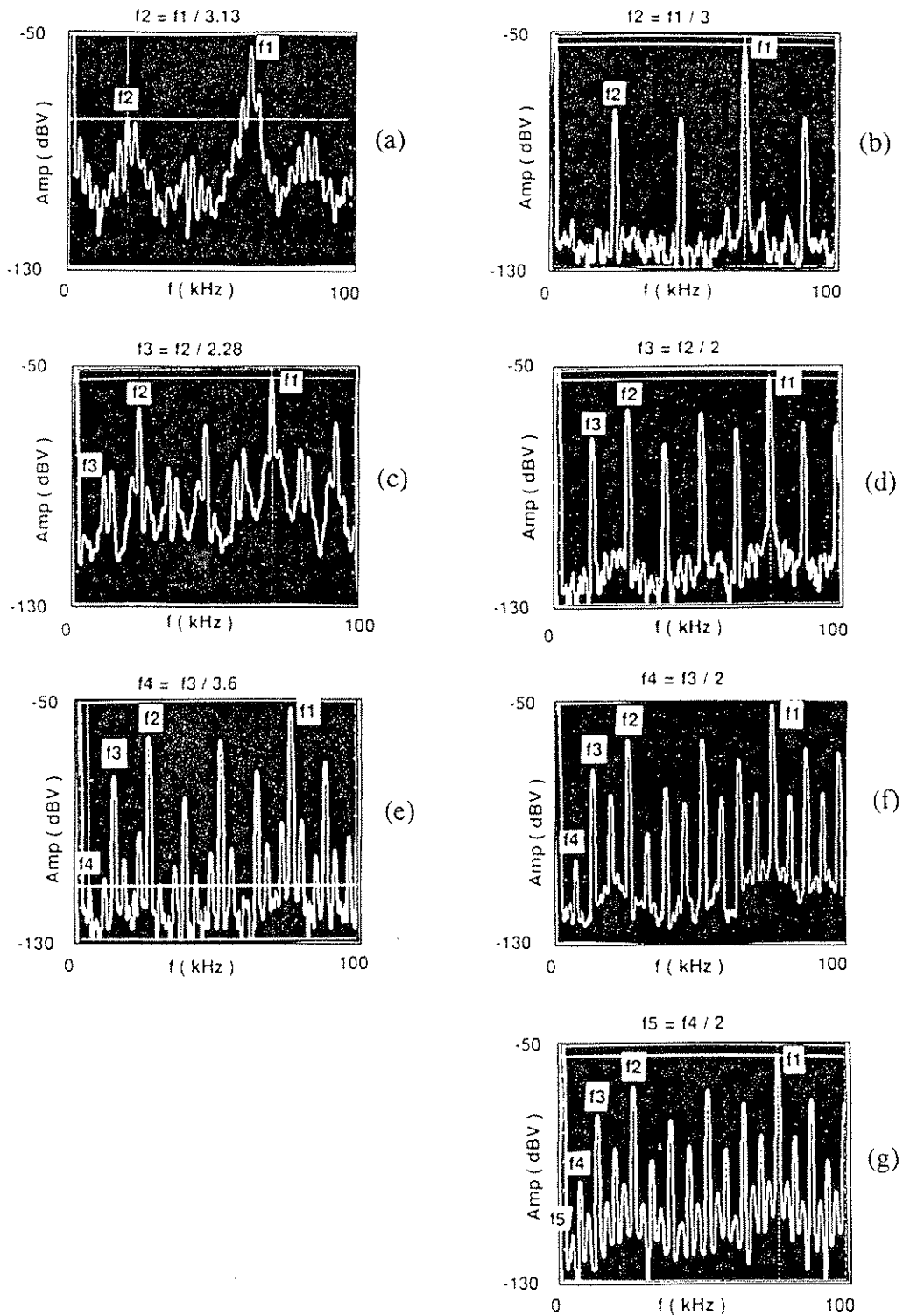


Figure 2.19: Nonlinear evolution of the instabilities (1)

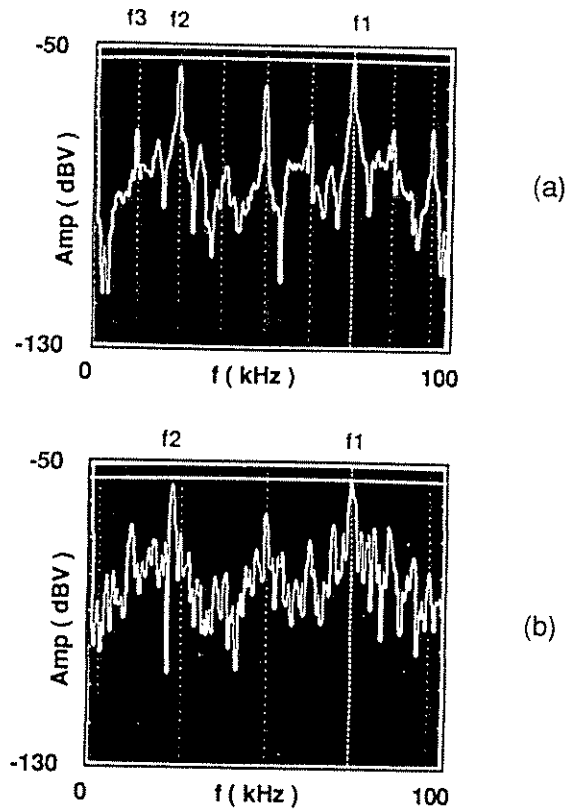


Figure 2.20: Nonlinear evolution of the instabilities (2). (a)  $f_1$ ,  $f_2$  and  $f_3$  are locked while  $f_4$  and  $f_5$  are unlocked in frequency. We find a broadband background noise appears with sharp  $f_1$ ,  $f_2$ , and  $f_3$  peaks. (b)  $f_1$  and  $f_2$  are also unlocked ( $f_1/f_2 = 3.12$ ).

# Chapter 3

## Theory of the Modified Simon-Hoh Instability

### 3.1 Introduction

In the previous chapter, we have shown experimental observations of intermediate frequency instabilities;  $M_1$ ,  $M_2$  and  $M_s$  modes. In this chapter we describe the theory of the  $M_1$  mode. As will be seen shortly, we have identified the  $M_1$  mode as a new electrostatic instability and named it as the modified Simon-Hoh instability (MSHI).

This chapter is organized as follows: First, we review the experimental observations of electrostatic instabilities in section 3.2; section 3.3 describes the physical picture of the MSHI; in section 3.4 and 3.5, the fluid and kinetic theories of the MSHI are shown, respectively; section 3.5 describes the comparison of the MSHI and other instabilities.

## 3.2 Review of Experimental Observation of Electrostatic Instabilities

Electrostatic waves excited by the interaction of an electron beam with a plasma have been studied for many years, both for high frequency electron oscillations[7] and low frequency ion oscillations[8]-[14]. Matitti et al.[8] observed an instability in the vicinity of the ion cyclotron frequency,  $f_{ci}$ , in their electron beam created plasma. The instability mechanism was explained as the interaction between the slow cyclotron wave on the beam and the forward plasma wave near  $f_{ci}$  with warm plasma electrons. Vermeer et al.[9] observed an instability near the ion plasma frequency,  $f_{pi}$ , excited by the slow cyclotron wave on the beam. Papadopoulos and Palmadesso[10] predicted the excitation of lower hybrid waves by the Landau growth mechanism when the injected beam velocity and the parallel phase velocity of the instabilities satisfy the resonance condition,  $\omega/k_{\parallel} \approx v_b$ . These instabilities[8]-[10] are excited by the direct coupling between electron beams and ion waves.

On the other hand, ion waves excited in the beam-plasma system by the  $E \times B$  current have been reported[11]-[14]. Kitagawa et al.[11] studied the flute-like drift instability in a hollow cylinder electron beam created plasma. Yamada and Owens[12] observed the modified two-stream instability at the lower hybrid frequency excited by the electron  $E \times B$  rotation. Wall et al.[13] observed the ion Bernstein wave excited by the  $E \times B$  current in their Q-machine plasma and an electron beam interaction experiment. Boswell[14] reported an instability that arose from a Kelvin-Helmholtz instability driven by an  $E \times B$  shear flow. The

instability frequency is the ion plasma frequency for the neutralized electron beam with  $n_i = n_b$ .

Intermediate frequency ( $\omega_{ci} \ll \omega \ll \omega_{ce}$ ) electrostatic instabilities driven by the relative electron-ion drift across an external axial magnetic field have been studied by many authors[11, 12, 15, 16, 17]. One such instability is the modified two-stream instability (MTSI) with finite  $k_z$  ( $k_z \ll k_y$ )[12, 15, 16], and the other is the flute-like drift instability (FDI) with  $k_z = 0, k_n \neq 0$ [11, 15, 17]. Here,  $k_z$  and  $k_y$  are parallel and perpendicular wave numbers, respectively, and  $k_n = \frac{1}{n_0} \frac{dn_0}{dx}$ . Both of these have instability frequencies on the order of the lower hybrid frequency,  $\omega_{LH}$ . Growth rates of the instabilities are also on the order of  $\omega_{LH}$ .

Fridman predicted an Anti-drift Instability which is also an intermediate frequency ( $\omega_{ci} \ll \omega \ll \omega_{ce}$ ) electrostatic instability in a weakly ionized inhomogeneous plasma with cold ( $T_i = 0$ ) unmagnetized ions[18].

Simon[19] and Hoh[20] studied the Simon-Hoh instability (SHI) in a weakly ionized, inhomogeneous, collisional, magnetized plasma under a strong electric field perpendicular to the DC magnetic field. The SHI is unstable when the density gradient and the electric field are in the same direction, and is triggered by the difference between the electron and ion  $E \times B$  drift velocities caused by collisions. The SHI was observed by Thomassen[21] in a hot cathode Penning discharge plasma. In collisionless, weakly magnetized-ion plasmas (electrons are magnetized) a similar instability is excited due to the slower ion drift velocity caused by a large ion Larmor radius.

The modified Simon-Hoh instability (MSHI) which we observed in the electron beam produced plasma does not correspond to any instability shown above, i.e.,



no instability shown above agrees with the measured  $I_p$  (fig. 2.12), P (fig. 2.14) and B (Figure 4.1(c)) dependences of the instability frequency at  $\omega_{ci} \ll \omega \ll \omega_{ce}$ . This instability occurs when there is a DC radial electric field in the plasma and when this field and the density gradient are in the same direction. In such a plasma the MSHI is driven unstable due to a difference between the electron and ion azimuthal drift velocities. We point out that this new instability is similar to the Simon-Hoh Instability (SHI)[19]-[21]. Therefore, first we discuss briefly the physical picture of the SHI and then explain the MSHI.

### 3.3 Physical Picture of the MSHI

#### 3.3.1 Simon-Hoh Instability

The SHI is an instability in a weakly ionized, collisional ( $\omega \ll \nu_{en}, \nu_{in}$ ) plasma with an axial magnetic field and a radial DC electric field. See Table 2.1 for an explanation of the various symbols and their typical values in our experiment. The SHI occurs when both ions and electrons are magnetized, the density is nonuniform ( $\nabla n_0 \neq 0$ ) in the direction of the electric field ( $E_{r0}$ ), and when the sign of the product of the electric field and the density gradient is positive ( $\nabla n_0 \cdot \vec{E}_{r0} > 0$ ). Figure 3.1 shows the physical picture of the SHI. The instability mechanism of the SHI is as follow: Under the DC axial  $B_0$  field and the radial  $E_{r0}$  field, both electrons and ions rotate with  $E_{r0} \times B_0$  drift velocity,

$$v_{Ej} = \frac{E_{r0}/B_0}{1 + \frac{1}{\Omega_j^2 r_{jn}^2}} \quad (3.1)$$

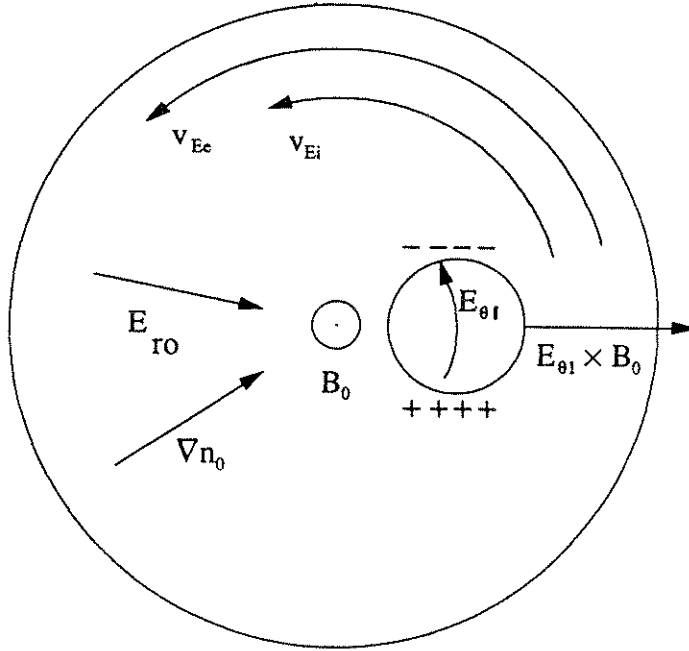


Figure 3.1: The physical picture of the SHI.

where,  $j = e$  (electron) or  $i$  (ion),  $\Omega_j$  is the cyclotron frequency and  $\tau_{jn}$  is the collision time with the neutral gas. Since  $\Omega_e^2 \tau_{en}^2 \gg 1$  and  $\Omega_i^2 \tau_{in}^2 \geq 1$ , we get

$$v_{Ee} = \frac{E_{r0}}{B_0} \quad (3.2)$$

$$v_{Ei} = \frac{E_{r0}/B_0}{1 + \frac{1}{\Omega_i^2 \tau_{in}^2}}. \quad (3.3)$$

This difference between the electron and ion  $E \times B$  drift velocities causes a charge separation in the  $\theta$  direction, and consequently produces an azimuthal electric field,  $E_{\theta 1}$ . When the plasma density is inhomogeneous and  $\nabla n_0 \cdot \vec{E}_{r0} > 0$ , then the  $E_{\theta 1} \times B_0$  velocity enhances the density perturbation. The instability frequency of the SHI is on the order of  $v_{Ee} k_\theta$ .

### 3.3.2 Modified Simon-Hoh Instability

The modified Simon-Hoh Instability (MSHI) is different from the usual SHI in that, (a) ions are unmagnetized and (b) both electrons and ions are collisionless. Therefore, the azimuthal velocity of the ions is not expressed by eq. (3.3). A velocity difference between electrons and ions is caused by the large ion Larmor radius effect. In our experiment the ions are unmagnetized because of the small axial B field. Furthermore, because of the large DC radial electric field, they move radially in and out across the B field. Therefore, the ion orbit is nearly a straight line. As the ions pass the vicinity of the center of the plasma, they are pushed outwards due to the  $v \times B$  force. Even though this perturbation of the ion orbit from a straight line is small, we cannot neglect the curvature. If we average over many ions, they always pass the center in the direction of the  $E_{r0} \times B_0$  drift. This is the ion azimuthal drift velocity which is smaller than the electron  $E_{r0} \times B_0$  velocity. The slower azimuthal drift velocity of ions causes a charge separation in the  $\theta$  direction; the consequent azimuthal electric field,  $E_{\theta 1}$  and the enhancement of the density perturbation by the  $E_{\theta 1} \times B_0$  velocity are the same as in the SHI case.

## 3.4 Fluid Theory of the MSHI

In this section, first we derive a general expression for the electrostatic oscillations (eq. (3.10)), which includes effects of the B fields, DC electric fields, plasma temperatures, density gradients and collisions. We show the dispersion relations of several well known instabilities from the equation by choosing correct plasma

conditions. Then we apply our experimental conditions to the equation and show the dispersion relation of the MSHI.

### 3.4.1 General Fluid Theory

We consider the following model: We take a Cartesian geometry with a uniform magnetic field  $\vec{B}_0 = B_0 \hat{z}$ . We look for electrostatic oscillations of potential  $\phi$  and amplitude  $n_1$  given by,

$$\phi = \phi(x) e^{i(k_y v_y + k_z v_z - \omega t)} \quad (3.4)$$

$$n_1 = n_1(x) e^{i(k_y v_y + k_z v_z - \omega t)} \quad (3.5)$$

and the fluctuating electric field is given by,

$$E_{1x} = -\frac{d\phi}{dx} = -\phi', \quad (3.6)$$

$$E_{1y} = -ik_y \phi. \quad (3.7)$$

The DC electric field and density are  $\vec{E}_0 = E_0 \hat{x}$  and  $n_0 = n_0(x)$ , respectively. The density gradient is  $k_n = \left| \frac{n'_0}{n_0} \right| = \left| \frac{1}{n_0} \frac{dn_0}{dx} \right|$ , where  $n'_0 < 0$ . We use the equations of motion

$$\begin{aligned} n_{j0} m_j \left[ \frac{\partial \vec{v}_{j1}}{\partial t} + (\vec{v}_{j0} \cdot \vec{\nabla}) \vec{v}_{j1} \right] = \\ s_j e n_{j0} (\vec{E}_1 + \vec{v}_{j1} \times \vec{B}_0) + s_j e n_{j1} (\vec{E}_0 + \vec{v}_{j0} \times \vec{B}_0) \\ - \kappa T_j \nabla n_{j1} - \kappa T_j \frac{n'_{j0}}{n_{j0}} n_1 - m_j n_{j0} \vec{v}_{j1} \nu_j, \end{aligned} \quad (3.8)$$

and the continuity equation

$$\frac{\partial n_{j1}}{\partial t} + (\vec{v}_{j0} \cdot \vec{\nabla}) n_{j1} + n_{j0} \vec{\nabla} \cdot \vec{v}_{j1} + (\vec{v}_{j1} \cdot \vec{\nabla}) n_{j0} = 0, \quad (3.9)$$

for plasma ions, plasma electrons and beam electrons, together with the local approximation,  $\phi'' = \phi' = 0$  and  $n_1'' = n_1' = 0$ , where  $j = i$  (ion),  $e$  (plasma electron) and  $b$  (beam electron),  $s_i = 1$ ,  $s_e = s_b = -1$ ,  $\nu_j$  is the collision frequency. Since collisions in the perpendicular equation give classical diffusion which is negligible, we consider collisions only in the  $\hat{z}$  direction. We find,

$$\frac{n_{j1}}{n_{j0}} = \frac{s_j e \phi}{m_j} \frac{\frac{k_y^2}{\bar{\omega}^2 - \Omega_j^2} + \frac{k_z^2}{\bar{\omega}^2 + i\nu_j \bar{\omega}} - \frac{s_j \Omega_j k_{nj} k_y / \bar{\omega}}{\bar{\omega}^2 - \Omega_j^2}}{1 - \frac{T_j}{m_j} \left[ \frac{k_y^2}{\bar{\omega}^2 - \Omega_j^2} + \frac{k_z^2}{\bar{\omega}^2 + i\nu_j \bar{\omega}} - \frac{s_j \Omega_j k_{nj} k_y / \bar{\omega}}{\bar{\omega}^2 - \Omega_j^2} \right]} \quad (3.10)$$

where,  $\Omega_j = |s_j e B_0 / m_j|$  is the cyclotron frequency and  $\bar{\omega}_j = \omega - \vec{k} \cdot \vec{v}_{j0}$ . The drift term  $\vec{k} \cdot \vec{v}_{j0}$  is expressed as

$$\vec{k} \cdot \vec{v}_{b0} = k_z v_{beam} + k_y v_{E \times B e} + k_y v_{bd} = k_z v_{beam} + \omega_{Eb} + \omega_b^* \quad (3.11)$$

$$\vec{k} \cdot \vec{v}_{e0} = k_y v_{E \times B e} + k_y v_{ed} = \omega_{Ee} + \omega_e^* \quad (3.12)$$

$$\vec{k} \cdot \vec{v}_{i0} = k_y v_{E \times B i} + k_y v_{id} = \omega_{Ei} + \omega_i^* \quad (3.13)$$

where  $\omega_{Ej} = k_y v_{E \times B j}$  is the  $E \times B$  drift frequency and  $\omega_j^* = k_y v_{jd} = -s_j \frac{T_j}{e B_0} k_{nj} k_y$  is the diamagnetic drift frequency. For convenience we use  $\omega_E$  and  $\omega^*$  for the electron  $E \times B$  and the electron diamagnetic drift frequency, respectively.

Before applying eq. (3.10) to our experiment, we derive some well known dispersion relations from it for several different plasma parameter regions. First, we show the density-potential relations for plasma electrons and ions.

### 1. Electrons

Consider magnetized electrons ( $\bar{\omega}^2 \ll \Omega_e^2$ ). Equation (3.10) is reduced to

$$\frac{n_{e1}}{n_{e0}} = -\frac{e \phi}{T_e} \frac{\frac{T_e}{m} \left[ -\frac{k_y^2}{\Omega_e^2} + \frac{k_z^2}{\bar{\omega}^2 + i\nu_e \bar{\omega}} - \frac{k_{ne} k_y}{\bar{\omega} \Omega_e} \right]}{1 - \frac{T_e}{m} \left[ -\frac{k_y^2}{\Omega_e^2} + \frac{k_z^2}{\bar{\omega}^2 + i\nu_e \bar{\omega}} - \frac{k_{ne} k_y}{\bar{\omega} \Omega_e} \right]} \quad (3.14)$$

(a) When  $T_e \simeq 0$ , the square bracket in the denominator of eq. (3.14) is neglected. Together with  $\nu_e \simeq 0$ , we find

$$\frac{n_{e1}}{n_{e0}} = \frac{e\phi}{m} \left[ \frac{k_y^2}{\Omega_e^2} - \frac{k_z^2}{\bar{\omega}^2} + \frac{k_{ne}k_y}{\Omega_e\bar{\omega}} \right], \quad (3.15)$$

where  $\bar{\omega} = \omega - \omega_E$ .

i. When  $k_{ne} \simeq 0$ , this reduces to

$$\frac{n_{e1}}{n_{e0}} = \frac{e\phi}{m} \left[ \frac{k_y^2}{\Omega_e^2} - \frac{k_z^2}{\bar{\omega}^2} \right]. \quad (3.16)$$

ii. When  $k_z \simeq 0$ , this reduces to

$$\frac{n_{e1}}{n_{e0}} = \frac{e\phi}{m} \left[ \frac{k_y^2}{\Omega_e^2} + \frac{k_{ne}k_y}{\Omega_e\bar{\omega}} \right]. \quad (3.17)$$

(b) When  $T_e \neq 0$  and  $c_e^2 k_y^2 \ll \Omega_e^2$  ( $c_e^2 = T_e/m$ ), we neglect the first term in the square bracket in eq. (3.14)

$$\frac{n_{e1}}{n_{e0}} = -\frac{e\phi}{T_e} \frac{\frac{T_e}{m} \left[ \frac{k_z^2}{\bar{\omega}^2 + i\nu_e\bar{\omega}} - \frac{k_{ne}k_y}{\bar{\omega}\Omega_e} \right]}{1 - \frac{T_e}{m} \left[ \frac{k_z^2}{\bar{\omega}^2 + i\nu_e\bar{\omega}} - \frac{k_{ne}k_y}{\bar{\omega}\Omega_e} \right]}, \quad (3.18)$$

where  $\bar{\omega} = \omega - \omega_E - \omega^*$ .

i. When  $\bar{\omega}/k_z \ll c_e$  and  $\nu_e \simeq 0$ ; electrons can freely move along the B field and establish a thermodynamic equilibrium. Since the first term in the square bracket in eq. (3.18) is dominant, it is reduced to the Boltzmann relation

$$\frac{n_{e1}}{n_{e0}} = \frac{e\phi}{T_e}. \quad (3.19)$$

ii. When  $\nu_e \simeq 0$  and  $k_z \simeq 0$ ; we find the modified Boltzmann relation for the  $k_z = 0$  case

$$\frac{n_{e1}}{n_{e0}} = \frac{e\phi}{T_e} \frac{\omega^*}{\omega - \omega_E}, \quad (3.20)$$

iii. When  $\nu_e \gg \bar{\omega}$  and  $k_z \neq 0$ ; one finds the modified Boltzmann relation

$$\frac{n_{e1}}{n_{e0}} = \frac{e\phi}{T_e} \frac{\omega^* + ik_z^2 c_e^2 / \nu_e}{\omega - \omega_E + ik_z^2 c_e^2 / \nu_e}, \quad (3.21)$$

where  $c_e^2 = T_e/m$ .

## 2. Ions

When  $T_i = 0$ ,  $\nu_i = 0$  and  $\vec{k} \cdot \vec{v}_{i0} \simeq 0$ ; eq. (3.10) is reduced to

$$\frac{n_{i1}}{n_{i0}} = \frac{e\phi}{T_e} \left[ \frac{c_s^2 k_y^2}{\omega^2 - \Omega_i^2} + \frac{c_s^2 k_z^2}{\omega^2} - \frac{c_s^2 \Omega_i k_{ni} k_y / \omega}{\omega^2 - \Omega_i^2} \right], \quad (3.22)$$

where  $c_s^2 = T_e/M$ .

(a) When ions are unmagnetized ( $\omega \gg \Omega_i$ ), this reduces to

$$\frac{n_{i1}}{n_{i0}} = \frac{e\phi c_s^2 k^2}{T_e \omega^2}. \quad (3.23)$$

(b) When ions are weakly magnetized ( $\omega \geq \Omega_i$ ) and  $k_y \gg k_z, k_{ni}$ , this reduces to

$$\frac{n_{i1}}{n_{i0}} = \frac{e\phi c_s^2 k_y^2}{T_e \omega^2 - \Omega_i^2}. \quad (3.24)$$

(c) When ions are strongly magnetized ( $\omega \ll \Omega_i$ ), this reduces to

$$\frac{n_{i1}}{n_{i0}} = \frac{e\phi}{T_e} \left[ -\frac{c_s^2 k_y^2}{\Omega_i^2} + \frac{c_s^2 k_z^2}{\omega^2} + \frac{\omega^*}{\omega} \right], \quad (3.25)$$

where we assumed  $k_{ni} = k_{ne}$ .

i. When  $k_z/k_y \gg \omega/\Omega_i$  or the ion Larmor radius for  $T_e$  is small ( $b = c_s^2 k_y^2 / \Omega_i^2 \ll 1$ ), the first term on the right hand side of eq. (3.25) is neglected and we find

$$\frac{n_{i1}}{n_{i0}} = \frac{e\phi}{T_e} \left[ \frac{c_s^2 k_z^2}{\omega^2} + \frac{\omega^*}{\omega} \right]. \quad (3.26)$$

ii. When  $k_z/k_y \ll \omega/\Omega_i$ , we find

$$\frac{n_{i1}}{n_{i0}} = \frac{e\phi}{T_e} \left[ -\frac{c_s^2 k_y^2}{\Omega_i^2} + \frac{\omega^*}{\omega} \right]. \quad (3.27)$$

Now by using the equations shown above together with the plasma approximation ( $n_{e1} = n_{i1}$ ) or Poisson's equation, we derive well known dispersion relations.

- When both electrons and ions are magnetized ( $\omega \ll \Omega_i \ll \Omega_e$ )
  - When the axial ion motion is important, and  $c_e$  is large enough to satisfy the Boltzmann relation for the electrons (even though  $k_n \neq 0$ ); eq. (3.19) and eq. (3.26) together with the plasma approximation give a dispersion relation for the collisionless drift wave[22]

$$\omega^2 - \omega^* \omega - c_s^2 k_z^2 = 0. \quad (3.28)$$

- When electron collisions (electron-neutral or electron-ion collisions) are important while the ion axial motion is unimportant, the modified Boltzmann relation (eq. (3.21)) and eq. (3.27) together with the plasma approximation give the dispersion relation for the collisional drift wave[4]

$$\omega^2 + i\sigma_{||}(\omega - \omega^*) = 0, \quad (3.29)$$

where  $\sigma_{||} = \frac{k_z^2}{k_y^2} \frac{\Omega_e \Omega_i}{\nu_e}$  and  $b \ll 1$  is assumed.

- When electrons are magnetized while ions are unmagnetized ( $\Omega_i \ll \omega \ll \Omega_e$ )
  - When  $T_e \simeq 0$  and electron collisions are unimportant
    - \* When  $k_{ne} \simeq 0$ , eq. (3.16) and eq. (3.23) together with Poisson's equation give the modified two-stream instability[12, 15, 16].



\* When  $k_z \simeq 0$ , eq. (3.17) and eq. (3.23) give the flute-like drift instability[11, 15, 17].

– When  $T_e \neq 0$ ,  $k_{ne} \neq 0$

\* When electron collisions are unimportant and  $E_0 = 0$ , eq. (3.20) and eq. (3.23) give the stable anti-drift mode[18]

$$\omega = \frac{c_s^2 k^2}{\omega^*}. \quad (3.30)$$

\* When electron collisions are important ( $\omega \ll k_z^2 c_e^2 / \nu_e$ ) and  $E_0 = 0$ , eq. (3.21) and eq. (3.23) give the ion-sound instability[22]

$$\omega \approx c_s k_{\perp} (1 + i\omega^* \nu_e / 2k_z^2 c_e^2). \quad (3.31)$$

### 3.4.2 MSHI Theory

Now we apply our experimental conditions to eq. (3.10). In our experiment the following plasma conditions are present; (a) electrons are magnetized while ions are weakly magnetized ( $\Omega_i \leq \omega \ll c_e k_y \ll \Omega_e$ ), (b) ions and beam electrons are cold ( $T_i, T_b \simeq 0$ ) while plasma electrons are not ( $T_e \neq 0$ ), (c) the plasma is weakly ionized, however, the collisions with neutral atoms are negligible ( $\nu_{en}, \nu_{in} \simeq 0$ ), and (d)  $k_{ne} = k_{nb} \geq k_y \gg k_z, k_{ni}$ . Plasma electrons are expressed by the modified Boltzmann relation, eq. (3.20); beam electrons follow eq. (3.15) with the third term in the square bracket being dominant because of small  $k_z$  and large  $\Omega_e$ ; plasma ions are reduced to eq. (3.24) with non-zero  $E \times B$  drift term. These relations are given as

$$\frac{n_{b1}}{n_{b0}} = \frac{e\phi k_{nb} k_y}{m \bar{\omega}_b} = \frac{e\phi}{T_e} \frac{\omega^*}{\omega - \omega_E - k_z v_{beam}}, \quad (3.32)$$

$$\frac{n_{e1}}{n_{e0}} = \frac{e\phi}{T_e} \frac{\omega^*}{\omega - \omega_E}, \quad (3.33)$$

$$\frac{n_{i1}}{n_{i0}} = \frac{e\phi}{T_e} \frac{c_s^2 k_y^2}{(\omega - \omega_{Ei})^2 - \Omega_i^2}, \quad (3.34)$$

where  $v_{beam}$  is the beam velocity,  $\omega_b^* = \omega^*$  and  $\omega_{Eb} = \omega_E$ .

## Plasma Approximation

For quasineutral perturbations, we take  $n_{e1} + n_{b1} = n_{i1}$ , and we get

$$\frac{1}{k_y^2 \lambda_D^2} \left[ (1-a) \frac{\omega^*}{\omega - \omega_E} + a \frac{\omega^*}{\omega - \omega_E - k_z v_{beam}} \right] = \frac{\omega_{pi}^2}{(\omega - \omega_{Ei})^2 - \Omega_i^2}, \quad (3.35)$$

where  $\lambda_D = \sqrt{T_e/4\pi n_{e0} e^2}$  is the electron Debye length and  $a = n_{b0}/n_{i0}$ . When  $a \ll 1$ , neglecting the beam term<sup>1</sup>, we obtain,

$$\frac{1}{k_y^2 \lambda_D^2} \frac{v_{ed} k_y}{\omega - \omega_E} = \frac{\omega_{pi}^2}{(\omega - \omega_{Ei})^2 - \Omega_i^2}. \quad (3.36)$$

Applying eq. (3.36) to cylindrical geometry with weakly magnetized ions ( $\Omega_{ci} \ll \omega$ ) as

$$\frac{1}{k_\theta^2 \lambda_D^2} \frac{\omega^*}{\omega - \omega_E} = \frac{\omega_{pi}^2}{(\omega - \omega_{\theta i})^2}, \quad (3.37)$$

where  $\omega^* = v_{ed} k_\theta$  and  $\omega_E = v_{E \times B e} k_\theta$ . Since ions are weakly magnetized, we replaced  $\omega_{Ei}$  with  $\omega_{\theta i}$ , which is the mean azimuthal ion drift speed. Equation (3.37) is solved to give

$$\omega_R = k_\theta v_{\theta i} + \frac{c_s^2 k_\theta^2}{2\omega^*} \approx k_\theta v_{\theta i}, \quad (3.38)$$

$$\omega_I = \sqrt{c_s^2 k_\theta^2 \frac{(\omega_E - \omega_{\theta i})}{\omega^*} - \frac{c_s^4 k_\theta^4}{4\omega^{*2}}} \approx \sqrt{\frac{c_s^2 k_\theta^2 (\omega_E - \omega_{\theta i})}{\omega^*}}. \quad (3.39)$$

<sup>1</sup>As far as the Simon-Hoh instability mechanism is concerned, i.e., a charge separation in the  $\theta$  direction, the consequent azimuthal electric field  $E_{\theta 1}$  and the enhancement of the density perturbation by the  $E_{\theta 1} \times B_0$  drift, the beam term does not affect the instability.

This shows that when  $v_{\theta i} < E_{r0}/B_0$ , we can have an excitation of a fluid instability. Note that the perpendicular phase velocity is nearly  $v_{\theta i}$  with a small correction due to the second term.

### Poisson's Equation

Now we apply eq. (3.33) and eq. (3.34) to Poisson's equation

$$-\nabla^2\phi = 4\pi e(n_{i1} - n_{e1}), \quad (3.40)$$

where we neglected the beam components. Applying this plane geometry result to the cylindrical geometry we find

$$1 = \frac{\omega_{pi}^2}{(\omega - \omega_{\theta i})^2} - \frac{1}{k_{\theta}^2 \lambda_D^2} \frac{\omega^*}{\omega - \omega_E}, \quad (3.41)$$

where we neglected  $\Omega_i$ . The roots for this dispersion relation are expressed by the Buneman instability type solution, i.e., the growth of the instability occurs as a result of the interaction between the fast (positive energy) wave on the ions and the slow (negative energy) wave on the electrons[4]. In the case of the MSHI, fast and slow ion waves

$$\omega = k_{\theta} v_{\theta i} \pm \omega_{pi}, \quad (3.42)$$

and a slow electron wave

$$\omega = k_{\theta} v_E - \frac{\omega^*}{k_{\theta}^2 \lambda_D^2}, \quad (3.43)$$

interact together. Figure 3.2 shows the real part  $\omega'_R = \omega_R/\Omega_i$  (fig. 3.2(a)) and the imaginary part  $\omega'_I = \omega_I/\Omega_i$  (fig. 3.2(b)) of the instability frequencies of eq. (3.41) as a function of  $k' = k_{\theta} v_E/\Omega_i$ . Since  $k_{\theta}$  is fixed to the  $m = 1$  mode, we consider that variations in  $k'$  are due to variations in  $v_E$  and treat  $\omega^*/k_{\theta}^2 \lambda_D^2$  as a constant.

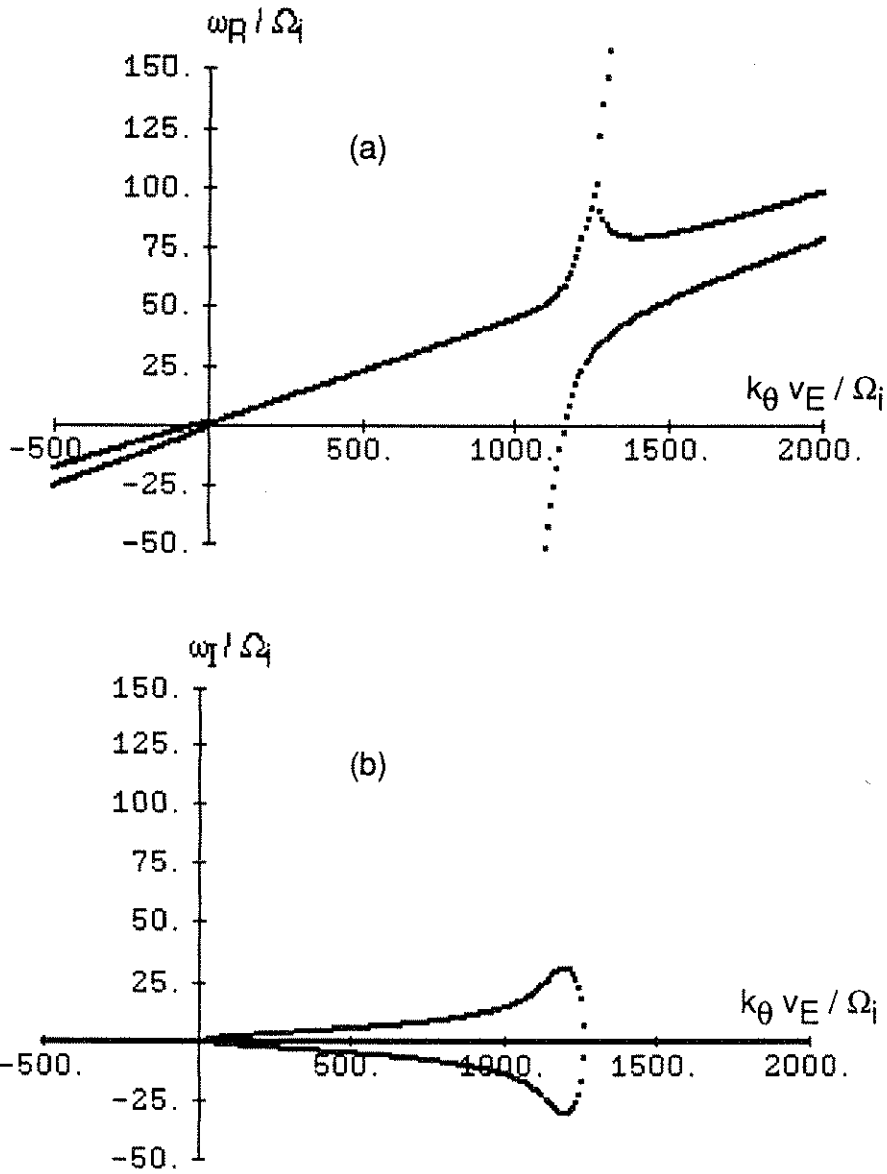


Figure 3.2: Dispersion relation of the MSHI. (a) The real part and (b) the imaginary part of the instability frequencies.

When  $k' \leq 0$  or  $k' \geq 1250$ , there are three real frequency roots which indicate that the plasma is stable. While at  $0 \leq k' \leq 1250$ , we find only one real frequency root and two complex frequency roots, which correspond to a growing wave ( $\omega_I > 0$ ) and a decaying wave ( $\omega_I < 0$ ). In our experiment,  $k' = 166$  and there exists an unstable root. Note that at  $k' < 1100$ ,  $\omega_R$  of the unstable root is expressed exactly as  $\omega_R = k_\theta v_{\theta i}$ , which is the same as the plasma approximation result. Aberration from the  $\omega_R = k_\theta v_{\theta i}$  occurs when  $\omega^*/k_\theta^2 \lambda_D^2 \leq k_\theta v_E$ , or  $k_\theta^2 \lambda_D^2 > 1$ . This is the same condition as the case when the plasma approximation is not valid. In our experimental conditions, since  $\omega^*/k_\theta^2 \lambda_D^2 > k_\theta v_E$  is always satisfied, the plasma approximation gives correct results. Note that in the case  $k_\theta v_{\theta i} = 0$ , the maximum growth of the unstable root occurs when  $\omega \simeq k_\theta v_E \simeq \omega_{pi}$ . This root corresponds to the flute-like drift instability[11, 15, 17].

### 3.5 Kinetic Theory of MSHI

Now we consider kinetic effects on ions. Note that in the actual experiment, ions have large perpendicular excursions in the electrostatic well created by the magnetized radially localized electrons. The ion density response must therefore be obtained from an appropriate Vlasov equation. The unperturbed ion distribution  $f_{i0}$  is a function of the constants of motion, i.e. the perpendicular and parallel energies  $W_\perp = (M/2)(\dot{r}^2 + r^2\dot{\theta}^2 + e\Phi(r))$ ,  $W_\parallel = (M/2)\dot{z}^2$  and the  $\theta$  - canonical momentum  $P_\theta = Mr^2(\dot{\theta} + \Omega_i/2)$  where  $\Omega_i = eB_0/M$  is the ion cyclotron frequency. Since the ion density is nearly uniform in space,  $f_{i0}$  may be chosen as a function of  $W_\perp$  and  $W_\parallel$  only. The perturbed Vlasov equation may now be solved in principle

by following the characteristics:

$$f_{i1} = - \int_{\infty}^t \frac{e}{M} E_1(r'(t'), t') \frac{\partial f_{i0}}{\partial v'} dt' \quad (3.44)$$

and the density perturbation obtained by the equation  $n_{i1} = \int f_{i1} d^3v$ . The exact eigenmode problem is quite complex because of the complicated zeroth order ion orbits (determined by  $\Phi(r)$  and  $B_0$ ) and the radially non-local response of ions which leads to integrodifferential operators. Considerable insight into the new physical effects introduced by large orbit excursions may however be obtained from an approximate kinetic theory which uses harmonic orbit approximations (exact for a parabolic potential well) and an appropriately averaged local radial response for the ions.

The unperturbed trajectory of ions is determined from a solution of the equations

$$\frac{d\vec{r}}{dt} = \vec{v} \quad (3.45)$$

$$\frac{d\vec{v}}{dt} = \Omega_i(\vec{v} \times \hat{z}) + \frac{eE_0}{M} \hat{r}. \quad (3.46)$$

When  $B_0$  is large and ions are magnetized, the second term in the right hand side of eq. (3.46) represents the  $E \times B$  drift term. On the other hand, when  $B_0$  is small and ion orbits are mainly decided by the  $E_0$  term, and by assuming a parabolic potential well,

$$\Phi = \Phi_0 \left(1 - \frac{r^2}{r_0^2}\right) \quad (3.47)$$

eq. (3.46) is reduced to

$$\frac{d\vec{v}}{dt} = \Omega_i(\vec{v} \times \hat{z}) + \Omega_R^2 \vec{r} \quad (3.48)$$

where  $\Omega_R = \sqrt{2e\Phi_0/Mr_0^2}$  is the ion rattle frequency in the parabolic electrostatic well created by the electrons. In the case when  $\Omega_R \gg \Omega_i$  is satisfied, ions are

trapped in  $\Phi$  and ‘magnetized’ due to rattling in this potential well. In this situation,  $\Omega_R$  takes the role of the cyclotron frequency,  $\Omega_i$ , and  $\Omega_i r \hat{\theta}$  the role of the  $E \times B$  drift [23].

In the following section, we show the dispersion relations for two cases; (a) ion cyclotron oscillation and  $E \times B$  drift and (b) ion rattle oscillation and  $\Omega_i r$  drift.

### 3.5.1 Ion Cyclotron Oscillation ( $\Omega_i$ ) and Ion $E \times B$ Drift

Solving eq. (3.44) for  $T_{i\perp} \neq T_{i\parallel}$ ,  $\chi_i$  is given by[24]

$$\chi_i = \frac{1}{k^2 \lambda_{Di}^2} \left\{ 1 + \sum_n \left[ 1 + \frac{T_{i\parallel}}{T_{i\perp}} \frac{n\Omega_i}{\bar{\omega} - n\Omega_i} \right] [W(z_n) - 1] I_n(b) e^{-b} \right\}, \quad (3.49)$$

where  $z_n = \frac{\bar{\omega} - n\Omega_i}{k_z T_{i\parallel} / M}$ ,  $\lambda_{Di} = \sqrt{T_{i\parallel} / 4\pi n_i e^2}$ ,  $b = k_\theta^2 a^2$ ,  $a = \frac{1}{\Omega_i} \sqrt{T_{i\perp} / M}$  is the finite Larmor radius (FLR) term,  $W$  is the plasma dispersion function and  $\bar{\omega} = \omega - k_\theta \langle v_{\theta i} \rangle$  where  $\langle v_{\theta i} \rangle$  is the average ion  $E \times B$  drift. In the case when  $k_z \approx 0$ ,  $z_n \ll 1$  and  $b \gg 1$  are satisfied, eq. (3.49) is reduced to

$$\chi_i = \frac{\omega_{pi}^2}{\bar{\omega}^2} \quad (3.50)$$

Using the plasma approximation  $\chi_i = \chi_e$ , where  $\chi_e$  is given by the fluid calculation, we get the dispersion relation

$$\frac{1}{k_\theta^2 \lambda_D^2} \frac{\omega^*}{\omega - \omega_E} = \frac{\omega_{pi}^2}{\bar{\omega}^2}. \quad (3.51)$$

Equation (3.51) is identical to the fluid calculation result as shown in eq. (3.37).

### 3.5.2 Ion Rattle Oscillation ( $\Omega_R$ ) and $\Omega_i r$ Drift

When  $\Omega_R$  replaces  $\Omega_i$  and  $\Omega_i r$  drift replaces the  $E \times B$  drift, eq. (3.49) becomes

$$\chi_i = \frac{1}{k^2 \lambda_{Di}^2} \left\{ 1 + \sum_n \left[ 1 + \frac{T_{i\parallel}}{T_{i\perp}} \frac{n\Omega_R}{\bar{\omega} - n\Omega_R} \right] [W(z'_n) - 1] I_n(b') e^{-b'} \right\} \quad (3.52)$$

where  $\Omega_R = \sqrt{2e\Phi_0/Mr_0^2}$  is the ion rattle frequency,  $\lambda_{Di} = \sqrt{T_{i\parallel}/4\pi n_i e^2}$ ,  $z'_n = \frac{\bar{\omega} - n\Omega_R}{k_z T_{i\parallel}/M}$ ,  $b' = k_\theta^2 a'^2$ ,  $a' = \frac{1}{\Omega_R} \sqrt{T_{i\perp}/M}$  is the 'effective FLR' term and  $\bar{\omega} = \omega - k_\theta \langle v_{\theta i} \rangle$  where  $\langle v_{\theta i} \rangle = \Omega_i \langle \Omega_R^2 (r - r_m) \rangle / \langle \Omega_R^2 \rangle$  is the mean fluid ion drift obtained by an appropriate average over the width of the radial eigenstructure around  $r_m$  and over the ion distribution function [23].

(a) For  $k_z \approx 0$ ,  $z'_n \ll 1$  and  $b' \gg 1$  (i.e., when ion trapping in the radial well is ignored), eq. (3.52) reduces to eq. (3.50). Therefore, the dispersion relation is identical to eq. (3.51) or the fluid calculation result shown in eq. (3.37).

(b) For  $k_z \approx 0$  and  $b' < 1$ , which is more appropriate for the experiment, we get the new dispersion relation

$$\frac{1}{k_\theta^2 \lambda_D^2} \frac{\omega^*}{\omega - \omega_E} = \frac{\omega_{pi}^2}{\bar{\omega}(\bar{\omega} + i\nu) - \Omega_R^2}. \quad (3.53)$$

We have introduced a phenomenological damping term  $\nu$  to account for the Landau type phase mixing which arises for perpendicularly propagating modes when  $\Omega_R = \Omega_R(W_\perp)$ ; i.e., when the electrostatic well is non-parabolic. Equation (3.53) may be solved to give the results:

$$\begin{aligned} \omega &= k_\theta \langle v_{\theta i} \rangle + \frac{c_s^2 k_\theta^2}{2\omega^*} \\ &+ i \left[ -\frac{\nu}{2} + \sqrt{\frac{c_s^2 k_\theta^2}{M\omega^*} (\omega_E - k_\theta \langle v_{\theta i} \rangle) - \Omega_R^2 + \frac{1}{4} (\nu + i \frac{c_s^2 k_\theta^2}{\omega^*})^2} \right]. \end{aligned} \quad (3.54)$$

The most important effect of the ion-rattle in the electrostatic well is the stabilization entering through the  $\Omega_R$  term in the square-root. The Landau effect does not stabilize the mode as may be verified by taking the large  $\nu$  limit; this is understandable because the Simon-Hoh instability is known to preserve the instability in the presence of large ion dissipation [19, 20]. From eq. (3.54) since  $\Omega_R^2$  is smaller



than  $\frac{c_s^2 k_\theta^2}{M\omega^*}(\omega_E - k_\theta < v_{\theta i} >)$  term, we note that the modified Simon-Hoh mode is unstable for the beam plasma experiment. The perpendicular phase velocity is  $< v_{\theta i} > + c_s^2 k_\theta^2 / 2\omega^*$ . Unfortunately,  $< v_\theta >$  can only be accurately obtained from a detailed non-local eigenmode analysis.

## 3.6 Comparison with Other Instabilities

### 3.6.1 Modified Two-stream Instability (MTSI) and Flute-like Drift Instability (FDI)

A dispersion relation for the intermediate frequency ( $\omega_{ci} \ll \omega \ll \omega_{ce}$ ) electrostatic instabilities driven by relative electron-ion drift across an external axial magnetic field[11, 12, 15, 16, 17] is expressed as,

$$1 + \chi_e + \chi_i = 0, \quad (3.55)$$

$$\chi_e = \frac{\omega_{pe}^2 k_\perp^2}{\omega_{ce}^2 k^2} - \frac{\omega_{pe}^2 k_z^2}{(\omega - kv_{0e})^2 k^2} + \frac{\omega_{pe}^2 k_n k_\perp}{\omega_{ce}(\omega - kv_{0e}) k^2}, \quad (3.56)$$

$$\chi_i = -\frac{\omega_{pi}^2}{(\omega - kv_{0i})^2}, \quad (3.57)$$

where  $k_n = |n'_0/n_0|$ . When the density gradient term (the third term) is dominant over the  $k_z$  term (the second term) in  $\chi_e$ , a dispersion relation for the flute-like drift instability (FDI)[11, 15, 17] is derived. Equation (3.55) is reduced to the modified two-stream instability (MTSI)[12, 15, 16] when the condition is reversed. The instability that we have observed is  $k_z \approx 0, k_n \neq 0$  mode. Therefore, it is similar to the FDI. For the experimental condition of  $\omega_{pe}^2 \ll \omega_{ce}^2, k_z = 0$ , eq. (3.56) is

reduced to

$$\chi_e = \frac{\omega_{pe}^2 \frac{k_n}{k}}{\omega_{ce}(\omega - kv_{0e})} = \frac{1}{k^2 \lambda_{De}^2} \frac{\omega^*}{\omega - kv_{0e}}, \quad (3.58)$$

which is the modified Boltzmann relation for  $k_z = 0$ . The dispersion relation eq. (3.55) is reduced to

$$1 + \frac{1}{k^2 \lambda_{De}^2} \frac{\omega^*}{\omega - kv_{0e}} - \frac{\omega_{pi}^2}{(\omega - kv_{0i})^2} = 0, \quad (3.59)$$

We rewrite eq. (3.59) as

$$(\omega - kv_{0e})[(\omega - kv_{0i})^2 - \omega_{pi}^2] = -\frac{1}{k^2 \lambda_{De}^2} \omega^* (\omega - kv_{0i})^2. \quad (3.60)$$

When (a)  $kv_{0e} \approx \omega_{pi}$ ,  $\omega \approx \omega_{pi}$  and  $kv_{0i} = 0$ , are satisfied, the FDI has the maximum growth rate. The maximum growth rate  $\gamma_{max}$  is calculated from eq. (3.60) by assuming  $\omega = \omega_{pi} + i\gamma$  ( $\gamma/\omega_{pi} \ll 1$ ),

$$\begin{aligned} (i\gamma)(i\gamma)(2\omega_{pi}) &= -\frac{1}{k^2 \lambda_{De}^2} \omega^* \omega_{pi}^2 \\ \gamma_{max}^2 &= \frac{\omega^* \omega_{pi}^2}{2k^2 \lambda_{De}^2}. \end{aligned} \quad (3.61)$$

The FDI is understood as an instability caused by a coupling between an electron  $E \times B$  drift wave in a nonuniform plasma and an ion plasma oscillation. No instabilities are found for the conditions (b)  $\omega \approx kv_{0e}$ ,  $\omega \ll \omega_{pi}$  and  $kv_{0i} = 0$ , (c)  $\omega \ll kv_{0e}$ ,  $\omega \approx \omega_{pi}$  and  $kv_{0i} = 0$ . The modified Simon-Hoh instability (MSHI) is a new unstable flute mode for (d)  $\omega \approx kv_{0i} \ll \omega_{pi}$ ,  $kv_{0e}$ . A growth rate of the MSHI is calculated from eq. (3.60) by assuming  $\omega = kv_{0i} + i\gamma$  ( $\gamma/kv_{0i} \ll 1$ ),

$$\begin{aligned} (-kv_{0e})(-\omega_{pi}^2) &= -\frac{1}{k^2 \lambda_{De}^2} \omega^* (i\gamma)^2 \\ \gamma^2 &= \frac{kv_{0e} \omega_{pi}^2 k^2 \lambda_{De}^2}{\omega^*} = \frac{\omega_E k^2 c_s^2}{\omega^*}. \end{aligned} \quad (3.62)$$

This growth rate is exactly the same as the  $\omega_I$  shown in eq. (3.39). Many authors[11, 12, 15, 16, 17] considered only a relative electron-ion drift  $v_0$  in their theory. However, none of them considered  $v_{0i}$  and  $v_{0e}$  separately, which is necessary to get the proper  $\omega_R$  of the MSHI. Unlike the FDI, the MSHI is unstable even when the plasma approximation ( $k^2 \lambda_{De}^2 \ll 1$ ) is satisfied, and both the real and the imaginary part of  $\omega$  are independent of plasma density.

### 3.6.2 Anti-drift Mode

The anti-drift instability[18] is an intermediate frequency ( $\omega_{ci} \ll \omega \ll \omega_{ce}$ ) electrostatic instability in a weakly ionized inhomogeneous plasma with cold ( $T_i = 0$ ) unmagnetized ions. Here we consider three cases as follows:

(a) When  $k_z = 0$  and  $E_{r0} = 0$ , we get

$$\frac{n_{e1}}{n_{e0}} = \frac{e\phi \omega^*}{T_e \omega} \quad (3.63)$$

$$\frac{n_{i1}}{n_{i0}} = \frac{e\phi k_{\perp}^2 c_s^2}{T_e \omega^2}. \quad (3.64)$$

In this case, we find a stable mode with a frequency  $\omega_R = c_s^2 k^2 / \omega^*$ . Since  $\omega^*$  is in the denominator, this mode is called the anti-drift mode. Note that this  $\omega_R$  is the same as the second term of the real frequency of the MSHI (different by a factor of 2).

There are two possible instability mechanisms to make the anti-drift mode unstable. One is collisions between electrons and the neutral gas, and the other is relative slippage between electrons and ions caused by the DC electric field.

(b) When  $k_z \neq 0$ ,  $E_{r0} = 0$  and electron-neutral collisions are important, we

get

$$\frac{n_{e1}}{n_{e0}} = \frac{\epsilon\phi\omega^* + ik_z^2 c_e^2/\nu_{en}}{T_e \omega + ik_z^2 c_e^2/\nu_{en}} \quad (3.65)$$

where  $c_e = \sqrt{T_e/m}$  and  $n_{i1}/n_{i0}$  is the same as eq. (3.64). This instability is called the anti-drift instability (ADI), which Fridman predicted in his paper. When  $\omega < \omega^* \ll k_z^2 c_e^2/\nu_{en}$ , the ADI is reduced to an ion-sound instability,  $\omega \approx c_s k_\perp (1 + i\omega^* \nu_{en}/2k_z^2 c_e^2)$  [22].

(c) When  $E_{r0} \neq 0$ ,  $k_z = 0$  and the ion azimuthal drift is neglected, we also get an unstable solution which is the same as the MSHI case with  $k_\theta v_{\theta i} = 0$ , i.e.,

$$\begin{aligned} \omega_R &= c_s^2 k^2 / 2\omega^* \\ \omega_I &= \sqrt{c_s^2 k_\theta^2 \frac{\omega_E - \omega_{\theta i}}{\omega^*} - \frac{c_s^4 k_\theta^4}{\omega^{*2}}} \approx \sqrt{\frac{c_s^2 k_\theta^2 (\omega_E - \omega_{\theta i})}{\omega^*}}. \end{aligned} \quad (3.66)$$

In the case of the MSHI, since  $k_\theta v_{\theta i} \gg c_s^2 k^2 / 2\omega^*$  is satisfied, the instability frequency  $\omega_R$  shows a completely different dependence on the plasma parameters compared to the ADI, even though  $\omega_i$  is the same. Therefore, the MSHI is classified as the ADI with  $E_{r0}$  and  $v_{Ee} \gg v_{\theta i} \neq 0$ .

# Chapter 4

## Verification of the MSHI

### 4.1 Introduction

We believe that the MSHI is a candidate for the  $M_1$  mode. As shown in Chapter 3, the MSHI is unstable when  $v_E > v_{\theta i}$ , and the real part of the instability frequency is  $\omega_R \approx k_\theta v_{\theta i}$ . From the results of the  $\Phi$  measurement,  $v_E$  is a factor of twenty larger than  $\omega_1/k_\theta$ , and as will be seen shortly, the  $v_{\theta i}$  measurement shows  $v_{\theta i} \approx \omega_1/k_\theta$ . Thus, the experimental results are consistent with the MSHI theory. In this section, first we show results of the  $v_{\theta i}$  measurement. Section 4.3 describes results of a simple calculation of an ion orbit under measured plasma potential profiles and explain how the ion azimuthal drift velocity  $v_{\theta i} \approx v_E/20$  is obtained. In section 4.4, an interpretation of the  $T_{i\perp}$  measurement results and the ion mass dependence of  $f_1$  is given. Section 4.5 describes a simple expression for the  $v_{\theta i}$ , and its comparison with the measured drift velocity and the instability phase velocity. In section 4.6, we show experimental verification of the  $v_{\theta i}$  equation

given in section 4.5.

## 4.2 $v_{\theta i}$ Measurement

The ion azimuthal drift velocity  $v_{\theta i}$  is measured by the one-sided probe technique. A probe is shielded on one side and biased to collect the ion saturation current. When the probe is faced away from the ion rotation direction, only the ion saturation current,  $I_{is} = en_i A c_s$ , is collected. When the probe is faced to the rotation direction, both  $I_{is}$  and the current caused by ion drift,  $I_{i\theta} = en_i A v_{\theta i}$ , are collected. The difference in current  $\Delta I$  is equal to  $I_{i\theta}$  and related to  $v_{\theta i}$  by  $v_{\theta i} = \Delta I c_s / I_{is}$ .

Figure 4.1 shows the measured  $f_1$  and the ion rotation frequency  $f_{\theta i}$ . We calculate  $f_{\theta i}$  by  $f_{\theta i} = v_{\theta i} k_{\theta} / 2\pi$ , where  $k_{\theta} = 1/r_1 = 2 \text{ cm}^{-1}$  and  $r_1 = 0.5 \text{ cm}$  is the radius at which  $M_1$  amplitude is maximum. We see that  $f_{\theta i}$  shows the same trend as  $f_1$  and agrees within a factor of two for the  $I_p$  (fig. 4.1(a)), P (fig. 4.1(b)) and B (fig. 4.1(c)) scan cases. In fig. 4.1,  $f_{Ei}$  is the calculated ion azimuthal drift frequency. We discuss  $f_{Ei}$  in section 4.5.

## 4.3 Orbit Calculation

In order to explain a factor of twenty smaller  $v_{\theta i}$  than  $v_E$ , we calculate an ion orbit and velocity using the measured DC plasma potential profiles shown in fig. 2.7(a). Figure 4.2(a) shows an ion orbit for  $I_p = 100 \mu\text{A}$  assuming that the ion is initially at rest at  $r = 1 \text{ cm}$ . The ion starts to move radially inward due to the  $E_{r0}$  field. At the central part, it is pushed slightly radially outward due to the  $v_{\theta} \times B_0$

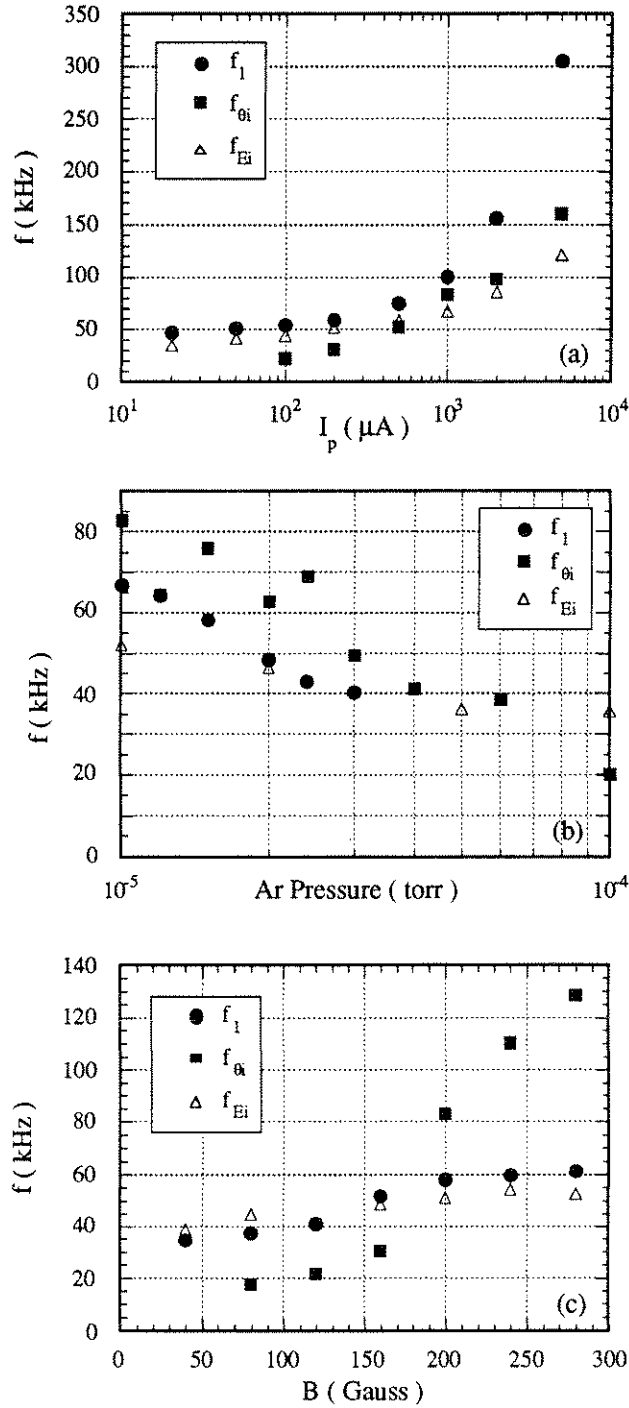


Figure 4.1: (a)  $I_p$ , (b)  $P$ , and (c)  $B$  dependence of  $f_1$ ,  $f_{\theta i}$ , and  $f_{Ei}$ . Here,  $f_{\theta i}$  is the measured ion rotation frequency by the one-sided probe and expressed as  $f_{\theta i} = v_{\theta i} k_{\theta} / 2\pi$ , where  $k_{\theta} = 1/r_1 = 2 \text{ cm}^{-1}$  and  $r_1 = 0.5 \text{ cm}$  is the radius at which  $M_1$  amplitude is maximum. And  $f_{Ei}$  is the calculated ion azimuthal drift frequency from eq. (4.9).

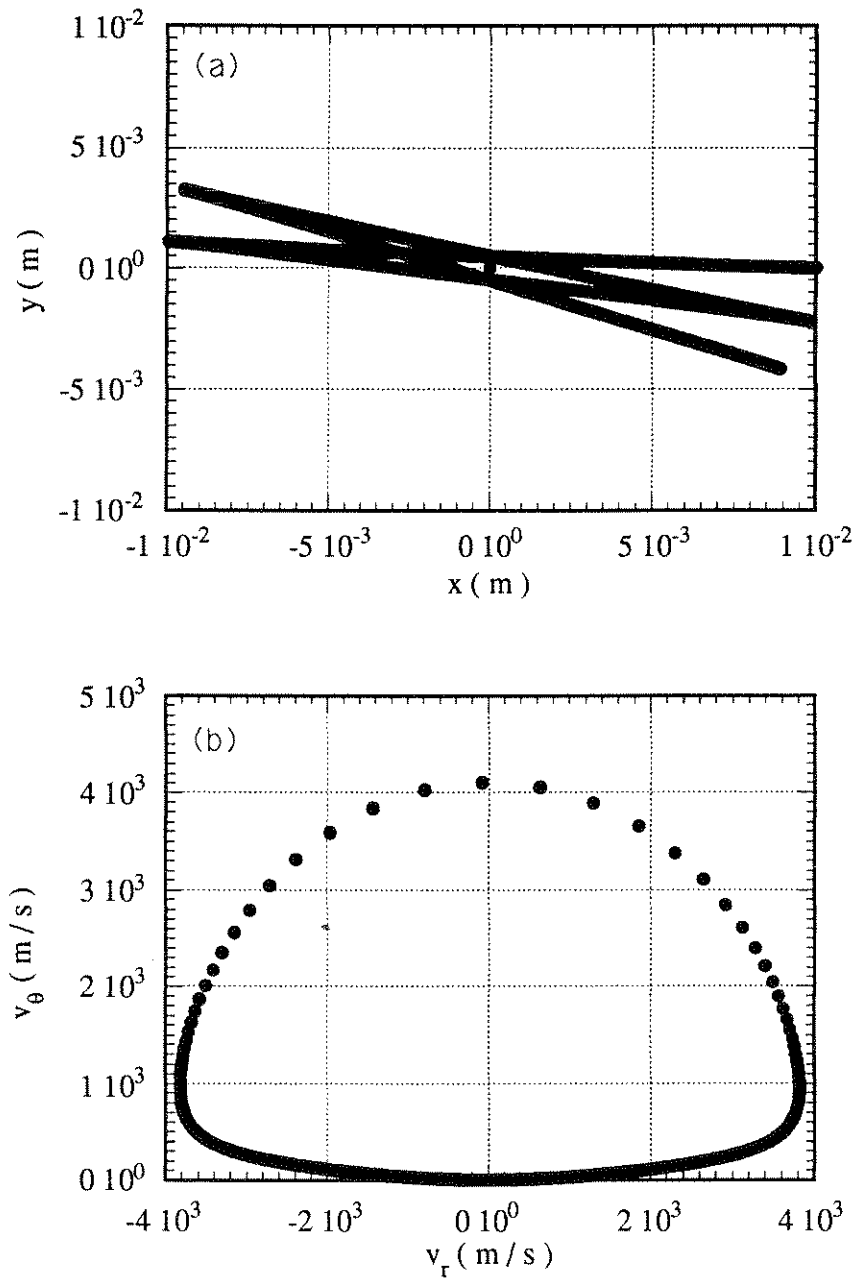


Figure 4.2: (a) A calculated ion orbit and (b)  $v_\theta$  versus  $v_r$  for the measured DC plasma potential for  $I_p = 100 \mu\text{A}$ . The ion is assumed to be initially at rest ( $v_r = v_\theta = 0$ ) at  $r = 1$  cm.



force. After passing the center, the ion is decelerated and stops at the same radial position as the initial position.

Figure 4.2(b) shows  $v_\theta$  versus  $v_r$ . At  $t = 0$ ,  $v_r = v_\theta = 0$  and the ion starts to gain negative  $v_r$  and begins to rotate in the clock-wise direction. The ion velocity  $v$  is governed by the conservation of energy, i.e.,

$$\frac{Mv_\theta^2}{2} + \frac{Mv_r^2}{2} = e\Delta\Phi, \quad (4.1)$$

where  $\Delta\Phi$  is the DC plasma potential difference. For most of the time,  $v_r$  is dominant over  $v_\theta$  because of the nearly straight line orbit. However, when an ion comes closest to the center,  $v_r$  becomes zero and  $v_\theta$  gets the maximum velocity,  $v_{\theta max}$ . At this point, eq. (4.1) is reduced to

$$\frac{Mv_{\theta max}^2}{2} = e\Delta\Phi. \quad (4.2)$$

It is this  $v_\theta$  that decides the phase velocity of the azimuthally propagating mode ( $M_1$ ).

An initial position dependence of  $v_{\theta max}$  is plotted in fig. 4.3(a) for the same potential profile as the fig. 4.2 case. We find that  $v_{\theta max}$  saturates at  $r > 2$  cm, which is only a factor of three larger than  $\omega_1/k_\theta$ . The averaged fluid velocity of ions,  $\langle v_{\theta i} \rangle$  seems to show a good agreement with  $\omega_1/k_\theta$ . Figure 4.3(b) shows a variation of  $v_{\theta max}$  for the measured  $\Phi$  profiles shown in fig. 2.7(a). The measured instability phase velocity  $\omega_1/k_\theta$  is also shown in the figure. The initial position of ions is fixed at  $r = 1.5$  cm in the orbit calculation. We see that  $v_{\theta max}$  and  $\omega_1/k_\theta$  show a similar dependence on  $I_p$  and differ by a factor of three.

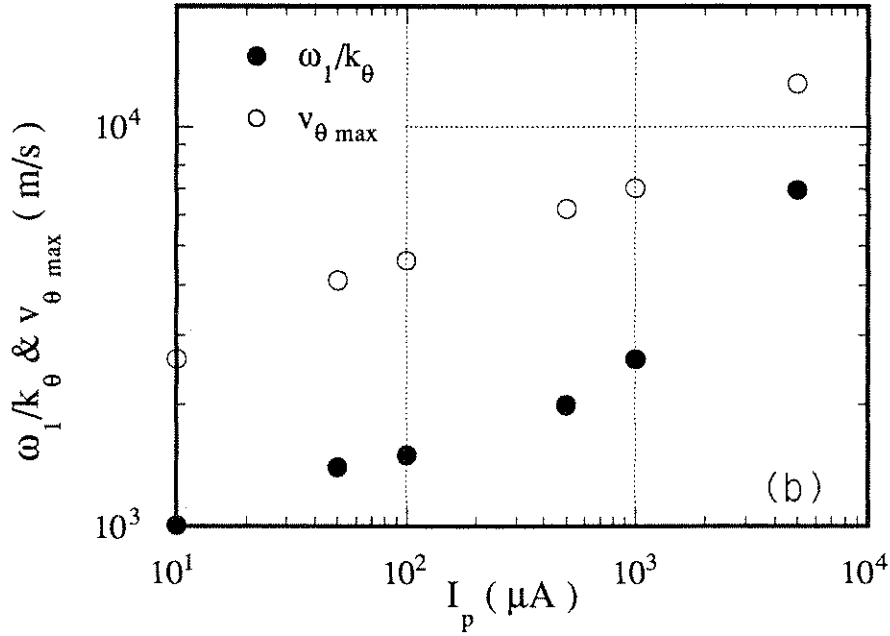
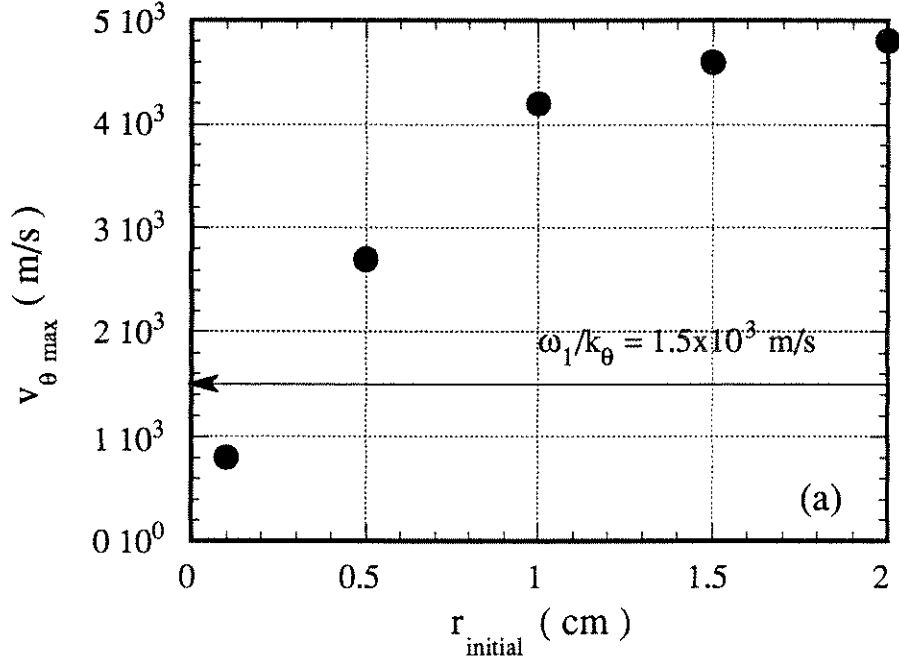


Figure 4.3: (a) An initial position dependence of  $v_{\theta \text{ max}}$  for the same potential profile as the fig. 4.2 case. Note that  $v_{\theta \text{ max}}$  saturates at  $r > 2$  cm, which is only a factor of three larger than  $\omega_1/k_\theta$ . The averaged fluid velocity of ions,  $\langle v_{\theta i} \rangle$  seems to show a good agreement with  $\omega_1/k_\theta$ . (b) Variation of  $v_{\theta \text{ max}}$  for the measured  $\Phi$  profile at each  $I_p$  and the measured  $\omega_1/k_\theta$ . The initial position of ions is fixed at  $r = 1.5$  cm in the orbit calculation.

## 4.4 Ion Mass Dependence of $f_1$ and $T_{i\perp}$ Measurement

A clear  $M^{-0.5}$  dependence of  $f_1$  is shown in fig. 2.15(b). We explain the reason for this and discuss the ion perpendicular temperature ( $T_{i\perp}$ ) measurement results. As mentioned above, the ion motion is governed by the DC potential profile and is approximated by a straight line. The azimuthal ion velocity,  $v_{\theta i}$ , is expressed by

$$\frac{M v_{\theta i}^2}{2} \approx e \Delta \Phi. \quad (4.3)$$

Therefore, the instability frequency is expected to have an ion mass dependence as

$$\omega_1 \approx k_{\theta} \langle v_{\theta i} \rangle \propto \sqrt{\frac{2e\Delta\Phi}{M}} \propto M^{-0.5}. \quad (4.4)$$

As shown in fig. 2.9(a), a good agreement between  $T_{i\perp}$  and  $\Delta\Phi$  indicate a relation of the form

$$\frac{M v_{\theta i}^2}{2} \approx e \Delta \Phi \approx \kappa T_{i\perp}. \quad (4.5)$$

Equation (4.5) suggests that  $T_{i\perp}$  corresponds to the ion perpendicular energy spread.

The radial position dependence of  $T_{i\perp}$  is shown in fig. 2.10. The reason why the ion kinetic energy or  $T_{i\perp}$  is the largest as we approach the center is simply that the ions “rattling” in the potential well sample the largest potential difference there. At larger radii or away from the axis of symmetry the ions give some of their kinetic energy back to the potential well and therefore are left with a smaller  $T_{i\perp}$ .

## 4.5 Finite Ion Larmor Radius Correction of Ion $E \times B$ Drift

Under a plane DC electric field,  $E_0 \propto e^{-k_\perp x}$ , an averaged ion  $E \times B$  drift velocity over the ion gyro-cycle and the Maxwellian distribution in  $v_\perp$  is expressed as

$$v_{Ei} = \frac{E_{r0}}{B_0} e^{-b} I_0(b), \quad (4.6)$$

where  $I_0$  is the modified Bessel function of the first kind and  $b = k_\perp^2 r_{Li}^2 / 2 = k_\perp^2 \kappa T_{i\perp} M / (eB_0)^2$  [22]. Now we want to show that eq. (4.6) is a good approximation for the phase velocity of MSHI or  $v_{\theta i}$  in our cylindrical plasma. We replace  $x$  with  $r$  and  $k_\perp$  with  $1/r_0$ , where  $r_0$  is a typical scale-length of  $E_{r0}$  or the plasma, and take  $r_0 = 1.0$  cm. When  $b = r_{Li}^2 / 2r_0^2 \ll 1$ ,  $v_{Ei}$  is approximated as

$$v_{Ei} \approx \frac{E_{r0}(1-b)}{B_0}. \quad (4.7)$$

This is the  $E \times B$  velocity with a small finite Larmor radius (FLR) correction term. When  $b > 1$ ,  $v_{Ei}$  is expressed as

$$v_{Ei} \approx \frac{E_{r0}}{B\sqrt{2\pi b}} = \frac{r_0 e E_{r0}}{\sqrt{2\pi \kappa T_{i\perp} M}}. \quad (4.8)$$

We approximate  $E_{r0}$  and  $T_{i\perp}$  as  $|E_{r0}| = |-\nabla\Phi_0| = k\Phi_0 \approx \Phi_0/r_0$  and  $\kappa T_{i\perp} \approx e\Delta\Phi_0$ . Finally, for the  $b > 1$  case, we get

$$v_{Ei} \approx \frac{1}{2\sqrt{\pi}} \sqrt{\frac{2e\Phi_0}{M}}. \quad (4.9)$$

This velocity is to be interpreted as the ion velocity obtained from the DC plasma potential.

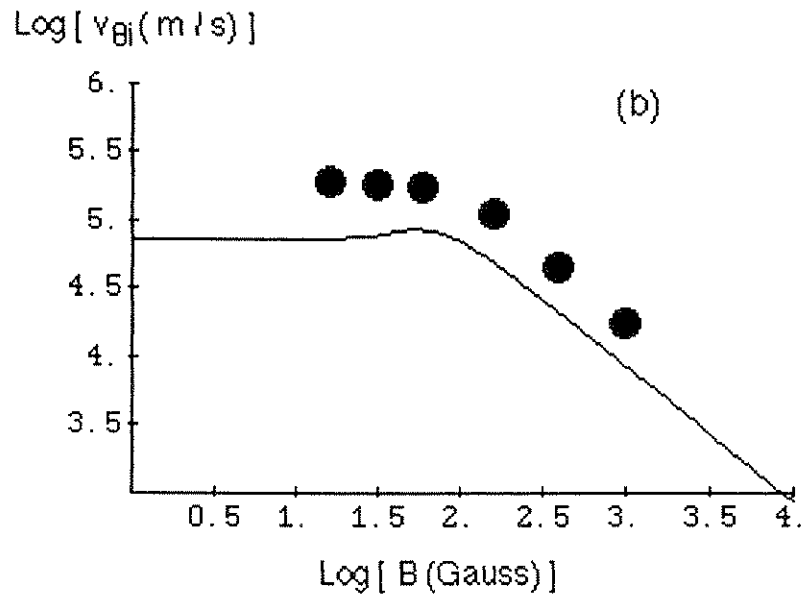
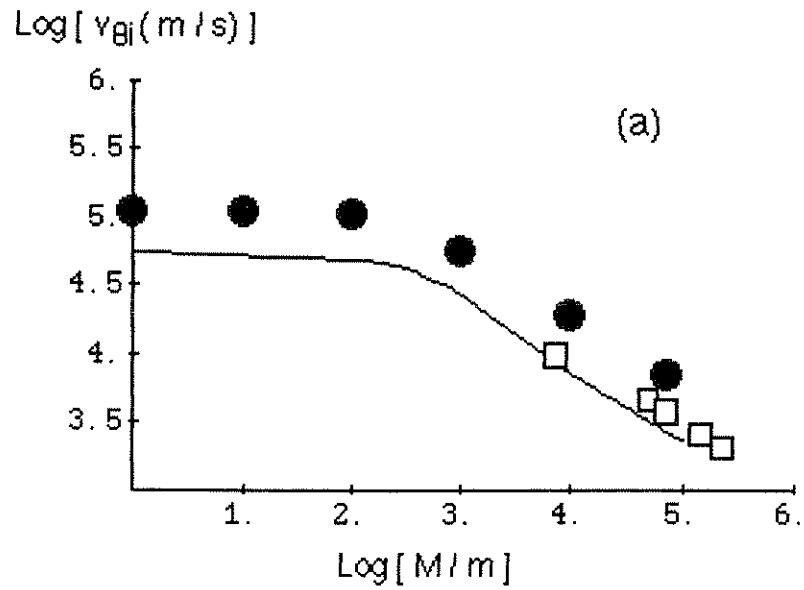


Figure 4.4: (a) Ion to electron mass ratio  $M/m$  dependence of the effective ion  $E \times B$  drift velocity  $v_{Ei}$  calculated from eq. (4.6) (solid line),  $v_{\theta max}$  obtained from the ion orbit calculation (solid circle), and the measured instability phase velocity  $v_1 = \omega_1/k_\theta$  (open square). (b) B dependence of  $v_{Ei}$  (solid line) and calculated  $v_{\theta max}$  (solid circle) for  $M/m = 100$ .

Equation (4.6) is shown in fig. 4.4(a) with a solid line as a function of ion to electron mass ratio,  $M/m$ . At  $M/m < 400$ ,  $v_{Ei}$  corresponds to the  $E \times B$  velocity with a small FLR correction term (eq. (4.7)), and has very weak mass dependence. At  $M/m > 400$ ,  $v_{Ei}$  is given by eq. (4.9) and it shows a  $1/\sqrt{M}$  dependence. The solid circle in fig. 4.4(a) shows  $v_{\theta max}$ , obtained from a simple ion orbit calculation shown in the previous section. In the figure, measured instability phase velocities,  $v_1 = \omega_1/k_\theta$ , are also shown (open square). These three quantities,  $v_{Ei}$ ,  $v_{\theta max}$  and  $v_1$ , agree well each other. The effective ion  $E \times B$  drift frequency  $f_{Ei} = v_{Ei}k_\theta/2\pi$  calculated from eq. (4.9) is shown in fig. 4.1. We see that  $f_{Ei}$  agrees particularly well with the measured instability frequency ( $f_1$ ) for the B scan and with the ion azimuthal drift frequency ( $f_{\theta i}$ ) for the  $I_p$  scan case. Furthermore,  $f_1$  shows the same overall trend with  $I_p$ , P and B as  $f_1$  and  $f_{\theta i}$ . Therefore, we conclude that the phase velocity of the  $M_1$  mode is possibly expressed as  $v_{Ei}$ , the effective ion  $E \times B$  drift velocity for the large Larmor radius.

We believe that eq. (4.6) is good for a wide range of  $b$  values, i.e., even for  $M/m < 1837$ , the mass ratio of a hydrogen ion. It is important to understand the  $M/m$  dependence of  $v_{\theta i}$  because later we will show Particles in Cell (PIC) code computer simulation results calculated with scaled mass ratios  $M/m = 100$  to 800. As shown in fig. 4.4(a), for  $B = 160$  G,  $v_{\theta i} \approx E/B$  is the  $E \times B$  drift velocity for mass ratios  $M/m < 400$ . Therefore, there is no velocity difference between the electrons and ions, and we expect to see no MSHI. In order to excite the MSHI, we need to increase the  $b$  value or reduce  $B$  so that  $v_{Ei}$  becomes smaller than  $v_{Ee}$ . Figure 4.4(b) shows  $B$  dependence of  $v_{Ei}$  (in solid line) and calculated  $v_{\theta max}$  (in solid circle) for  $M/m = 100$ . At  $B \geq 100$  G, both  $v_{Ei}$  and  $v_{\theta max}$  show  $1/B$

dependence and they correspond to  $v_{Ei} \approx v_{Ee} = E_{r0}/B$ . In order to excite the MSHI,  $B \leq 100$  G is required to satisfy the condition  $v_{Ee} > v_{Ei} = v_{\theta i} \propto \sqrt{\Delta\Phi/M}$ .

## 4.6 Biased End-plate Experiments

Since the instability frequency is decided by the DC plasma potential,  $\omega_1 \propto \sqrt{\Delta\Phi/M}$ , we have tried to control  $\Delta\Phi$ . The method we have used is to bias the end-plate. Figure 4.5(a) shows the plasma potential at  $r = 0$  cm,  $r = 1$  cm, and the difference between the two quantities,  $\Delta\Phi$ , measured by the emissive probe as a function of the end-plate bias,  $V_{EP}$ . Figure 4.5(b) shows the instability frequency,  $f_1$ , versus  $V_{EP}$ . We find that  $f_1$  is closely related to  $\Delta\Phi$ . The calculated  $f_1$  using the eq. (4.9) is roughly a factor of two smaller than the measured  $f_1$  but has a strikingly similar functional dependence on  $V_{EP}$ .

## 4.7 Summary

The experimental findings can be summarized as follows:

1. The measured ion azimuthal velocity,  $v_{\theta i}$ , is in reasonable agreement with the phase velocity of the  $M_1$  mode,  $v_1 = \omega_1/k_\theta$  as expected for the MSHI.
2. By using the measured plasma potential profile, it is found that the calculated  $v_{\theta max}$  shows good agreement with  $v_1$ . In this calculation, it is assumed that the ions are at rest at the initial position. In the experiments, the ion orbit is approximated by a straight line with a very small aberration due to  $v \times B$  force.

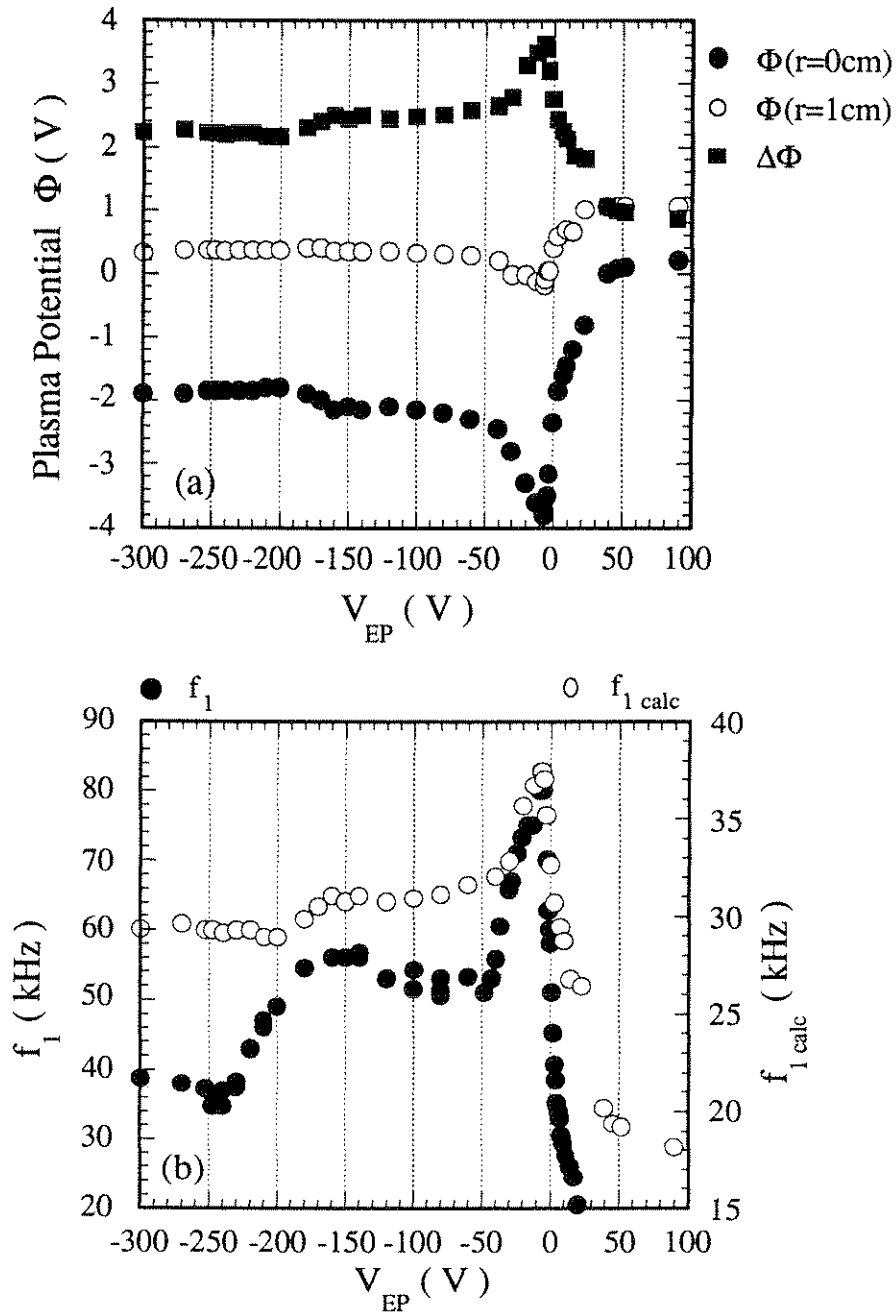


Figure 4.5: (a) The plasma potential at  $r = 0$  cm,  $r = 1$  cm, and the difference between the two quantities,  $\Delta\Phi$ , measured by the emissive probe as a function of the end-plate bias,  $V_{EP}$ . (b) The instability frequency,  $f_1$ , versus  $V_{EP}$ .  $f_1$  is closely related to  $\Delta\Phi$ . The calculated  $f_1$  using the eq. (4.9) is roughly a factor of two smaller than the measured  $f_1$  but has a strikingly similar functional dependence on  $V_{EP}$ .



3. The ion mass dependence of  $f_1$  and the ion perpendicular temperature,  $T_{i\perp}$ , are measured. It can be shown that they are simply expressed as  $e\Delta\Phi \approx \kappa T_{i\perp} \approx Mv_i^2/2$ . These results are expected from the orbit calculation.
4. We have shown that the calculated  $v_{\theta i}$  can simply be approximated by the ion  $E \times B$  velocity,  $v_{Ei}$ , expressed by eq. (4.6), for a wide range of ion mass ratios,  $M/m$ , by assuming  $\kappa T_{i\perp} \approx e\Delta\Phi$ . The measured  $v_1$  also agrees well with eq. (4.6). The electron  $E \times B$  drift velocity is simply expressed as  $v_{Ee} = E_{r0}/B_0$ , because of the small electron Larmor radius. A difference of twenty between the electron  $E \times B$  and the ion azimuthal velocity is easily explained by eq. (4.6).
5. By biasing the end-plate,  $\Delta\Phi$  can be controlled. It was shown that the measured and calculated instability frequencies agree well, when  $\Delta\Phi$  is manipulated in this manner.

# Chapter 5

## Transient Study of the MSHI

### 5.1 Introduction

In our beam-plasma system since the plasma is collisionally ionized by the electron beam, ions are produced only at the 1 cm diameter beam region. In order to maintain the broad steady state density profile, which we have shown in chapter 2, ions have to keep diffusing radially. Note that the DC electric field is radially inward in the direction to retard the ions in the beam region. Ions therefore have to be heated at least on the order of the DC plasma potential ( $\Delta\Phi$ ) to go outside. The perpendicular ion temperature  $T_{i\perp}$  was measured by an energy analyzer. We found that  $T_{i\perp}$  is simply expressed as

$$\kappa T_{i\perp} \approx \frac{M v_i^2}{2} \approx e\Delta\Phi \quad (5.1)$$

where  $\Delta\Phi$  is the DC plasma potential difference in the radial direction. This equation implies that once ions go outside to the high potential position, they fall down the potential well and acquire a kinetic energy which corresponds to  $e\Delta\Phi$ .

In our previous measurements which were steady state, there was no evidence for the radial diffusion of ions. Furthermore, it is not clear how the ions diffuse out.

We described the MSHI theory and calculated the real part ( $\omega_R$ ) and the imaginary part ( $\omega_I$ ) of the instability frequency. We studied  $\omega_R$  in detail for various plasma conditions and showed that the measured  $\omega_R$  agrees well with the theory. However, no measurement was conducted on  $\omega_I$ .

In this chapter we discuss time resolved measurements which follow the evolution of the DC parameters of the plasma and the transient study of the growth phase of the MSHI. We have performed (A) the radial relaxation of the ion and electron density profiles measurement, (B) the instability onset measurement, and (C) the instability growth measurement. In order to study (A) and (B), we have applied a pulsed beam acceleration voltage  $V_B$  and measured the temporal evolution of the electron saturation current  $I_{es}$  and the ion saturation current  $I_{is}$  at various radial positions. After a quick turn-on of  $V_B$ , the plasma ionization process, the ion diffusion process and the growth of the instability process take place. In the instability onset measurement all these processes are included together.

We have used the biased endplate method to study (C). When a positive bias is applied to the endplate, the amplitude of the MSHI is strongly suppressed. When the bias is electrically turned off and the endplate is grounded, the instability starts growing. In this method, since we are varying the plasma potential but are maintaining the steady state ionization process, the growth of the mode is clearly observed.

In the next section we describe the results of (A) the radial relaxation of the ion

and electron density profiles measurement, (B) the instability onset measurement, and (C) the instability growth measurement.

## 5.2 Experiments

### 5.2.1 Ion Diffusion Measurements

For the ion diffusion measurement, we have applied a pulsed  $V_B$ . The rise time of  $V_B$  is less than  $0.4 \mu s$ . A fluctuation, whose oscillation period is  $1.2 \mu s$ , is observed in  $V_B$  early in time ( $t \leq 8 \mu s$ ). The maximum fluctuation level at  $t = 0.4 \mu s$  is  $\Delta V_B/V_B \simeq 0.45$  and decays in time. This might be caused by the capacitive effect of the gun. The rise time of  $I_p$  is  $0.4 \mu s$ . Figure 5.1(a) shows the time variation of  $I_{is}$  measured at the high pressure Ar gas ( $P = 3 \times 10^{-4}$  torr) and at the high beam current ( $I_p = 3$  mA). Since the ion density is large ( $n_i \simeq 10^{10} \text{ cm}^{-3}$ ) and the instability level is small compared with the DC level at this plasma condition, we can measure a clear time evolution of  $I_{is}$ . In fig. 5.1(a),  $I_{is}$  measured at seven different radial positions,  $r=0, 0.5, 1.0, 2.0, 3.0, 4.0$  and  $5.0$  cm from the beam center are shown. The results are extremely reproducible for many different runs. Figure 5.1(b) shows the temporal evolution of the ion radial density profiles reconstructed from fig. 5.1(a). It is clear that the  $n_i$  profile is the same as the beam profile early in time. Then ions start diffusing, and at  $t = 30 \sim 100 \mu s$  they reach the steady state. At this state we find the broad ion profile which is observed in the steady state experiments.

Figure 5.2 shows the time to reach the steady state current level ( $T_{ss}$ ) as a

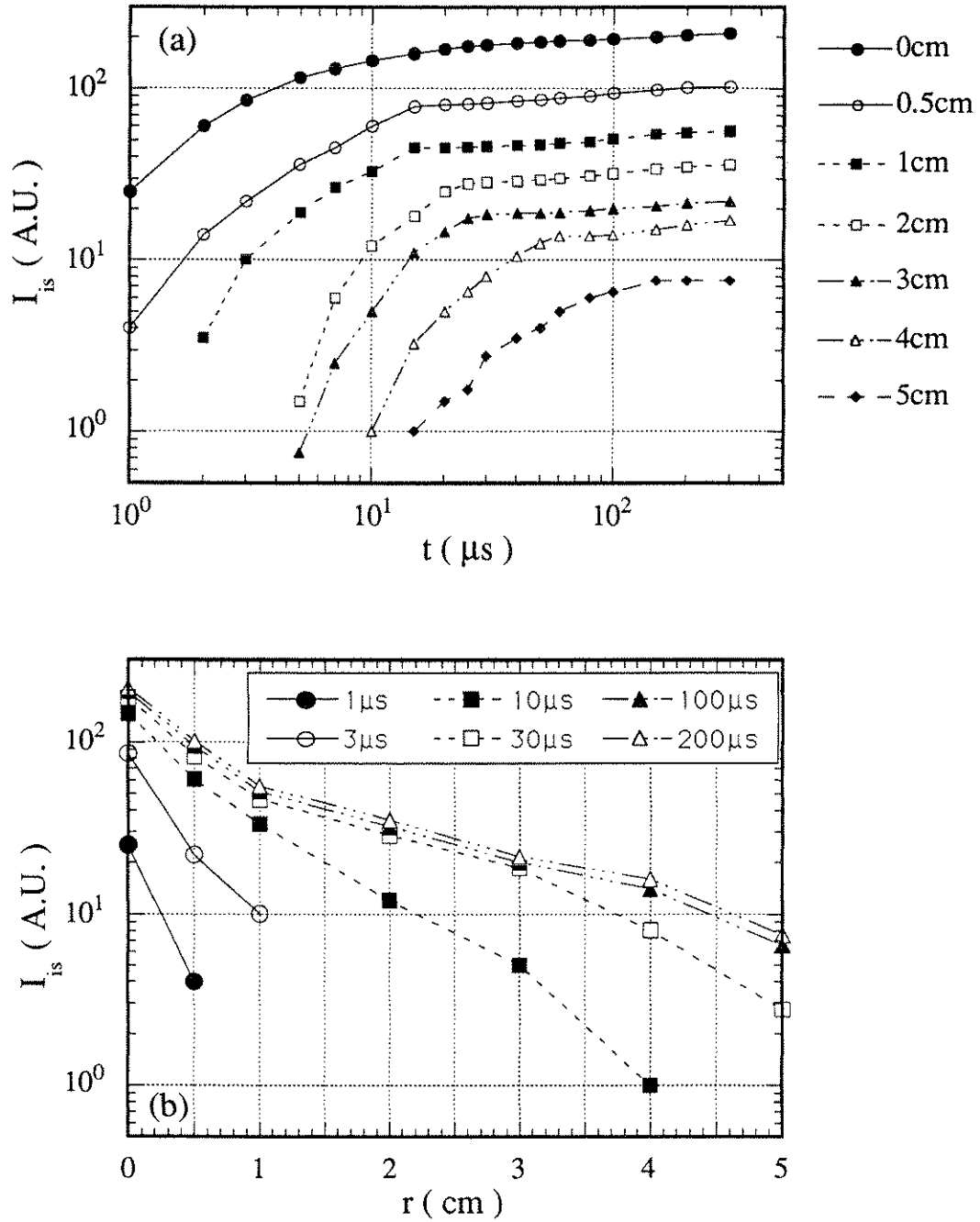


Figure 5.1: (a) Time variation of the ion saturation current measured at high pressure Ar gas ( $P = 3 \times 10^{-4}$  torr) and at high beam current ( $I_p = 3$  mA). (b) The temporal evolution of the ion radial density profiles reconstructed from fig. 5.1(a).

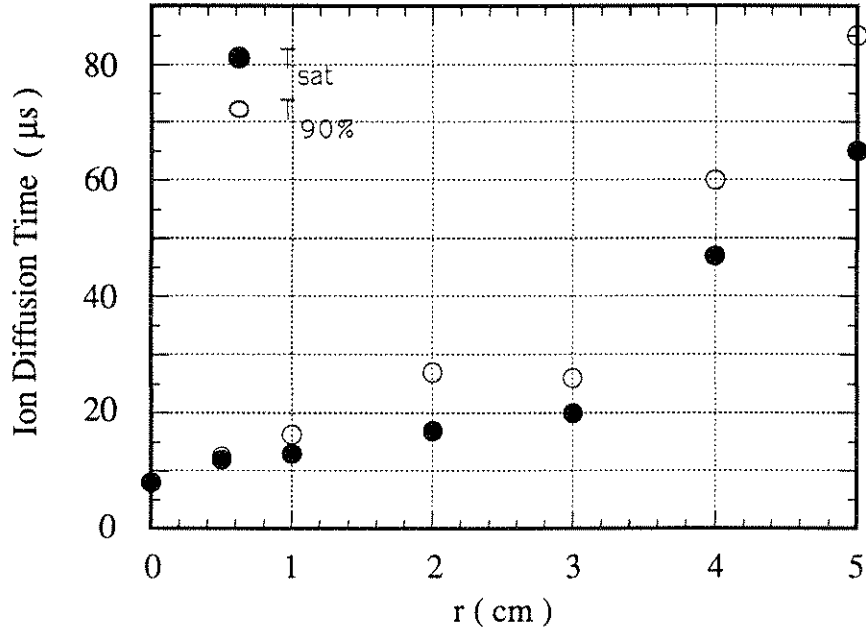


Figure 5.2: Time for  $I_{is}$  to reach the steady state as a function of  $r$

function of the radial position of the probe.  $T_{ss}$  is determined by two methods; one is the time to reach the 90 % of the saturated  $I_{is}$  level ( $T_{90\%}$ ) and the other is determined by extrapolating the linear part of the  $\log I_{is} - \log t$  line to the saturated  $I_{is}$  level ( $T_{sat}$ ). The ion diffusion velocity reduced from the slope of the curve at  $r \geq 3$  cm is calculated to be  $\sim 3.4 \times 10^4$  cm/s. This velocity is an order of magnitude lower than the ion acoustic velocity  $c_s = 3.1 \times 10^5$  cm/s for the  $T_e = 4$  eV case.

Figure 5.3(a) shows the atomic mass,  $A_i$ , dependence of  $v_{Di}$ . We see that  $v_{Di}$  is larger for smaller  $A_i$ . Figure 5.3(b) shows the Ar pressure dependence of the ion diffusion velocity  $v_{Di}$ . It is clear that  $v_{Di}$  is larger for lower pressure.

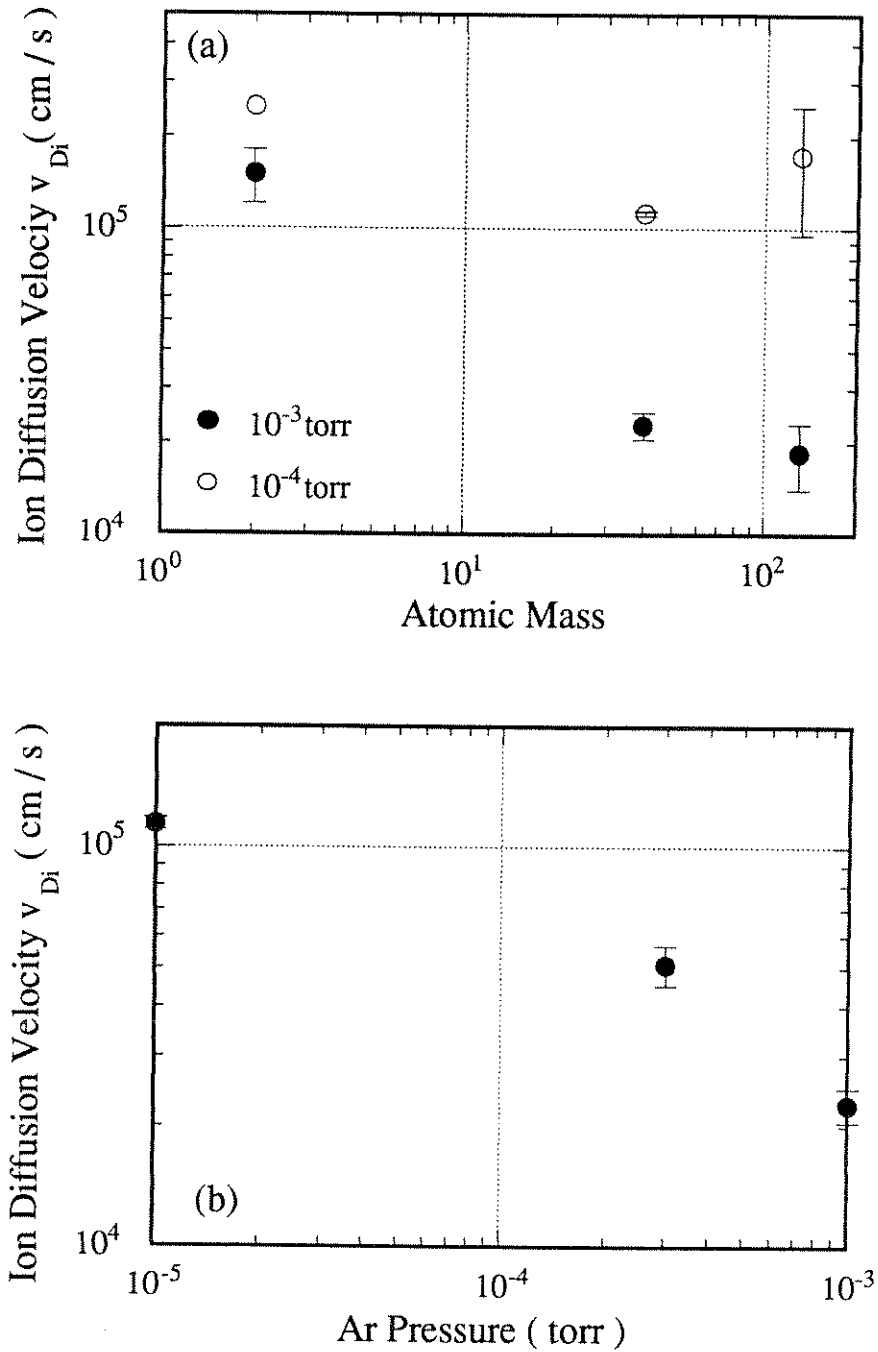


Figure 5.3: (a) Atomic mass and (b) neutral pressure dependence of the diffusion velocities.

### 5.2.2 Instability Onset Measurements

The instability onset measurements have been conducted by applying the pulsed acceleration voltage  $V_B$  as shown in the previous section. We measure the time variation of the electron saturation current fluctuation at the low pressure ( $2 \times 10^{-6}$  torr  $\leq P \leq 5 \times 10^{-5}$  torr) where the MSHI is destabilized. Since the plasma density is low ( $10^7 \text{ cm}^{-3} \leq n_i \leq 10^9 \text{ cm}^{-3}$ ), the ion saturation current fluctuation is not clear compared with the electron saturation current fluctuation.

#### P Dependence of Instability Onset

Figure 5.4 shows the time history of  $I_{es}$  for various Ar pressures measured at  $r = 0.5$  cm. The onset time  $\tau_{onset}$  is shorter for higher P. Figure 5.5(a) shows  $\tau_{onset}$  as a function of P. We see that  $\tau_{onset}$  is inversely proportional to P. The instability frequency  $f_1$  and amplitude  $n_1$  are plotted in fig. 5.5(b) and (c) respectively.

#### $I_p$ Dependence of Instability Onset

Figure 5.6 shows the  $I_p$  dependence of  $\tau_{onset}$  measured at  $r = 0.5$  cm. Since P is high ( $2 \times 10^{-5}$  torr), the onset time  $\tau_{onset}$  is short. We see that  $\tau_{onset}$  becomes shorter for the larger  $I_p$ .

#### r Dependence of Instability Onset

Figure 5.7 shows the radial position dependence of the time variation of  $I_{es}$ . At the plasma center (fig. 5.7(a)), the increase in the DC current level is observed early in time. A fluctuation starts to oscillate roughly  $2.5 \mu\text{s}$  later. At  $r = 0.5$  cm, following a slow increase in the DC current, a clear instability oscillation



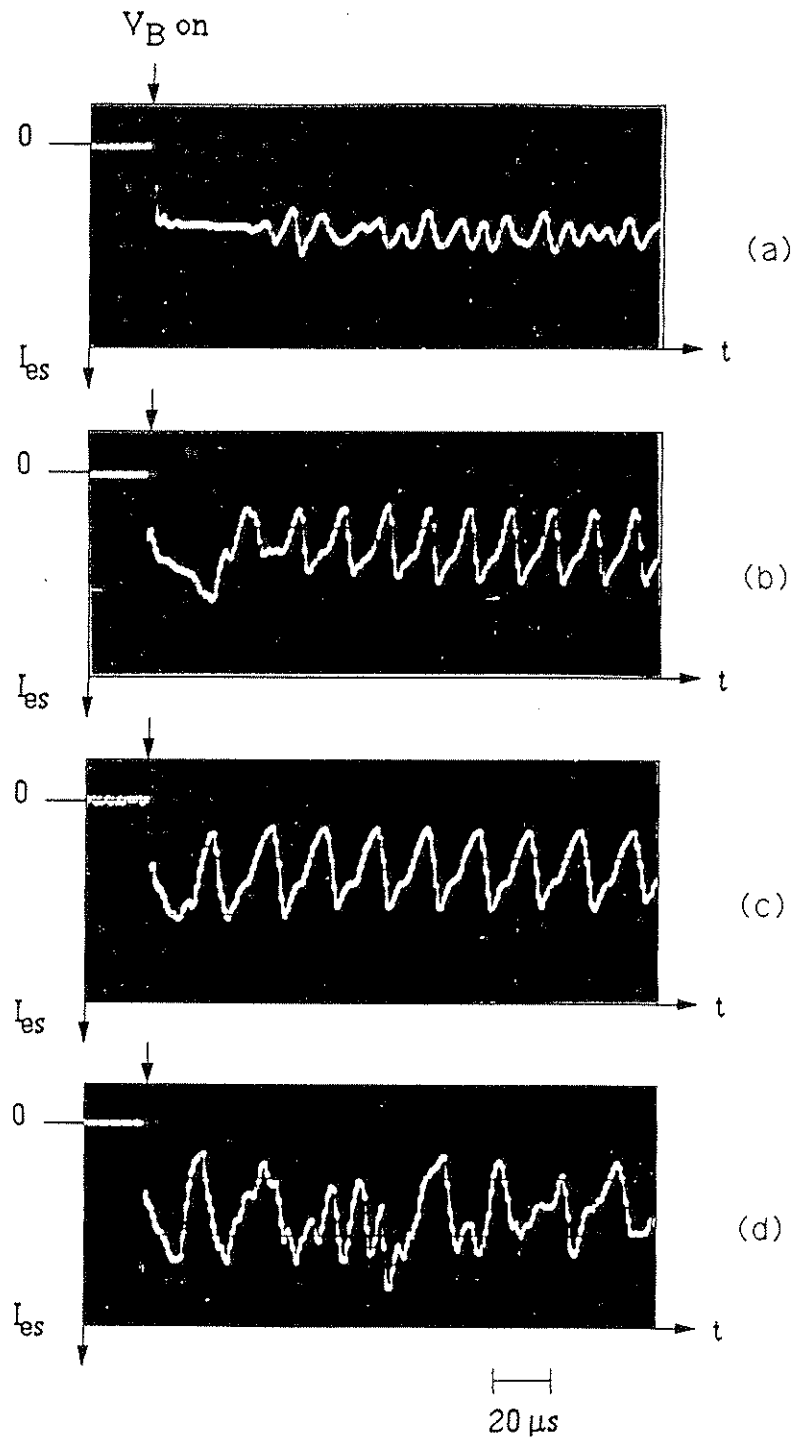


Figure 5.4: Ar pressure dependence of the instability onset measured at  $r = 0.5$  cm,  $I_p = 100 \mu A$ . (a)  $2.1 \times 10^{-6}$  torr, (b)  $1.0 \times 10^{-5}$  torr, (c)  $2.6 \times 10^{-5}$  torr and (d)  $4.0 \times 10^{-5}$  torr. The onset time  $\tau_{onset}$  is shorter for higher pressure.

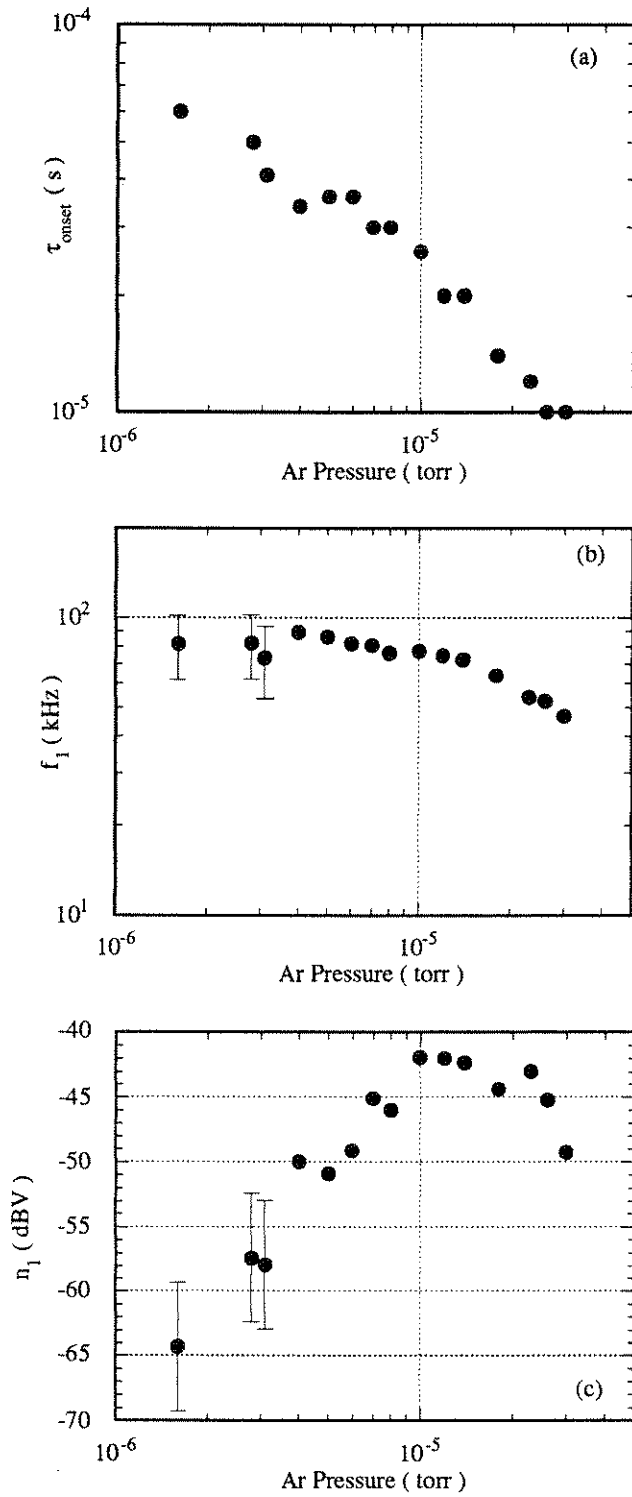


Figure 5.5: Ar pressure dependence of the instability (a) onset time ( $\tau_{onset}$ ), (b) frequency, and (c) amplitude. We see that  $\tau_{onset}$  is inversely proportional to  $P$ .  $I_p = 100 \mu A$ ,  $r = 0.5$  cm.

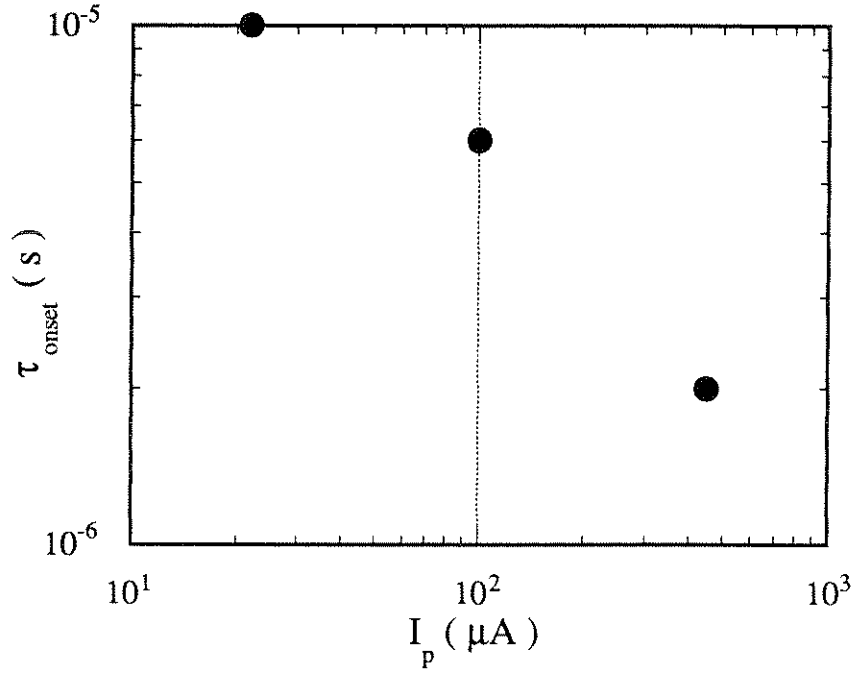


Figure 5.6:  $I_p$  dependence of the instability onset time  $\tau_{onset}$ . We see that  $\tau_{onset}$  becomes shorter for the larger  $I_p$ . Ar  $2 \times 10^{-5}$  torr,  $r = 0.5$  cm .

starts (see fig. 5.7(b)). The amplitude of the oscillation reaches the saturated level after two cycles. Note that the fluctuation shows almost a 100 % oscillation, i.e.,  $n_1/n_0 \simeq 1$ . As shown in fig. 5.7(c), at  $r = 1.0$  cm, neither a DC current increase nor a fluctuation is observed until  $t \simeq 13 \mu\text{s}$ . A clear oscillation starts at  $t \geq 13 \mu\text{s}$  and the fluctuation level is already saturated at the first cycle with  $n_1/n_0 \simeq 0.93$ . These results implies that at  $r \geq 0.5$  cm the electrons are pushed out by the fluctuation.

### 5.2.3 Instability Growth Measurement

In the previous section, we showed that the plasma potential  $\Phi$  can be controlled by varying the endplate bias  $V_{EP}$ . Since the MSHI frequency  $f_1$  depends on  $\Phi$

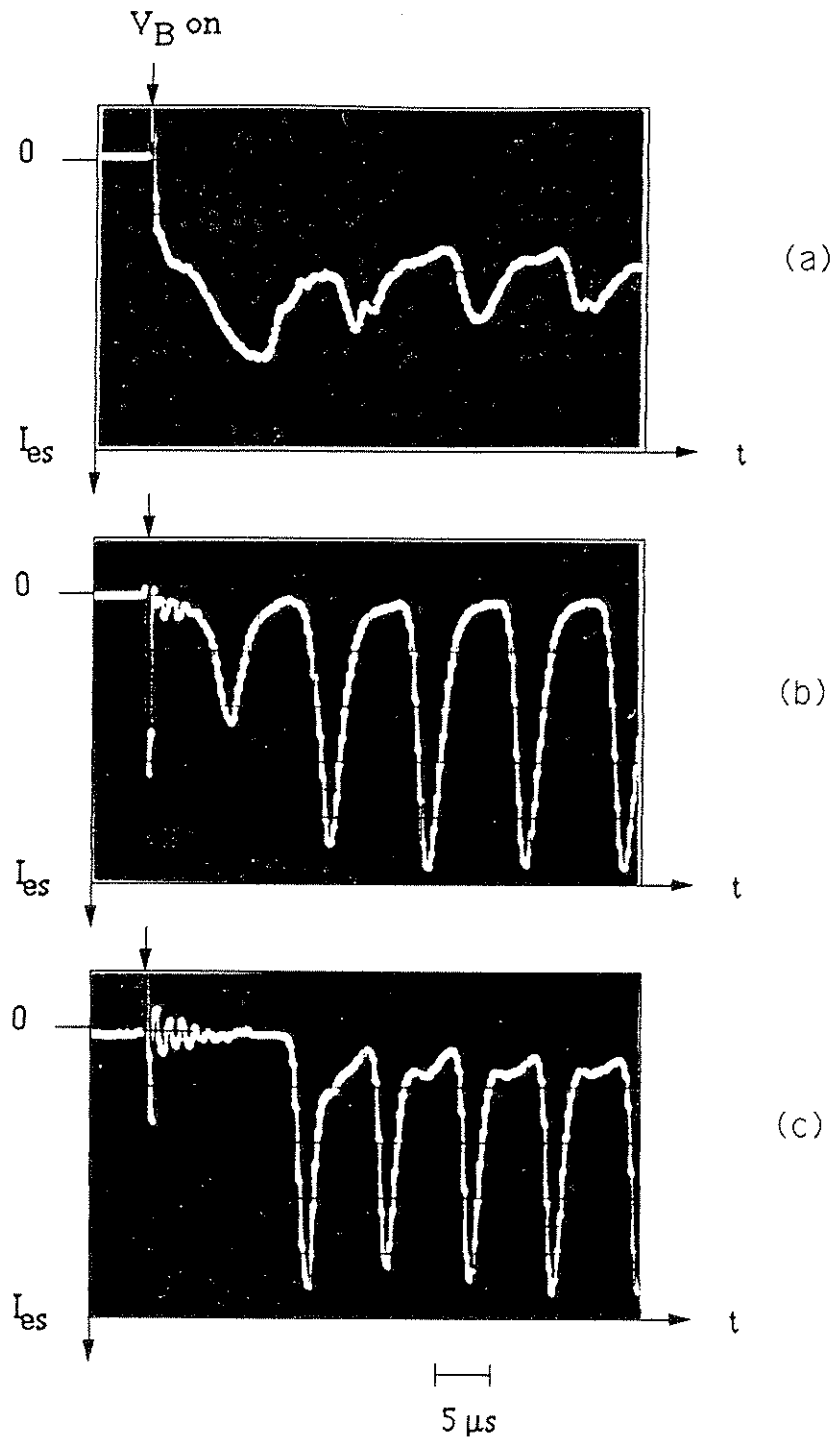


Figure 5.7: Radial position dependence of the electron saturation current measured at (a)  $r = 0$  cm, (b)  $r = 0.5$  cm and (c)  $r = 1.0$  cm. Ar  $2 \times 10^{-5}$  torr,  $I_p = 2000 \mu A$ .

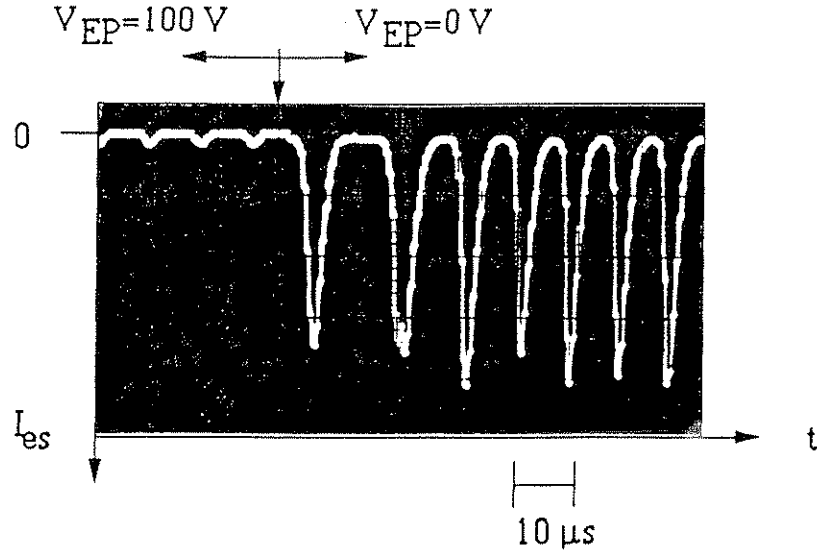


Figure 5.8: End-plate bias voltage dependence of the  $I_{es}$ .  $I_{es}$  shows a significant increase in the amplitude when  $V_{EP}$  is turned off. Ar  $2 \times 10^{-5}$  torr,  $I_p = 2000 \mu\text{A}$  and  $r = 0.5$  cm.

as  $f_1 \propto \Phi^{0.5}$ ,  $f_1$  is controlled by  $V_{EP}$ . We also found that the amplitude of the MSHI,  $n_1$ , strongly depends on  $V_{EP}$ . For example, when the endplate was positively biased, we observed nearly a 30 dBV lower instability level compared with the grounded endplate case. In the experiment, we have applied a positive bias ( $V_{EP} = 10 \sim 100$  V) to the endplate to stabilize the MSHI. Time variations of  $I_{es}$  are measured before and after the bias is electrically turned off and the endplate is grounded.

$V_{EP}$  is turned off within less than  $0.4 \mu\text{s}$ . Figure 5.8 shows a temporal evolution of  $I_{es}$  measured at  $r = 0.5$  cm. The same results are observed by the positively biased probe.  $I_{es}$  shows a significant increase in the amplitude when  $V_{EP}$  is turned off. 90 % of the saturated amplitude level is observed in the first oscillation of  $I_{es}$  which occurs  $7 \mu\text{s}$  after turning off the  $V_{EP}$ . This implies that the growth

rate  $\omega_I$  is larger than the real part of the instability frequency  $\omega_R$ . Note that the instability frequency is varying in time after turning off  $V_{EP}$ . We believe that this frequency variation could be due to the temporal variation of the DC radial plasma potential profile. This issue needs more work in future.

Figure 5.9 shows the instability growth and the instability onset measured for the same conditions at  $r = 0.2$  cm. The instability onset time  $\tau_{onset}$  is longer at the lower P and the lower  $I_p$  as described in the previous section. The instability growth time  $\tau_{growth}$ , however, is always on the order of the instability period, i.e.,  $\omega_I \simeq \omega_R$ . For example, at Ar P =  $2.4 \times 10^{-6}$  torr,  $I_p = 20 \mu\text{A}$ ,  $\tau_{onset}$  is  $150 \mu\text{s}$  (fig. 5.9(c)), while  $\tau_{growth}$  is  $5 \mu\text{s}$  (fig. 5.9(d)). Therefore, the measured P and  $I_p$  dependence of the instability onset time,  $\tau_{onset}$  is not explained by the variation of the instability growth time,  $\tau_{growth}$ . We believe that this longer  $\tau_{onset}$  at the lower P and the lower  $I_p$  is caused by the longer ionization time.

## 5.3 Discussion

### 5.3.1 Ion Diffusion Mechanisms

First, we consider ambipolar ion diffusion. Since ions diffuse more rapidly across the B field than the magnetized electrons, one might expect that an ambipolar electric field would arise to retard the ion diffusion and aid electron diffusion[4, 25]. As a result, a diffusion coefficient might be given by an ambipolar diffusion coefficient  $D_{\perp A}$ ,

$$D_{\perp A} \approx D_{\perp e} \left(1 + \frac{T_i}{T_e}\right), \quad (5.2)$$

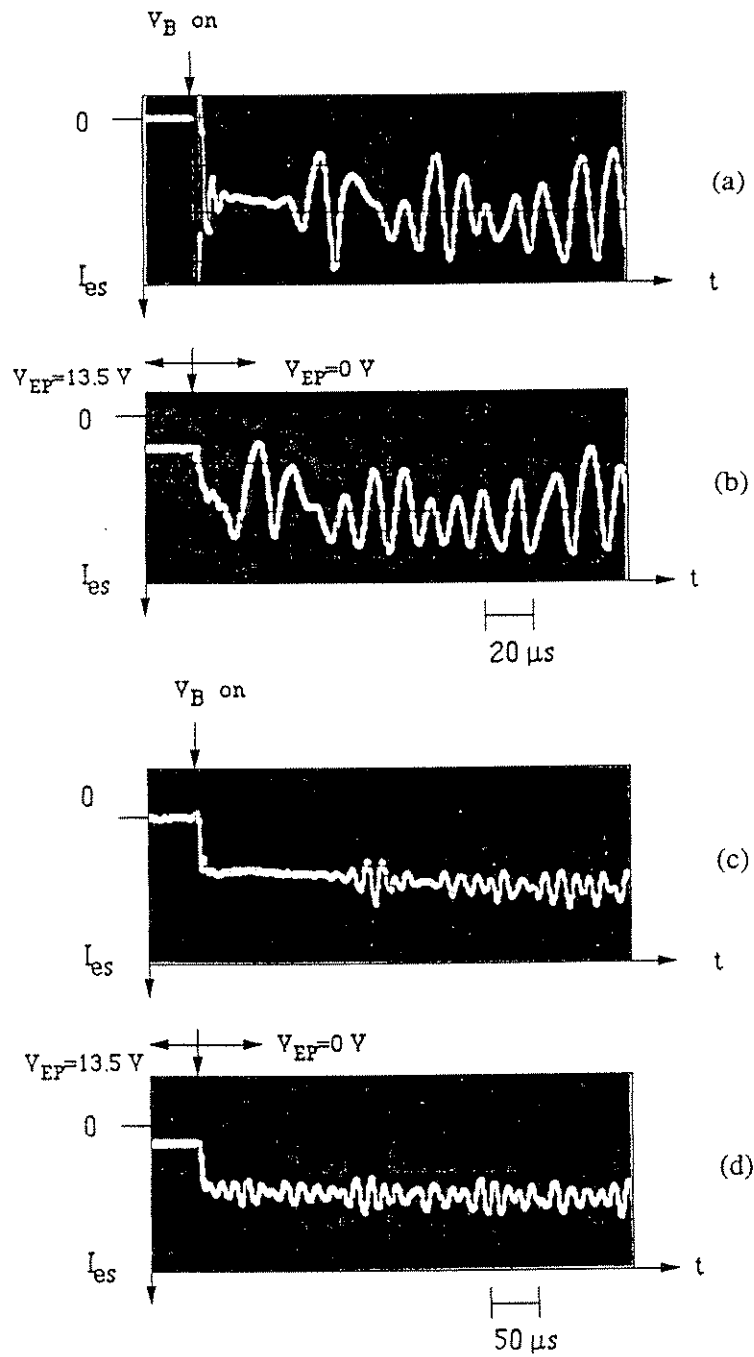


Figure 5.9: End-plate bias voltage dependence of the instability onset and growth. (a) Onset and (b) growth measurements conducted at Ar  $5 \times 10^{-6}$  torr,  $I_p = 100 \mu\text{A}$  and  $r = 0.2$  cm. (c) Onset and (d) growth measurements conducted at Ar  $2.4 \times 10^{-6}$  torr,  $I_p = 20 \mu\text{A}$  and  $r = 0.2$  cm. (c)  $\tau_{onset}$  is 150  $\mu\text{s}$  while (d)  $\tau_{growth}$  is 5  $\mu\text{s}$ .

where  $D_{\perp e} \approx T_e \nu_{en} / (m \Omega_e)$  is the electron perpendicular diffusion coefficient,  $\nu_{en}$  is the electron-neutral collision frequency and  $\Omega_e$  is the electron cyclotron frequency. The ambipolar diffusion velocity  $v_{\perp A}$  is expressed as

$$v_{\perp A} = D_{\perp A} k_{ne}, \quad (5.3)$$

where  $k_{ne} = |n'_{e0} / n_{e0}| = 3.8 \text{ cm}^{-1}$ . When  $T_i \approx T_e$ , the calculated  $v_{\perp A}$  as a function of the gas pressure  $P$  is  $v_{\perp A} = 2.3 \times 10^6 P(\text{torr}) \text{ cm/s}$ . The observed ion diffusion velocity  $v_{Di}$  for  $P = 10^{-5} \sim 10^{-3} \text{ torr}$  shown in fig. 5.3 is much smaller than the calculated velocity of  $v_{\perp A} = 23 \sim 2.3 \times 10^3 \text{ cm/s}$ .

In the derivation of eq. (5.2), we assumed that the diffusion along the B field is negligible, i.e., the plasma is infinite in the direction along the B field. It is pointed out by Simon that when the plasma size is finite along the B field, electrons can move along the B field and short-circuit the electric field caused by the ion diffusion across the B field[26]. As a result, electrons and ions diffuse not with the ambipolar diffusion coefficient but with their own diffusion coefficients. This short-circuit effect is important in short plasma columns with the field lines terminated by conducting plates[4]. Paulikas and Pyle[28] showed that the condition for the perpendicular diffusion to be non-ambipolar is given by

$$\frac{L}{a} < \sqrt{\frac{1}{a k_{ne}} \frac{\Omega_e}{\nu_{en}}}, \quad (5.4)$$

where  $L$  is the plasma length and  $a$  is the plasma radius. For our experimental conditions, Ar gas,  $B = 160 \text{ G}$ ,  $L = 80 \text{ cm}$ ,  $a = 5 \text{ cm}$  and  $k_{ne} = 3.8 \text{ cm}^{-1}$  case, eq. (5.4) is reduced to  $P < 1.2 \times 10^{-2} \text{ torr}$ . Therefore, we expect to have the short-circuit effect and the non-ambipolar radial diffusion in our experiments.



The ion diffusion coefficient  $D_{\perp i}$  is given by[4]

$$D_{\perp i} = \frac{\frac{T_i}{M\nu_{in}}}{1 + \frac{\Omega_i^2}{\nu_{in}^2}}, \quad (5.5)$$

where  $\Omega_i$  is the ion cyclotron frequency and  $\nu_{in}$  is the ion-neutral collision frequency. The ion diffusion velocity  $v_{\perp i}$  is expressed as

$$v_{\perp i} = D_{\perp i} k_{ni}, \quad (5.6)$$

where  $k_{ni} = |n'_{i0}/n_{i0}|$ . When  $\Omega_i/\nu_{in} \ll 1$ , which corresponds to the case when P is large and ions collide with neutrals before they complete a gyrocycle,  $D_{\perp i}$  is given by

$$D_{\perp i} \simeq D_{\parallel i} = \frac{T_i}{M\nu_{in}} \propto P^{-1} M^{-0.5} B^0, \quad (5.7)$$

where  $D_{\parallel i}$  is the ion diffusion coefficient parallel to the direction of the B field. Equation (5.7) is the same as the no magnetic field case. In this case,  $D_{\perp i}$  decreases with P because of the increased ion-neutral collisions. Since ions are unmagnetized, collisions between neutrals slow down the ions. When  $\Omega_i/\nu_{in} \gg 1$ , which corresponds to the low P case,  $D_{\perp i}$  is given by

$$D_{\perp i} \simeq \frac{D_{\parallel i}}{\left(\frac{\Omega_i}{\nu_{in}}\right)^2} = \frac{T_i M \nu_{in}}{e^2 B^2} \propto P M^{0.5} B^{-2}. \quad (5.8)$$

In contrast to the large P case,  $D_{\perp i}$  increases with P. At this low pressure region, unless ions collide with the neutral atoms, they simply gyrate and no diffusion occurs. Therefore, collisions between ions and neutrals are necessary for the diffusion.

Figure 5.10 shows the calculated  $D_{\perp i}$  versus the neutral pressure P for Xe, Ar and H<sub>2</sub>. In fig. 5.10(a), We have assumed that the ion temperature  $T_i$  is 0.03 eV,

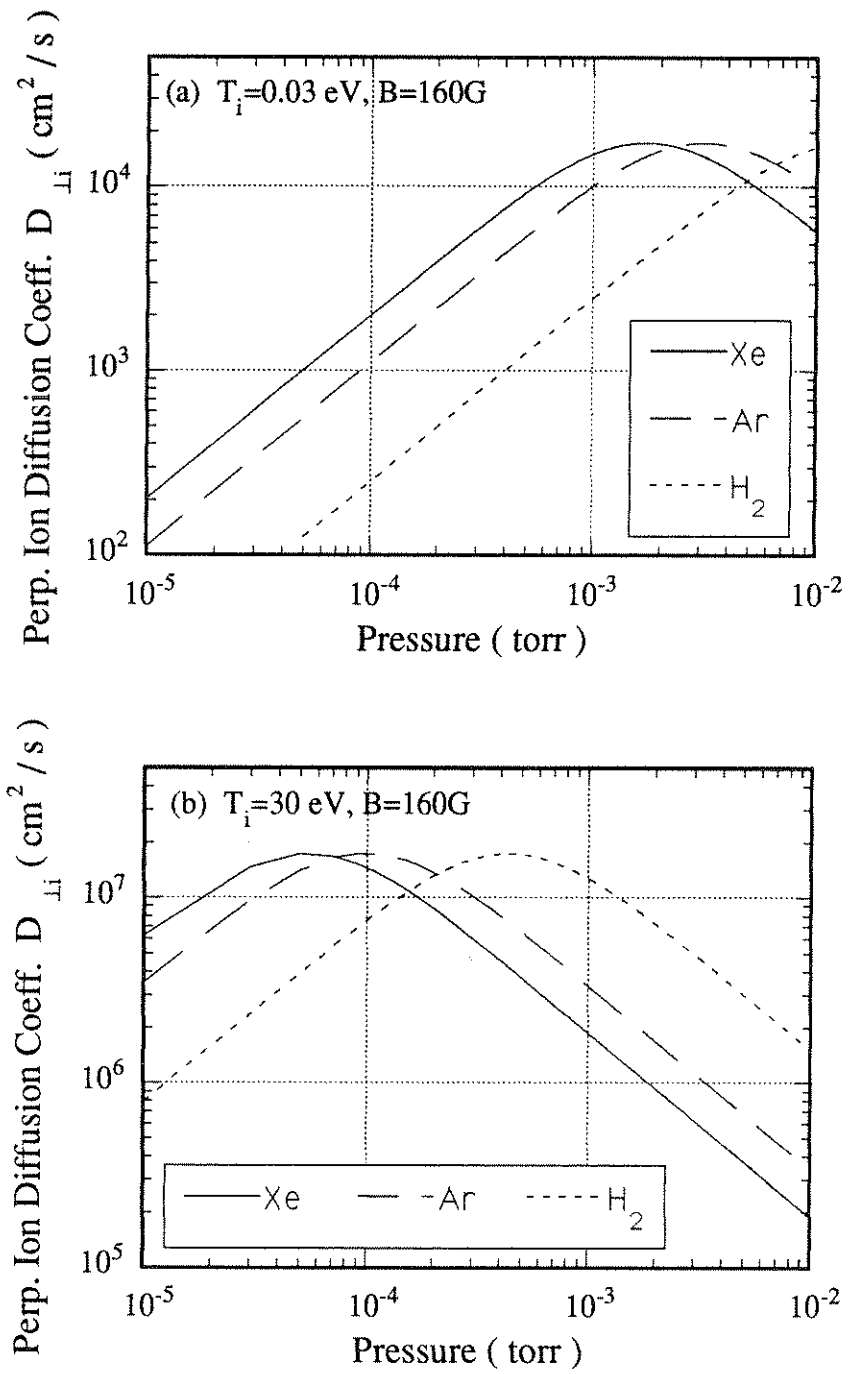


Figure 5.10: Ion temperature and ion mass dependence of the ion perpendicular diffusion coefficient. (a)  $T_i = 0.03\text{ eV}$  and (b)  $T_i = 30\text{ eV}$ .

a room temperature. At the pressure range of  $P = 10^{-5} \sim 10^{-3}$  torr,  $D_{\perp i}$  is larger for larger  $P$  and larger atomic mass  $A_i$ . In our experiment, we have observed that the ion diffusion velocity  $v_{Di}$  decreases with  $P$  and also with  $A_i$  at the pressure range of  $P = 10^{-5} \sim 10^{-3}$  torr. Therefore, if the ion temperature is 0.03 eV or ions are born at the room temperature and no heating occurs, we cannot explain the measured ion diffusion mechanism. Figure 5.10(b) shows the calculated  $D_{\perp i}$  for  $T_i = 30$  eV case. At the pressure range of  $P = 10^{-4} \sim 10^{-2}$  torr,  $D_{\perp i}$  shows a similar dependence on  $P$  and  $A_i$  as the experimental observations, i.e.,  $D_{\perp i}$  decreases with  $P$  and  $A_i$ . However, disagreements with the experiments occur at the lower pressure region ( $P = 10^{-5} \sim 10^{-4}$  torr). Furthermore, the absolute number of the calculated diffusion coefficient at  $T_i = 30$  eV is more than two orders of magnitude larger than the measured coefficient.

As shown in eq. (5.7), when  $\Omega_i/\nu_{in} \gg 1$  is satisfied, the transport of ions across a  $B$  field should be reduced by  $1/B^2$  in a collisional or a classical theory. It was shown that some instabilities enhance the radial loss rates and give rise to anomalous diffusion or turbulent diffusion. Drummond and Rosenbluth[27] showed that the two-stream ion cyclotron instability leads to an anomalous radial diffusion of electrons with a diffusion coefficient similar to the Bohm diffusion coefficient,  $D_B = \kappa T_e/16eB_0$ . Paulikas and Pyle[28] studied the current convective instability in the positive column of the glow discharge and showed that the experimental results agree fairly well with the predictions made by Kadomtsev and Nedospasov[29]. Turbulent diffusion arising from the Simon-Hoh instability[19, 20] was investigated by Thomassen[21].

Turbulent ion heating caused by instabilities has been studied by many authors. In non-isothermal plasmas ( $T_e \gg T_i$ ), Mah et al. observed a rapid ion heating caused by an axial electron current driven ion acoustic wave[30]. They showed that the ion heating stops when the electron drift velocity becomes smaller than the critical velocity for the growth of the ion acoustic wave, which is decided by the ion Landau damping. In isothermal plasmas ( $T_e \simeq T_i$ ), ion heating caused by the discrete-spectrum ion cyclotron drift wave ( $\omega \simeq n\Omega_i$ ), continuous-spectrum ion cyclotron drift wave ( $\omega \simeq \omega_i^* \gg \Omega_i$ ) and the two-stream lower-hybrid instability ( $\omega \simeq \omega_{LH} \simeq \omega_{pi}$ ) was reported by Yamada et al.[31, 32, 33], where  $\Omega_i$ ,  $\omega_i^*$ ,  $\omega_{LH}$  and  $\omega_{pi}$  are the ion cyclotron, the ion diamagnetic drift, the lower hybrid and the ion plasma frequencies, respectively. The ion heating mechanism of the discrete-spectrum ion cyclotron drift wave (ICDW)[31, 33] was explained by the resonant ion cyclotron damping. They showed that the measured ion heating rate agrees with the calculated heating rate from the quasilinear theory. In the case of the continuous-spectrum ICDW[31, 33] and the lower-hybrid instability[32], they considered the renormalized quasilinear theory[34] by introducing the nonresonant stochastic heating term. For the lower-hybrid heating case, even though the instability amplitude showed a discrete-spectrum, stochasticity was introduced because of the large growth rate of the instability.

We believe that the stochastic heating by the MSHI occurs in our experiments. In order to resolve this issue, future work in this area should include time resolved ion temperature measurements.

# Chapter 6

## Nonlinear Evolution of the MSHI

### 6.1 Introduction

In this chapter, we discuss the nonlinear evolution of the MSHI. As the parameters  $I_p$  or  $P$  is varied to increase the amplitude of  $M_1$ , a second mode  $M_2$  with a frequency  $f_2 < f_1$  appears at the low-frequency end as do sideband modes  $M_s$  at  $f_s = f_1 \pm f_2$ . As seen in chapter 2 (see fig. 2.12) the onset of  $M_2$  and  $M_s$  are characterized by a decrease in the amplitude of  $M_1$  ( $n_1$ ) when  $I_p$  is used as the control parameter. Thereafter, as we continue to increase  $I_p$ ,  $n_1$  continues to increase monotonically. Whereas  $n_2$  and  $n_s$ , the amplitudes of  $M_2$  and  $M_s$ , show a strong increase when the  $M_2$  and  $M_1$  are frequency locked. If the pressure is used to control the amplitudes of  $M_1$ ,  $M_2$  and  $M_s$ ,  $n_1$  shows a monotonic increase with pressure with no discernible drop in its amplitude. However,  $n_2$  and  $n_s$  do show

a strong growth when the  $M_1$  and  $M_2$  modes are frequency locked to one another as in the  $I_p$  scan. For given  $I_p$ , as  $P$  is increased, the ratio of  $f_1/f_2$  decreases and exhibits frequency locking at 4, 3 and 2. While  $M_1$  peaks off-axis,  $M_2$  has a peak on axis, and we showed that it is an  $m = 0$  mode. Both  $f_1$  and  $f_2$  are nearly independent of  $r$ . While  $f_1$  scales as  $1/\sqrt{M}$ ,  $f_2$  is independent of the ion mass. However, as will be shown <sup>in</sup> this chapter,  $f_2$  has an excellent correlation with the “bounce frequency” i.e.,  $f_2 \approx f_b = \frac{1}{2\pi} \sqrt{\frac{ek_z^2 \phi_1}{M}}$  where  $\phi_1$  is the fluctuating plasma potential. The correlation of  $f_2$  with  $f_b$  would indicate that  $f_2$  should have a  $1/\sqrt{M}$  dependence. However, since  $\phi_1$  scales as  $M$  (see fig. 6.2),  $f_2$  is independent of the atomic mass.

We now propose the following interpretation of the above mentioned observations. As already stated,  $M_1$  is identified as the modified Simon-Hoh instability ( $k_z \simeq 0$ ) driven in an inhomogeneous plasma with strongly magnetized electrons and weakly magnetized ions. When  $M_1$  attains a sufficiently large amplitude, it traps a significant number of ions in the wave potential. The  $M_1$  mode is now driven modulationally unstable to sideband modes  $M_s$  with frequencies  $f_1 \pm f_2$  (where  $f_2 \approx f_b$ , the bounce frequency of trapped ions) via a nonlinear coupling introduced by the trapped particles.

## 6.2 Particle Trapping Instability Theory

We now consider the process of ion trapping in a large amplitude  $M_1$  mode. Introducing  $\xi = ky - \omega t$  (where  $y$  represents the  $\theta$ -coordinate in a slab approximation)

we get the ion orbit equation

$$\ddot{\xi} + [\Omega_R^2 + \Omega_i^2 + \omega_B^2 \cos \xi] \dot{\xi} \cong (k_\theta V_{\theta i} - \omega) \Omega_R^2 \quad (6.1)$$

where  $\omega_B = \sqrt{ek_\theta^2 \phi_1 / M}$  is the ion bounce frequency in the wave potential,  $\Omega_i = eB_0 / M$  is the ion cyclotron frequency and  $\Omega_R = \sqrt{2e\Phi_0 / Mr_0^2}$  is the ion rattle frequency in the DC parabolic electrostatic well as described in chapter 3. To get significant ion trapping, we should have  $\omega_B^2 > (\Omega_R^2 + \Omega_i^2)$ . This would have been difficult, if the radial electrostatic well were truly parabolic. However, the  $M_1$  mode maximizes at a radius where  $\Phi'$  is already small so that the effective  $\Omega_R^2$  is considerably reduced. Thus we find that a  $\phi_1$  is sufficiently large to result in significant ion trapping. The RHS of eq. (6.1) shows that ions will stay trapped for a time  $\Delta t$  such that  $\bar{\xi} \Delta t \sim (k_\theta V_{\theta i} - \omega) \Delta t \sim 1$ . The effects we consider below should therefore take place in times shorter than this time.

We now consider excitation of side-band instabilities by the trapped ions in the large amplitude  $M_1$  mode. Following, Kruer et al.[35] and Goldman[36] we now write the mode-coupling equations for the side-band instability as follows:

$$\left[ \epsilon_s(\omega, \underline{k}) - \frac{\omega_T^2}{(\omega - \underline{k} \cdot \underline{v}_p)^2 - \omega_B^2} \right] E_s(\omega, \underline{k}) = \frac{\omega_T^2}{(\omega - \underline{k} \cdot \underline{v}_p)^2 - \omega_B^2} E_2(\omega - \omega_o, \underline{k} - \underline{k}_o) \quad (6.2)$$

$$\left[ \epsilon_2(\omega - \omega_o, \underline{k} - \underline{k}_o) - \frac{\omega_T^2}{(\omega - \underline{k} \cdot \underline{v}_p)^2 - \omega_B^2} \right] E_2(\omega - \omega_o, \underline{k} - \underline{k}_o) = \frac{\omega_T^2}{(\omega - \underline{k} \cdot \underline{v}_p)^2 - \omega_B^2} E_s(\omega, \underline{k}) \quad (6.3)$$

where  $\omega_T^2 = 4\pi e^2 n_T / M$ ,  $n_T$  is the ‘density’ of trapped particles and we have neglected the coupling to the upper sidebands, which is somewhat weaker in the

experiments. It has been assumed that the coupling effects of the  $M_1$  mode only enter through trapped particle effects. The  $\epsilon_s$  and  $\epsilon_2$  refer to the dielectric response at frequencies  $\omega$  and  $\omega - \omega_o$  as described above. The dispersion relation is obtained from the determinant as

$$1 = \frac{\omega_T^2}{(\omega - \underline{k} \cdot \underline{v}_p)^2 - \omega_B^2} \left[ \frac{1}{\epsilon_S(\omega, \underline{k})} + \frac{1}{\epsilon_2(\omega - \omega_o, \underline{k} - \underline{k}_o)} \right] \quad (6.4)$$

### 6.3 Verification of Particle Trapping Instability

In this section, we show experimental evidence for  $M_2$  and  $M_s$  being driven by the particle trapping instability (PTI). In a wave-frame of  $M_1$ , ions are bouncing azimuthally back and forth in a wave potential of  $M_1$  with the bounce frequency,  $f_b = \frac{1}{2\pi} \sqrt{\frac{ek_\theta^2 \phi_1}{M}}$ . Therefore, in the lab-frame,  $M_s$ , whose frequency is  $f_s = f_1 \pm f_b$ , is thought to be the PTI mode driven unstable by trapped ions.  $M_s$  also satisfies the dispersion relation of the MSHI, with a somewhat different  $k_\theta$  from  $M_1$  due to the radial amplitude peak position shift. Since  $M_s$  is a resonant plasma mode,  $M_s$  shows a large response at  $f_s$ .

$M_2$  mode frequency is a beat frequency of  $f_1$  and  $f_s$ , i.e.,  $f_2 = f_1 - f_s = f_b$ .  $M_2$  response is also large because it is at resonance with a kinetic ion mode. As shown in chapter 2, the wave numbers of  $M_2$  are  $k_{z2} = 0$ ,  $k_{\theta 2} = 0$  and  $M_2$  is a radially standing wave (see table 2.2). Similar wave numbers and radial amplitude profiles (see fig. 2.18) were observed in electrostatic ion cyclotron wave experiments[37].

Instability measurements were conducted by collecting fluctuating electron current for several plasma conditions by varying  $I_p$ , P and B (see chapter 2). We have observed that  $f_2$  scales as  $f_2 \propto \sqrt{n_1}$  as shown in fig. 2.16(b). In this section,



first we show more details on  $f_2$  scaling on  $n_1$ . Then we will show  $\phi_1$  measurement results and compare  $f_2$  to  $f_b$ .

### 6.3.1 $n_1$ Dependence of $f_2$

The P dependence of  $f_2$  is shown in fig. 6.1(a), which reveals strong P dependence. The  $n_1$  dependence of  $f_2$  is shown in fig. 6.1(b). We find that  $f_2$  scales as  $f_2 \propto \sqrt{n_1}$  very well regardless of the pressure variation or plasma condition.

No ion mass (M) dependence is observed in  $f_2$  (see fig. 2.15(a)). However, since  $n_1$  has M dependence (fig. 2.16(a)), if we plot  $f_2$  versus  $n_1$ ,  $f_2$  shows M dependence for a given  $n_1$  (fig. 2.16(b)). This implies that  $n_1$  scales as  $n_1 \propto M$  and  $f_2 \propto \sqrt{n_1/M} \propto \sqrt{M/M} \propto M^0$ .

### 6.3.2 $\phi_1$ Measurements

As we have shown in chapter 3,  $n_1$  and  $\phi_1$  are related to each other by the modified Boltzmann relation as

$$\frac{n_1}{n_0} = \frac{e\phi_1}{T_e} \frac{\omega^*}{\omega - \omega_E} \approx \frac{e\phi_1}{T_e} \frac{\frac{T_e}{eB_0} k_n k_\theta}{-\frac{E_0}{B_0} k_\theta} = \frac{k_n}{k_\phi} \frac{\phi_1}{\Phi} \quad (6.5)$$

where  $k_n = \frac{1}{n_0} \frac{dn_0}{dr}$  and  $k_\phi = \frac{1}{\Phi} \frac{d\Phi}{dr}$ . If  $\frac{k_n}{k_\phi} \frac{n_0}{\Phi}$  is a constant,  $n_1$  scales as  $n_1 \propto \phi_1$  and  $f_2$  agrees with bounce frequency scaling,  $f_b \propto \sqrt{\phi_1/M}$ . In order to show that  $f_2 = f_b$ , we measured  $\phi_1$  with the emissive probe described in chapter 2. The wave potential of the  $M_1$  mode,  $\phi_1$ , is obtained from a fluctuating component of the floating potential of the emissive probe. Figure 6.2(a) shows  $\phi_1$  and DC plasma potential difference ( $\Delta\Phi$ ) between the center and  $r = 1.5 \sim 2.0$  cm. The  $\phi_1$  measurement was conducted at the center. Figure 6.2(b) shows measured  $f_1$ ,

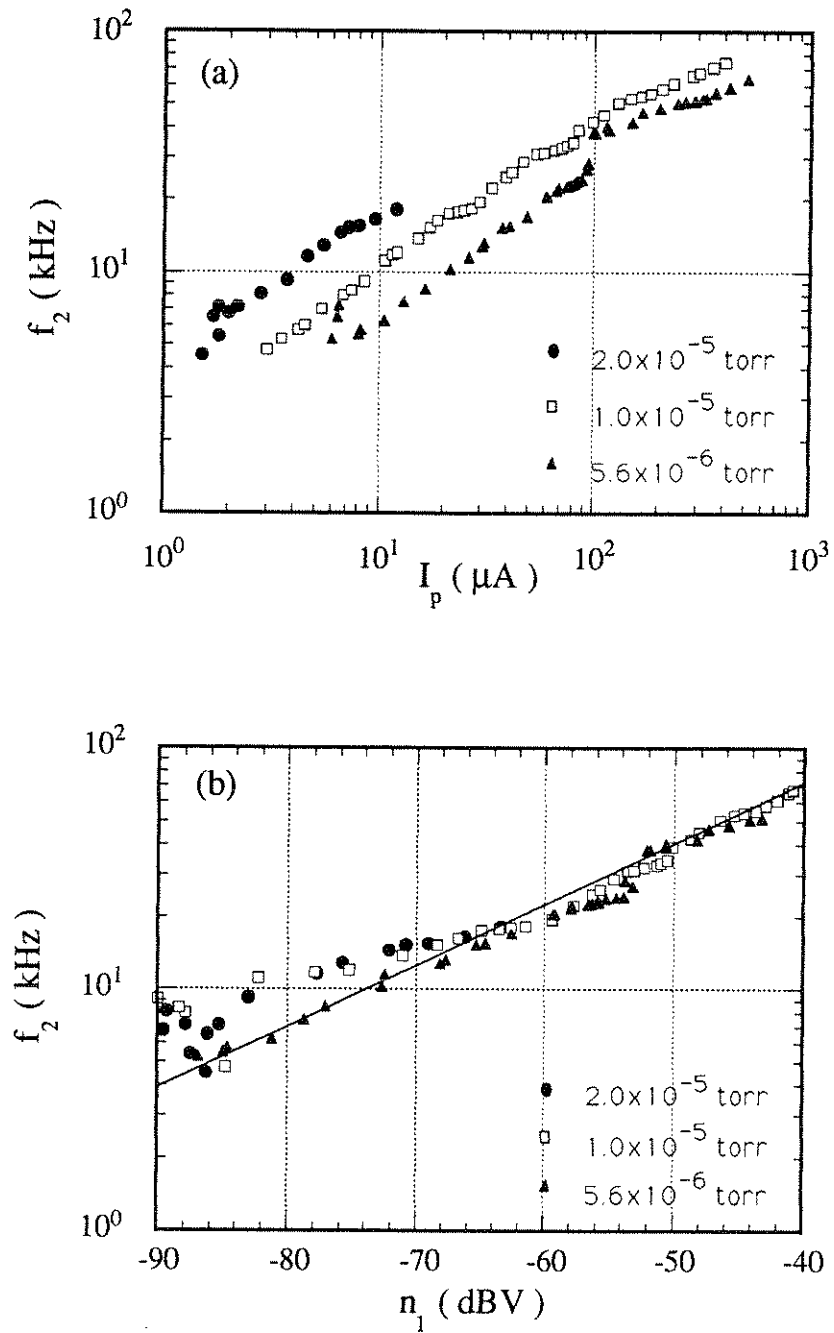


Figure 6.1: Ar pressure dependence of (a)  $f_2$  VS  $I_p$  and (b)  $f_2$  VS  $n_1$ .  $f_2$  scales as  $f_2 \propto \sqrt{n_1}$  very well regardless of the pressure variation.

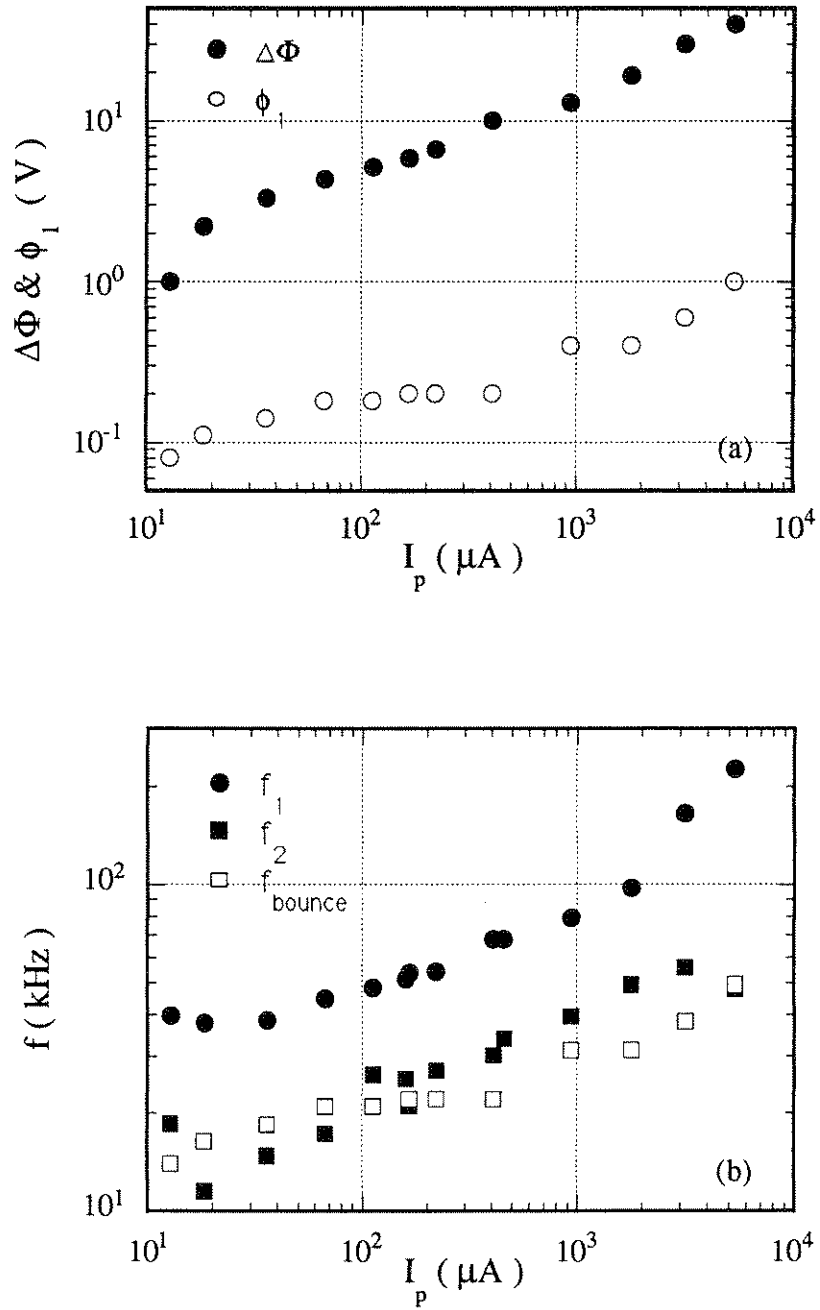


Figure 6.2:  $I_p$  dependence of (a)  $\Delta\Phi$  and  $\phi_1$  and (b) the calculated  $f_{\text{bounce}}$ . We see that  $f_2$  and  $f_b$  agree not only in the dependence on  $I_p$  but also absolute value.

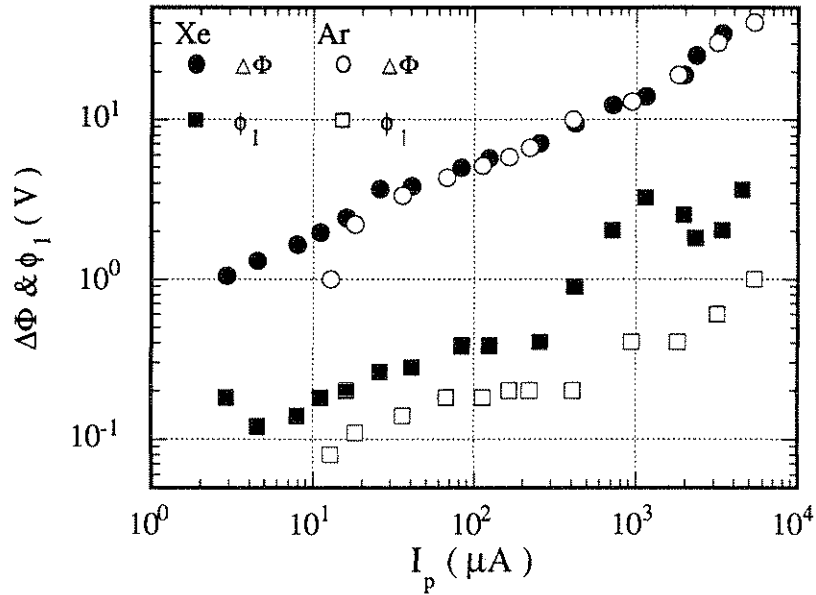


Figure 6.3: Ion mass dependence of  $\Delta\Phi$  and  $\phi_1$ . No ion mass dependence is observed for  $\Phi$ , while,  $\phi_1$  scales as  $\phi_1 \propto M$ .

$f_2$  and calculated  $f_b$ . We see that  $f_2$  and  $f_b$  agree not only in the dependence on  $I_p$  but also absolute value.

Figure 6.3 shows the ion mass dependence of  $\Delta\Phi$  and  $\phi_1$ . No ion mass dependence is observed for  $\Phi$ , while  $\phi_1$  scales as  $\phi_1 \propto M$ . As shown in chapter 4,  $f_1$  scales as  $f_1 \propto \sqrt{\Phi/M}$  and  $\Phi$  has no ion mass dependence. Therefore, we find a  $M^{-0.5}$  dependence on  $f_1$ . On the other hand, even though  $f_2$  scales as  $f_2 \propto \sqrt{\phi_1/M}$ , since  $\phi_1$  shows  $M$  dependence, no ion mass dependence is observed for  $f_2$ .

## 6.4 Mode Coupling

We now give an interpretation of the mode-locking behavior observed in the experiments. The strongest mode-locking effects are observed when  $\omega_s \approx \omega_2 \approx \omega_1/2$ . This may be directly seen from the mode coupling equations. We can readily explain these equations in the standard form

$$\ddot{x}_2 - \omega_2^2 x_2 = \alpha x_1(t) x_s \quad (6.6)$$

$$\ddot{x}_s - \omega_s^2 x_s = \beta x_1(t) x_2 \quad (6.7)$$

where the space dependencies have been removed by Fourier analysis and we have retained the time-dependence in  $x_1$ . For  $\omega_2 \cong \omega_s$ , the two equations become degenerate; if we introduce  $x_2 = \sqrt{\alpha/\beta} x_s$ , one may write

$$\ddot{x}_s + [\omega_s^2 - \sqrt{\alpha\beta} x_1(t)] x_s = 0.$$

When  $\omega_s \sim \omega_1/2$ , we have essentially the unstable Mathieu oscillator, where the excited frequency is  $\omega_1/2$  over a range of  $\omega_s$  given by  $\delta\omega_s \sim \sqrt{\alpha\beta}$ . This is the mode-locking behavior observed in the experiment. The mode-locking behavior at integers other than 2, i.e.,  $\omega_2 \cong \omega_1/n$ , corresponds to equations nonlinear in  $\omega_2$  and are beyond the scope of present theory; they are understandably weaker in experiments.

## 6.5 Summary

We believe that a finite amplitude  $M_1$  mode is driven modulationally unstable by ion trapping effects leading to the excitation of  $M_2$  modes and the sideband modes

$M_s$ . We have also shown that the final state can be a new periodic oscillation, the mode-locked state with  $f_2 = f_s = f_1/2$ . Such a periodic state is likely to be further modulationally unstable to a low-frequency  $M_3$  mode at a frequency  $f_3$  which will then migrate and perhaps mode-lock at  $f_2/2$  and so on. Thus, what at first sight appears to be a simple period doubling route of chaos follows a rather complex path starting at the low-frequency modulational end and finally mode-locking at the sub-harmonic.

We believe that this scenario of a sequence of modulational instabilities leading to the turbulent state may be quite generic to plasma systems. In many instances, the plasma either excites coherent modes or leads to coherent excitations by a nonlinear condensation of the energy in some wave length regions (e.g. in long wave length plasmas, long-scale drift vortices in drift wave turbulence, etc.). The plasma must then find a way of entering the turbulent state through a series of modulational instabilities. The detailed nonlinear physics of the modulational instability can be different in different cases. For strong plasma wave turbulence, the collapse mechanisms investigated by Zakharov[38] are an example of such modulational instabilities. In our experiment, there is very clear evidence of such a sequence of events involving trapped particle effects. This general picture is also consistent with the picture of onset of chaos in nonlinear oscillators involving sub-harmonic generation, which can also be looked upon as a series of modulational instabilities[39].

The physical mechanism of the  $M_2$  mode (and indeed  $M_{n+2}$  modes, where  $n = 0, 1, 2, ..$ ) is not yet understood. The  $M_2$  mode is a  $m = 0$  mode which has a density peak at the beam center and a rather deep near-null at about the

beam edge, together with a rapid radial phase change of 180 degrees across the near-null with nearly uniform radial phase elsewhere. The initially most plausible option for  $M_2$ , a nearly radially propagating ion sound wave mode, seems ruled out since careful axial measurements show that any axial  $k_z$  is too small to allow enough electron flow along the field lines required to nearly shield ion oscillations in the usual manner. The likely explanation is that it is some sort of hybrid mode between the electron rich inner core and the very rich ion-kinetic halo.

When there are two modes  $M_2$  ( $m = 0$  mode) and  $M_s$  ( $m = 1$  mode) the fact that their frequencies sum to the MSHI frequency  $f_1$  together with the fact that the daughter azimuthal mode numbers also sum to the MSHI mode ( $0 + 1 = 1$ ), all point to the parametric decay scenario. Unfortunately, the basic physics of the two daughter modes is not yet understood. Therefore one cannot yet form the desired linear mode operators on the mode variables for each daughter mode, let alone the coupling between the daughter modes and the pump.

On carefully examining the data shown in fig. 2.12, in the vicinity of the onset of the coupled modes, one notices the sudden drop of the pump, and a rise of the daughter modes but subsequent steady co-existence of  $M_1$ ,  $M_2$  and  $M_s$  all at comparable levels. Although  $n_2$  and  $n_s$  show amplitude peaks when frequency locking occurs,  $n_1$  continues to increase monotonically. This suggests that a three-mode-coupled system is not the whole story. It may be plausible that the beam plays a critical role in determining the plasma conditions. Since the role of the beam is neglected in the computer simulations to be discussed next (only electron and ion profiles are initiated) one perhaps does not expect to see the rich nonlinear behavior in the simulations.

# Chapter 7

## Computer Simulations

In order to get better insights into the MSHI, we have run a  $2\frac{1}{2}$  dimensional cylindrical boundary electrostatic particle-in-cell computer simulation, SYLSIM [40].

The calculations were performed on a  $128 \times 128$  grid with 8000 ions and 8000 electrons. Since the beam electron density is nearly two orders of magnitude lower than the plasma electron density, we have neglected the beam electron component. In order to create the DC radial electric field, we have applied different radial profiles for electrons and ions. Both of them have Maxwellian distribution functions and Maxwellian density profiles,  $n_j = n_{j0} \exp(-r^2/r_{j0}^2)$ , where  $j = i$  for ions and  $j = e$  for electrons. However,  $r_{i0}$  is larger than  $r_{e0}$  as observed in the experiments. In order to satisfy total charge neutrality in 2-D, we have chosen  $n_{i0} = n_{e0}(r_{e0}/r_{i0})^2$ . Initial parameters are  $M/m = 800$ ,  $T_e/T_i = 100$  and  $\omega_{ce}/\omega_{pe} = 1$ . These parameters correspond to  $r_{e0} = 0.5$  cm,  $r_{i0} = 2.0$  cm,  $n_{e0} = 10^8$  cm $^{-3}$ ,  $n_{i0} = 6.25 \times 10^6$  cm $^{-3}$ ,  $\Delta\Phi = 30$  V,  $T_e = 4$  eV,  $T_i = 0.04$  eV and  $B = 32$  G.



As shown in chapter 4, the instability frequency of the MSHI is decided by the effective ion Larmor radius term,  $b = k_{\perp}^2 e \Delta \Phi_0 M / (\epsilon B_0)^2$ . Since M ( $M/m = 800$ ) is two orders of magnitude smaller than the Ar mass ( $M/m = 7.4 \times 10^4$ ), we have chosen a smaller B and a larger  $\Delta \Phi_0$  in the simulation.

In this code, electrons have positive and ions have negative charge. Therefore, the DC electric field is radially outward and the  $E_{r0} \times B_0$  drift is in the  $-\hat{\theta}$  direction. The azimuthal charge separation caused by the slower ion drift and the consequent azimuthal electric field  $E_{\theta 1}$  is in the  $\hat{\theta}$  direction. As a result, the  $E_{\theta 1} \times B_0$  velocity is in the  $\hat{r}$  direction which enhances the density perturbation. Therefore,  $\nabla n_0 \cdot \vec{E}_{r0} < 0$  is an instability condition in the simulation.

Note that because of the positive charge of the electrons, the Boltzmann relation is expressed as

$$\frac{n_{e1}}{n_{e0}} = -\frac{e\phi}{T_e}. \quad (7.1)$$

Therefore, when the Boltzmann relation is satisfied, we find a 180 degree phase shift between  $\phi$  and  $n_e$  oscillations. On the other hand, the modified Boltzmann relation is expressed as

$$\frac{n_{e1}}{n_{e0}} = -\frac{e\phi}{T_e} \frac{\omega^*}{\omega - \omega_E}. \quad (7.2)$$

When the condition  $\omega \ll \omega_E$  is satisfied, eq. (7.2) is reduced to

$$\frac{n_{e1}}{n_{e0}} \approx \frac{e\phi}{T_e} \frac{\omega^*}{\omega_E}, \quad (7.3)$$

and  $\phi$  and  $n_e$  oscillations are in phase. Since the modified Boltzmann relation with large  $E \times B$  drift is satisfied in our experiment, as shown in the theory, we expect to see  $\phi$  and  $n_e$  oscillations in phase in the computer simulation. The  $\phi$

and  $n_i$  relation is expressed by eq. (3.34) and it is reduced to

$$\frac{n_{i1}}{n_{i0}} \approx -\frac{e\phi}{T_e} \frac{c_s^2 k_y^2}{(\omega - k_y v_{\theta i})^2} \quad (7.4)$$

in the simulation.

Figure 7.1 and fig. 7.2 show electron and ion density plots. No clear electron density structures are observed until  $t \approx 5000 \omega_p^{-1}$  (fig. 7.1(b)). An elongation and a rotation of the electron column in the  $E \times B$  drift direction ( $-\hat{\theta}$  direction) is observed at  $t > 5000 \omega_p^{-1}$  (fig. 7.1(c), fig. 7.2). It is at this time that the instability with a clearly defined frequency is observed.

Figure 7.3 shows the time history of the potential fluctuation calculated simultaneously with fig. 7.1 and fig. 7.2. The potential fluctuation is collected at nine cells located 1 cm away from the plasma center. A clear oscillation which corresponds to the electron column rotation is observed. Figure 7.4 shows the expanded time history of the potential ( $\phi$ ) fluctuations from  $t = 8000$  to  $9000 \omega_p^{-1}$  together with  $n_e$  and  $n_i$  fluctuations. As shown in fig. 7.4(a), the  $n_e$  and  $\phi$  are in phase. This result indicates that the modified Boltzmann relation or eq. (7.3) is satisfied as we expected. The  $n_i$  and  $\phi$  are 180 degrees out of phase (see fig. 7.4(b)) indicating eq. (7.4) is satisfied. In fig. 7.5,  $\phi$  fluctuations observed in three different azimuthal locations spread 90 degrees from each other and at the same radial position ( $r = 1$  cm) are shown. From the phase delay between the signals,  $k_\theta$  is calculated to be  $m = 2$  mode rather than the  $m = 1$  mode observed in the experiments.

Figure 7.6 shows trajectories of ions from  $t = 0$  to  $2000 \omega_p^{-1}$  for  $M/m = 100$  and  $B = 32$  G. Trajectories depend on the initial ion positions. Ions which are initially

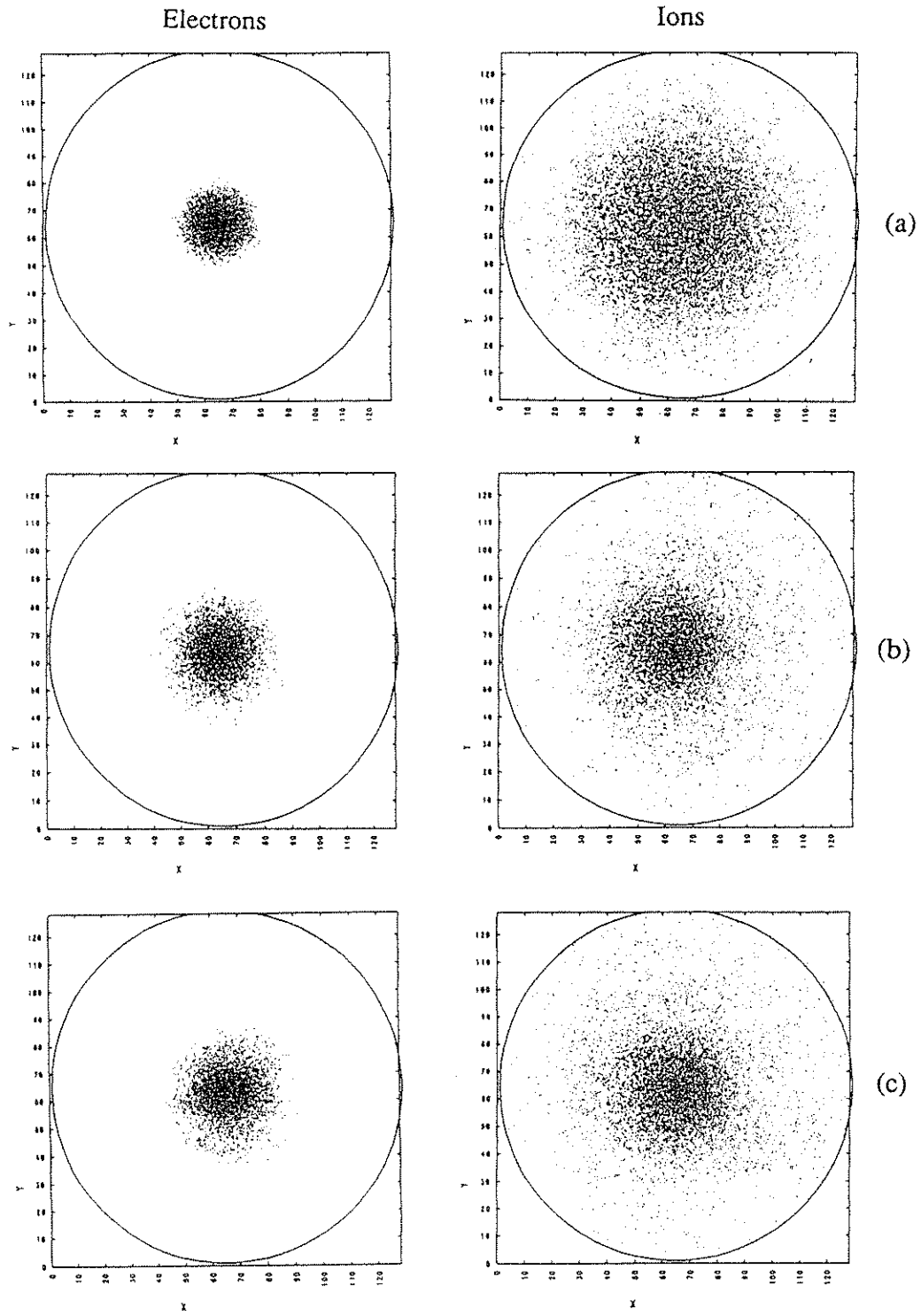


Figure 7.1: Electron and ion density plots (1). (a)  $t = 0$ , (b)  $t = 3092 \omega_p^{-1}$  and (c)  $t = 5872 \omega_p^{-1}$ .  $M/m = 800$ ,  $B = 32$  G.

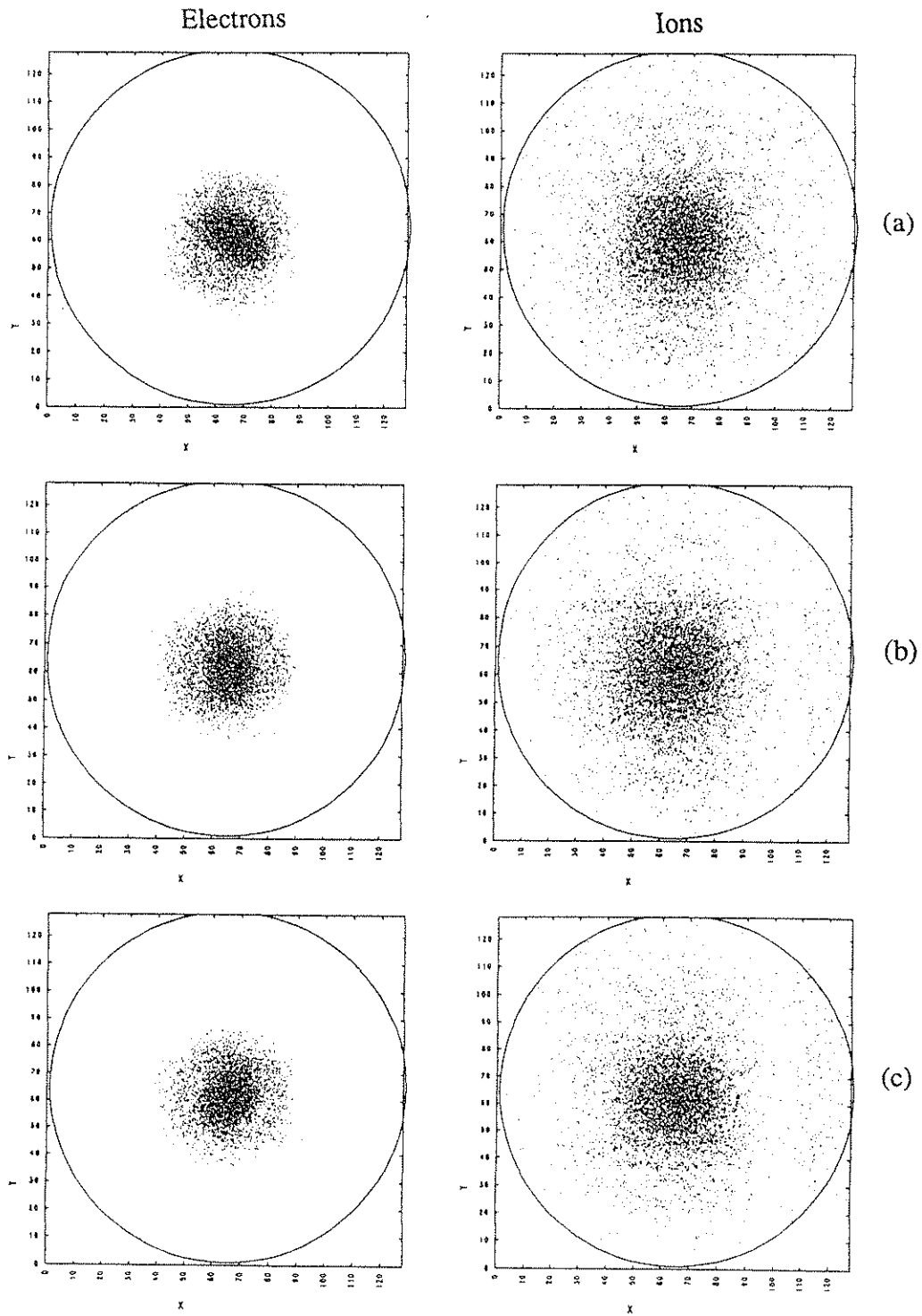


Figure 7.2: Electron and ion density plots (2). (a)  $t = 8067.6 \omega_p^{-1}$ , (b)  $t = 8109.2 \omega_p^{-1}$  and (c)  $t = 8124.8 \omega_p^{-1}$ .  $M/m = 800$ ,  $B = 32$  G.

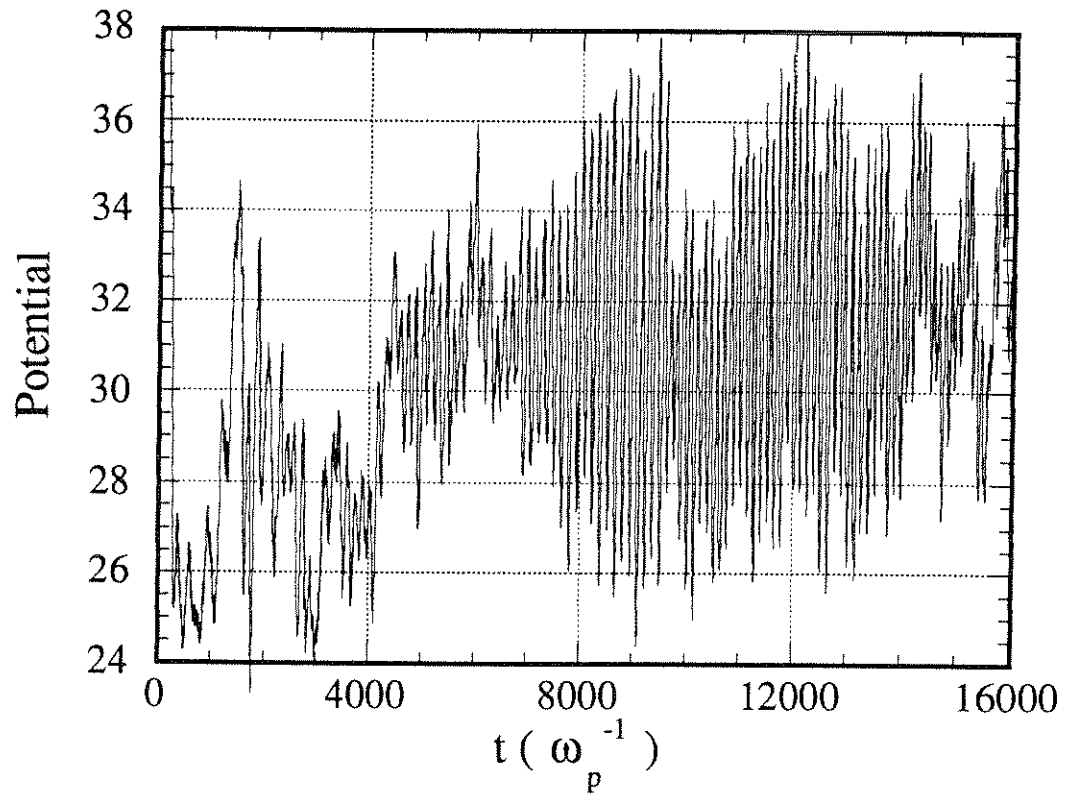


Figure 7.3: Time history of the potential fluctuation calculated simultaneously with fig. 7.1 and fig. 7.2. A clear oscillation which corresponds to the electron column rotation is observed.

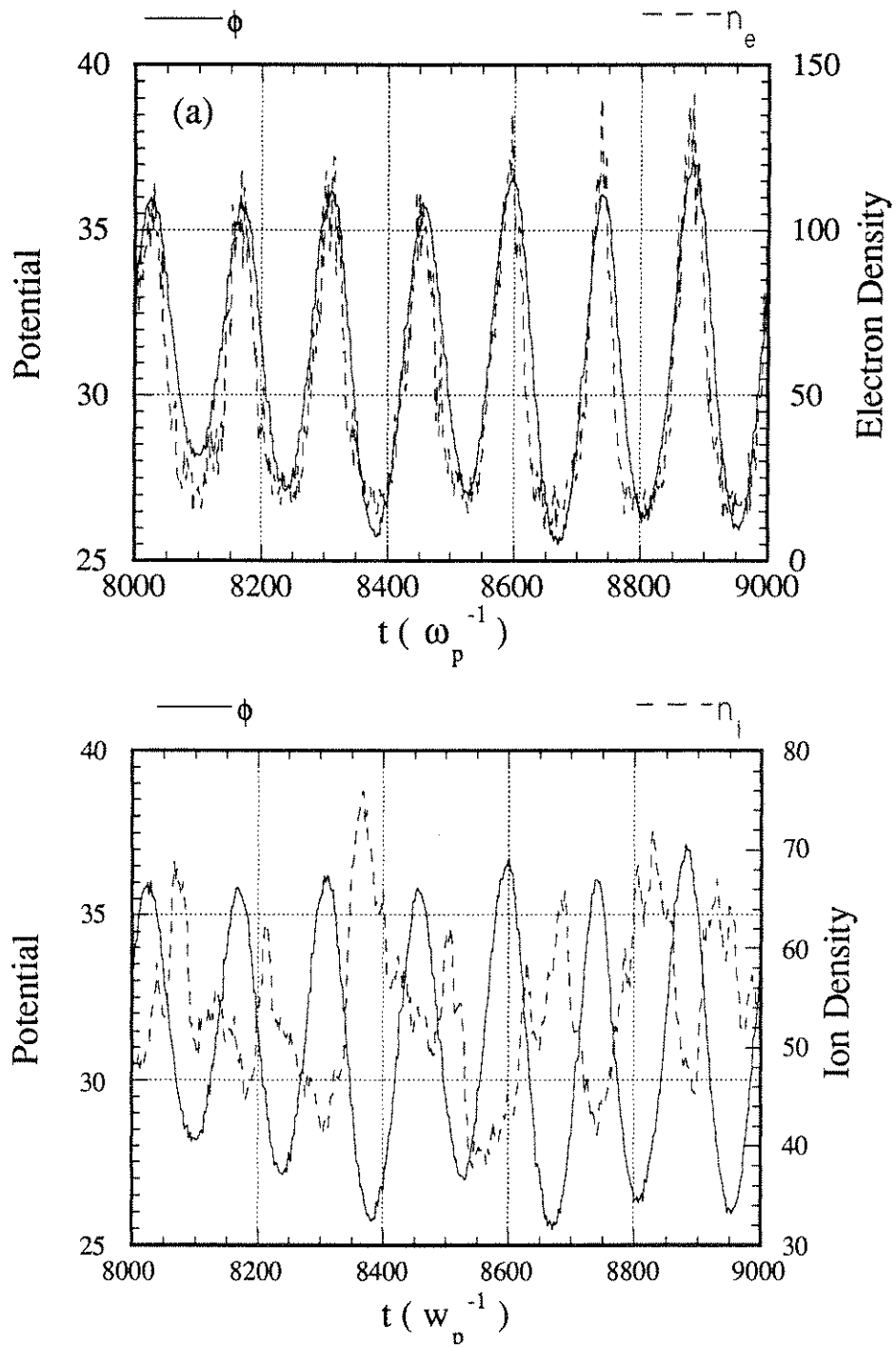


Figure 7.4: Time history of (a) electron and (b) ion density fluctuations together with the potential fluctuation. The  $n_e$  and  $\phi$  are in phase. This result indicates that the modified Boltzmann relation or eq. (7.3) is satisfied as we expected. The  $n_i$  and  $\phi$  are 180 degrees out of phase (see fig. 7.4(b)) indicating eq. (7.4) is satisfied.

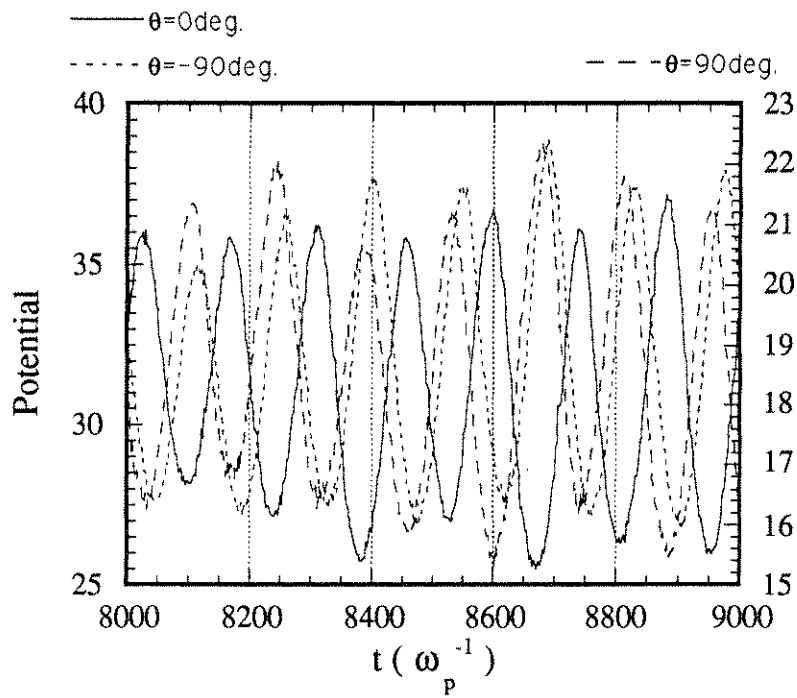


Figure 7.5: Potential fluctuations measured by three probes separated 90 degrees each other.  $k_\theta$  is calculated to be  $m = 2$  mode rather than the  $m = 1$  mode observed in the experiments.

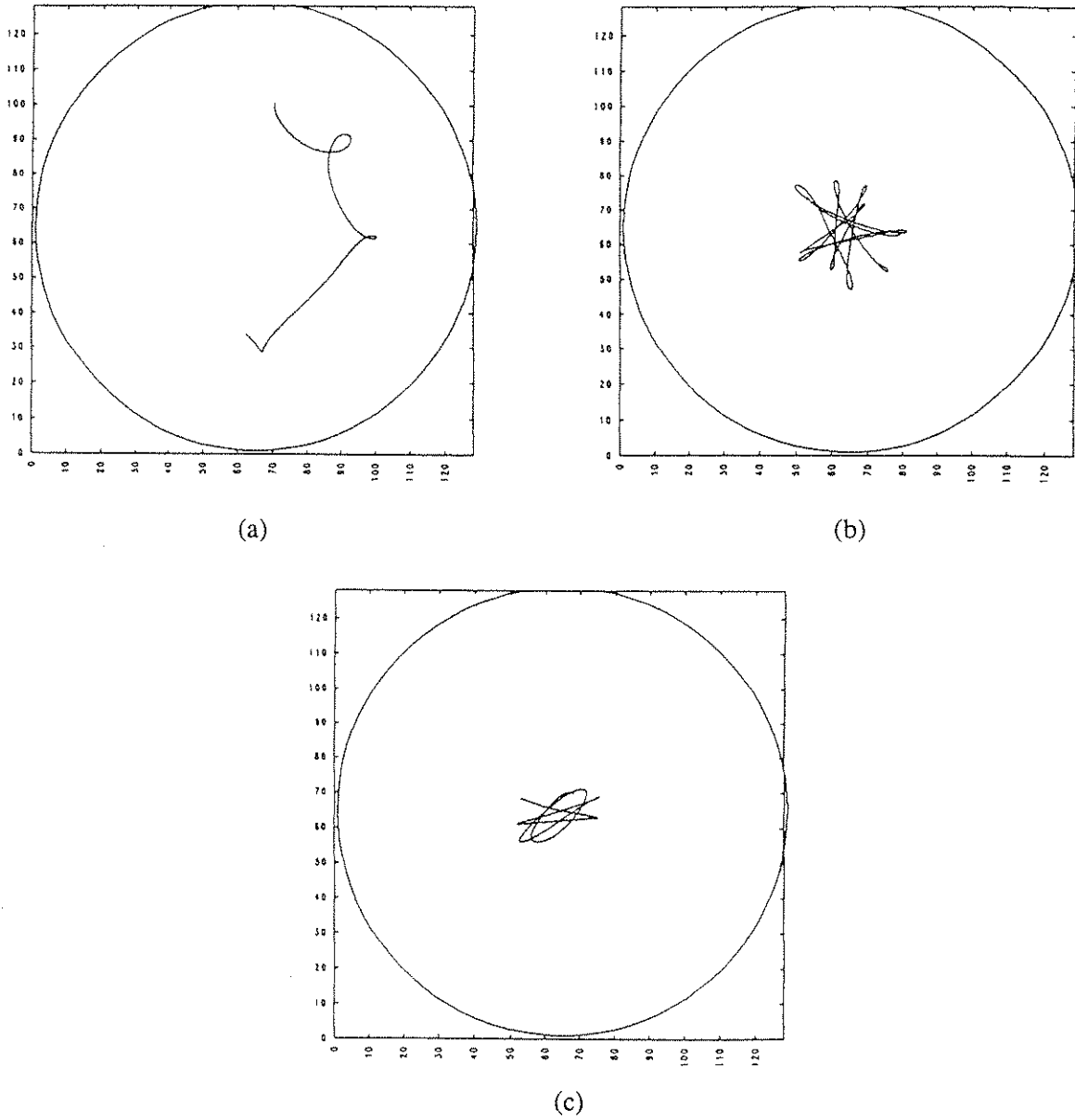


Figure 7.6: Trajectories of ions from  $t = 0$  to  $2000 \omega_p^{-1}$  for  $M/m = 100$  and  $B = 32$  G. (a) Ions which are initially at large radii where the E field is small ( $r \geq 2$  cm) do not come to the central region and no contribution to the MSHI is made. (b) Ions at the higher E field region ( $r \leq 2$  cm), however, show star shape trajectories as predicted in chapter 4. (c) An ion trajectory which starts from the star shape and ends up with a circular shape. We believe that this ion is trapped by the wave potential of the MSHI and contributes to the modulation of the MSHI.



---

|                                   |                                   |
|-----------------------------------|-----------------------------------|
| Measured Plasma rotation period   | $T_r = 160 (\omega_{pe}^{-1})$    |
| Effective ion ExB drift period    | $T_{Ei} = 294 (\omega_{pe}^{-1})$ |
| Electron ExB drift period         | $T_{Ee} = 44 (\omega_{pe}^{-1})$  |
| Electron diamagnetic drift period | $T^* = 59 (\omega_{pe}^{-1})$     |
| Electron cyclotron osc. period    | $T_{ec} = 6.3 (\omega_{pe}^{-1})$ |
| Ion plasma osc. period            | $T_{pi} = 63 (\omega_{pe}^{-1})$  |
| Ion cyclotron osc. period         | $T_{ci} = 630 (\omega_{pe}^{-1})$ |

---

Table 7.1: Measured and calculated oscillation periods

at large radii where the E field is small ( $r \geq 2$  cm) do not come to the central region and no contribution to the MSHI is made (see fig. 7.6(a)). Ions at the higher E field region ( $r \leq 2$  cm), however, show star shape trajectories (fig. 7.6(b)) as predicted in the previous section. Figure 7.6(c) shows an ion trajectory which starts from the star shape and ends up with a circular shape. We believe that this ion is trapped by the wave potential of the MSHI and contributes to the modulation of the MSHI.

Table 7.1 compares the measured plasma rotation period and the calculated plasma oscillation periods for  $M/m = 100$  and  $B = 32$  G. Since the E field and plasma potential ( $\Phi$ ) are changing in time self-consistently, we calculated the radial profiles of the E and  $\Phi$  during the steady state oscillation and used them in  $T_{E \times B e}$  and  $T_{E \times B i}$  calculations. The instability period is half the rotation period because of the instability mode number  $m = 2$ . We find that the measured instability period is closest to the effective ion  $E \times B$  rotation period and is larger than the electron  $E \times B$  period as expected.

# Chapter 8

## Conclusions

An intermediate frequency ( $f_{ci} < f < f_{ce}$ ) electrostatic instability has been observed in an electron beam produced, cylindrical plasma column. We have identified this instability as a new instability, the modified Simon-Hoh instability (MSHI), which has an instability mechanism similar to the Simon-Hoh instability (SHI). This instability can occur in a cylindrical collisionless plasma if a radial DC electric field exists and if this radial DC electric field and the radial density gradient are in the same direction. The origin of the DC electric field is found to be the difference between the ion and the electron radial density profiles. In such a plasma if the ions are essentially unmagnetized but if the electrons are magnetized, a velocity difference in the  $\theta$  direction can arise because of the finite ion Larmor radius effect. This leads to a space charge separation in the  $\theta$  direction. The consequent azimuthal electric field  $E_{\theta 1}$  and the enhancement of the density perturbation by the  $E_{\theta 1} \times B_0$  velocity occur in the same manner as in the SHI. The instability frequency is decided by the ion azimuthal drift velocity. We have

investigated this new instability through experiments, theory and 2D computer simulations.

We believe that a finite amplitude modified Simon-Hoh instability is driven modulationally unstable by ion trapping effects leading to the excitation of  $M_2$  modes and the sideband modes  $M_s$ . The final state can be a new periodic oscillation, the mode-locked state with  $f_2 = f_s = f_1/2$ . Such a periodic state is likely to be further modulationally unstable to a low-frequency  $M_3$  mode which will then migrate and perhaps mode-lock at  $f_2/2$  and so on. Thus, what at first sight appears to be a simple period doubling route of chaos follows a rather complex path starting at the low-frequency modulational end and finally mode-locking at the sub-harmonic.

There are many unanswered questions in this work. The first is how are the steady state ion and electron density profiles established? What is the ion heating mechanism that leads to the ion spreading out in the radial directions? Secondly, what exactly is the nature of the  $M_{n+2}$  modes ( $n = 0, 1, ..$ )? What is the coupling mechanisms between the daughter modes and the pump,  $M_1$  mode? These are challenging questions for future work in this area.

# Appendix A

## Observation of Other Nonlinear Evolutions of the MSHI

In this appendix, we show other nonlinear evolution of the modified Simon-Hoh instability.

### A.1 Period Doubling Sequence and Energy Exchange

In addition to  $M_1$ ,  $M_2$  and  $M_s$  modes, sometime we observe a  $M_{1/2}$  mode with a frequency  $f_1/2$ .

Figure A.1(a) shows the  $I_p$  dependence of the instability frequencies. At  $I_p = 38.9 \mu\text{A}$ , in addition to  $M_1$ ,  $M_2$  and  $M_s$  modes ( $f_1/f_2 = 2.38$ ), a new mode  $M_{1/2}$  appears at a frequency  $f_1/2$ , which is clear in fig. A.1(b). At  $I_p = 53.9 \mu\text{A}$ ,  $M_1$  and  $M_2$  are locked at  $f_1/f_2 = 2$  and merge to  $M_{1/2}$  mode. At  $I_p > 74 \mu\text{A}$ ,  $M_1$  and

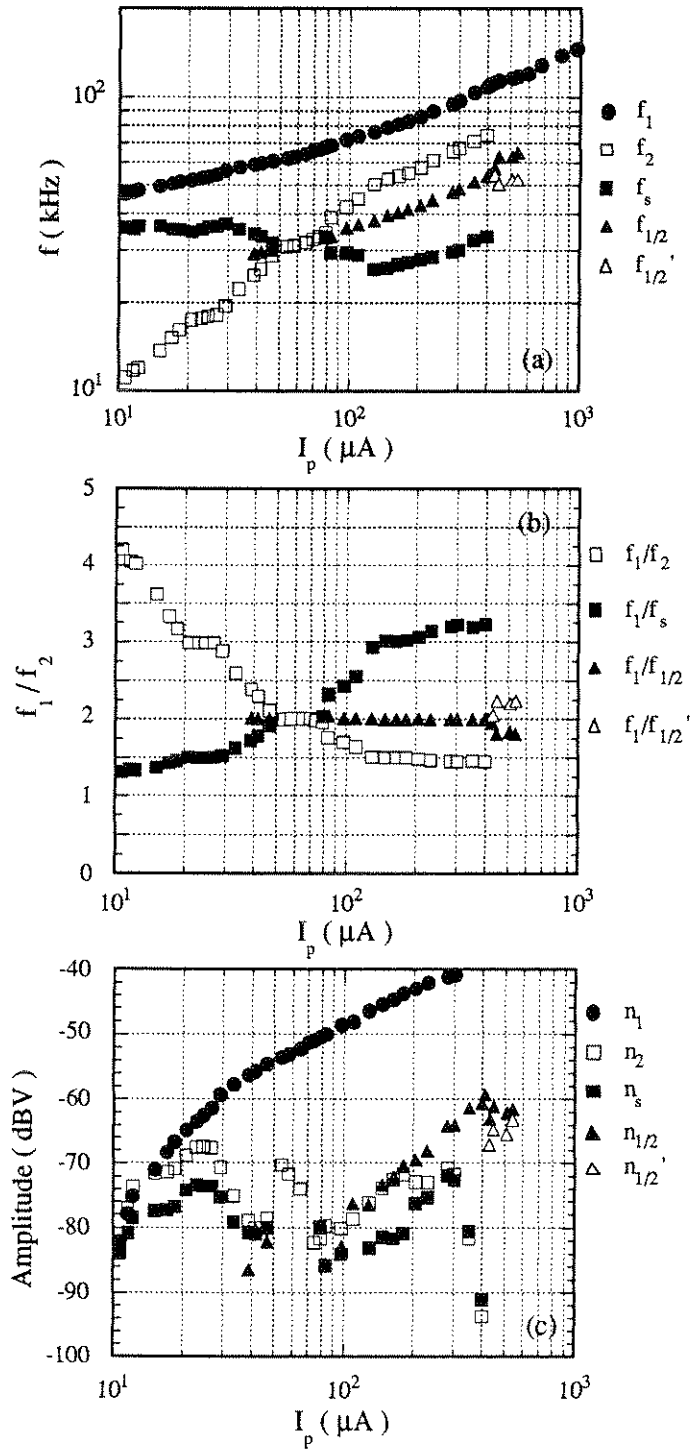


Figure A.1:  $I_p$  dependence of (a) instability frequencies, (b)  $f_1/f_2$  and (c) amplitudes. Ar  $1 \times 10^{-5}$  torr,  $r = 0.3$  cm.

$M_2$  are unlocked in frequency and  $f_2$  is now larger than  $f_1/2$ .  $M_{1/2}$  still exists with a frequency  $f_1/2$ . At  $I_p > 300 \mu\text{A}$ ,  $M_2$  and  $M_s$  mode amplitudes become smaller and disappear together at  $I_p = 410 \mu\text{A}$  (see fig. A.1(c)), while the  $M_{1/2}$  mode amplitude keeps increasing until  $I_p = 410 \mu\text{A}$ . Above this  $I_p$ ,  $M_{1/2}$  bifurcates into two modes.

In this sequence we have observed an excitation of  $M_{1/2}$  mode when  $f_2$  and  $f_s$  are getting closer to  $f_1/2$  and frequencies are unlocked. According to the nonlinear evolution which we have described in this thesis, new subharmonic components appear when a frequency locking occurs. Therefore, what we have shown above is a different nonlinear evolution of the MSHI, a period doubling sequence.

There are two groups of the subharmonics of  $f_1$ : One is  $M_{n+1}$  and  $M_{s_{n+1}}$  modes whose frequencies are  $f_{n+1}$  and  $f_{s_{n+1}} = f_1 - f_{n+1}$ , respectively ( $n = 1, 2, \dots$ ). These are the modes which we have described in this thesis. The other is  $M_{1/2^n}$  modes with frequencies  $m f_{1/2^n}$  ( $m, n = 1, 2, \dots$ ). These modes appear as a result of period doubling sequence. We have observed an energy exchange between these two groups as will be shown below.

Figure A.2 shows a sequence of the energy exchange between  $M_{n-2}$ ,  $M_{s_{n+1}}$  modes and  $M_{1/2^n}$  modes. In fig. A.2(a) we find frequency components correspond to  $f_1, f_2, f_s = f_1 - f_2, f_{1/2}, f_{1/2} - f_s, f_{1/2} + f_s$  and so on. Note that in this case, a narrow frequency locking at  $f_1/f_2 = 18/13$  occurs. In fig. A.2(b), we find new modes  $M_{1/4}$  and  $M_{3/4}$  appear at frequencies  $f_1/4$  and  $3f_1/4$ , respectively. At the transition from fig. A.2(a) to fig. A.2(b), we find that the  $M_1$  and  $M_{1/2}$  amplitudes increase (+0.8 dBV and +2.73 dBV, respectively), while,  $M_2$  and  $M_s$  amplitudes decrease (-6.0 dBV and -8.0 dBV, respectively). We believe that the main energy

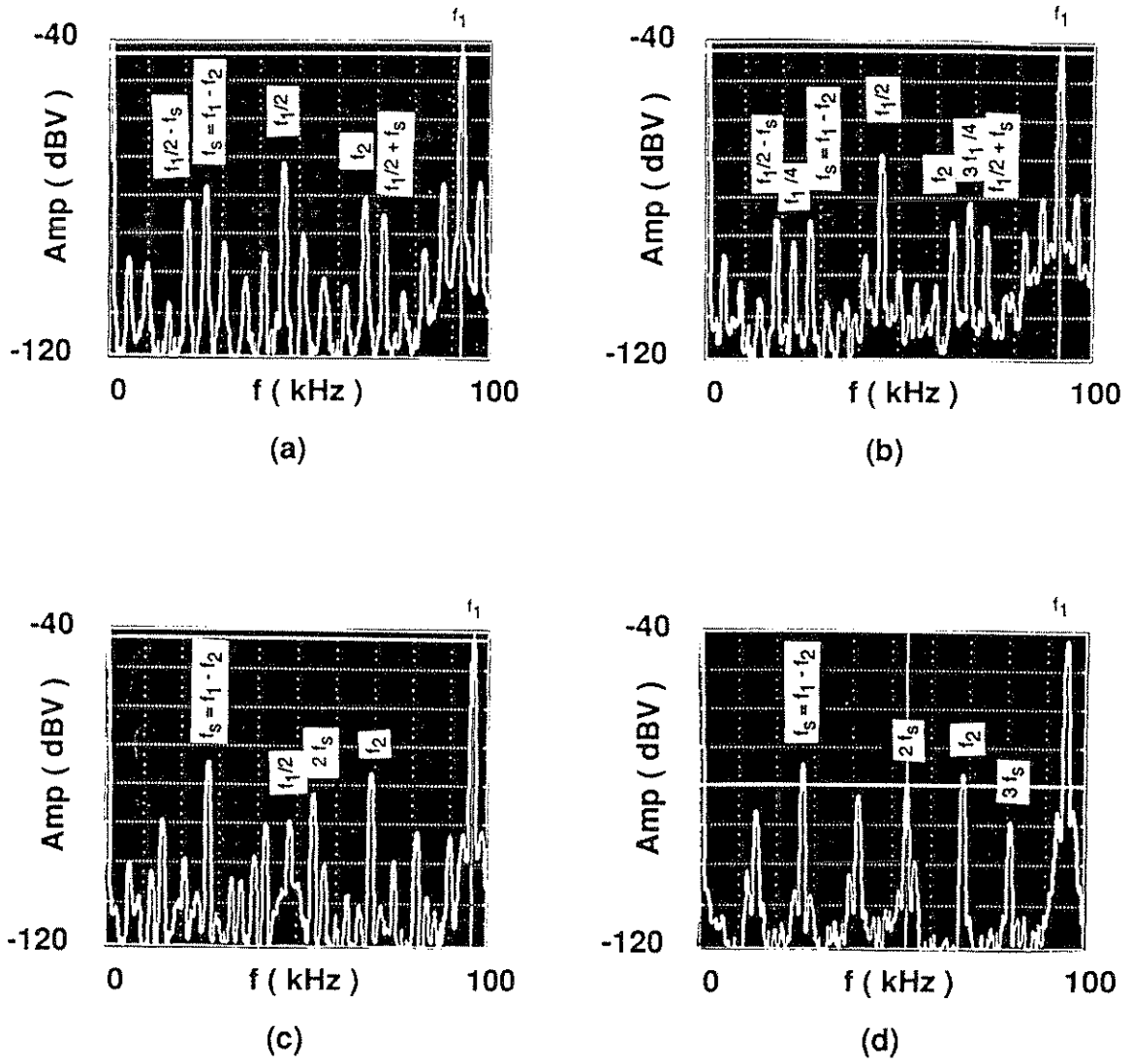


Figure A.2: A sequence of an energy exchange between  $M_{1/2n}$  mode and  $M_{n+2}$ ,  $M_{s_{n+1}}$  modes. (a)  $V_B = 200$  V,  $I_p = 210$   $\mu$ A, (b)  $V_B = 220$  V,  $I_p = 220$   $\mu$ A, (c)  $V_B = 200$  V,  $I_p = 230$   $\mu$ A and (d)  $V_B = 190$  V,  $I_p = 205$   $\mu$ A. Ar  $1 \times 10^{-5}$  torr,  $r = 0.3$  cm.

source to excite  $M_{1/4}$  and  $M_{3/4}$  is  $M_1$ . However, since  $M_2$  and  $M_s$  amplitudes decrease together with the increase in  $M_{1/2}$  amplitude, it is clear that an energy exchange from  $M_{n-2}$ ,  $M_{s_{n+1}}$  modes to  $M_{1/2n}$  modes occurs. Figure A.2(c) shows the case when the  $M_1$  amplitude decreases -0.03 dBV, the  $M_{1/4}$ ,  $M_{3/4}$  and  $M_{1/2}$  amplitudes decrease more than an order of magnitude (-15.81 dBV, -31.31 dBV and -20.25 dBV, respectively), together with a nearly an order of magnitude increase in  $M_2$  and  $M_s$  mode amplitudes (+9.65 dBV and +10.65 dBV, respectively) from fig. A.2(b). Note that the amplitudes of the  $2f_s$ ,  $3f_s$ ,  $f_1 - 2f_s$  and  $f_1 - 3f_s$  components increase  $\sim 16$  dBV. Finally in fig. A.2(d) when the  $M_1$  amplitude decreases -0.21 dBV,  $M_{1/4}$ ,  $M_{3/4}$  and  $M_{1/2}$  disappear, while  $M_2$  and  $M_s$  increase +0.02 dBV and +0.04 dBV, respectively. Therefore, we find that an energy exchange from  $M_{1/2n}$  mode to  $M_{n+2}$  and  $M_{s_{n+1}}$  modes occurs in the sequence from fig. A.2(b) to (c), (d).

## A.2 Strong Sideband Excitations

As shown in chapter 2 (see fig. 2.11 or fig. 2.13) the amplitudes of the  $f_2$  component ( $M_2$  mode) and the  $f_{s-} = f_1 - f_2$  component (the lower side band,  $M_{s-}$  mode) are more than an order of magnitude larger than the amplitude of the  $f_{s+} = f_1 + f_2$  component (the upper sideband,  $M_{s+}$  mode). In such a case, the excitation of the  $M_2$  and the  $M_{s-}$  looks like a parametric decay in a sense that the sum frequency of two main daughter modes  $M_2$  and  $M_{s-}$  is equal to the  $M_1$  mode frequency, together with the fact that sum of the azimuthal mode numbers of these daughter modes is that of the  $M_1$  mode. However, at some experimental conditions, we



observe a strong excitation of the upper and the lower sidebands modes ( $M_{s_+}$  and  $M_{s_-}$  modes, respectively) but a very weak excitation of the  $M_2$  mode. Figure A.3 shows a sequence of an excitation of the sideband modes for an Ar pressure scan. The experiments are conducted with a plasma length of 17 cm (a movable 5.5 cm in diameter endplate located at 17 cm from the gun). The unbiased probe placed at  $z = 1$  cm from the gun and  $r = 0.2$  cm is used for the measurements. In fig. A.3(a) we find only a coherent  $M_1$  mode. Small-amplitude components at  $f = 34$  kHz and 70 kHz are not signals but pick up noises. When we decrease the pressure  $P$ , the lower and the upper sidebands appear (fig. A.3(b)). Note that the amplitude of the  $M_2$  mode is at the noise level and  $\sim 15$  dBV lower than the amplitude of the  $M_{s_-}$  mode. In fig. A.3(c), we find that not only the first upper and the lower sidebands ( $f_1 \pm f_2$ ) but also the second sidebands ( $f_1 \pm 2f_2$ ) are getting larger. In fig. A.3(d), the amplitudes of the  $f_1 \pm f_2$  and  $f_1 \pm 2f_2$  components are even larger than the amplitude of the  $f_1$  component. At  $P = 8.4 \times 10^{-6}$  torr, we find the  $f_1 \pm nf_2/2$  components as shown in fig. A.3(e).

In this sequence the amplitude of the  $M_2$  mode is much smaller than the upper and the lower sidebands (see fig. A.3(c)). Therefore, we don't think that the parametric decay scenario, which is described as the decay of  $M_1$  mode into  $M_2$  and  $M_{s_-}$  modes, is the proper mechanism. A strong excitation of both upper and the lower sidebands indicates a modulational instability. In this case, the  $\epsilon_2$  term in the mode coupling equation (eq. (6.4)) should be replaced by the  $\epsilon_{s_+}$  term, the dielectric function of the upper sideband.

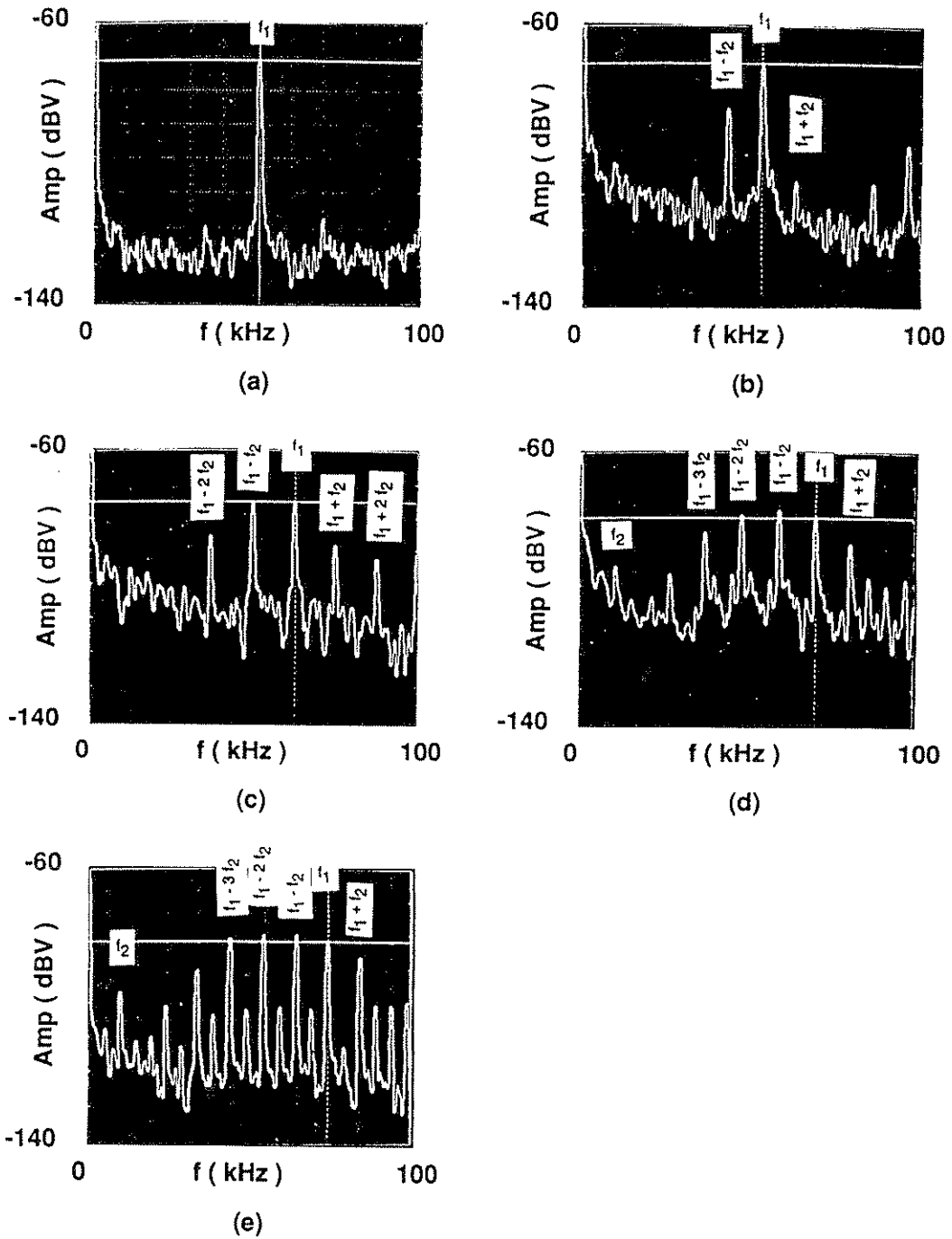


Figure A.3: Ar pressure dependence of a sequence of an excitation of the sideband modes. (a)  $P = 5.2 \times 10^{-5}$  torr, (b)  $P = 4.2 \times 10^{-5}$  torr, (c)  $P = 2.5 \times 10^{-5}$  torr, (d)  $P = 1.4 \times 10^{-5}$  torr and (e)  $P = 8.4 \times 10^{-6}$  torr. The plasma length is 17 cm,  $I_p = 25 \sim 34 \mu\text{A}$ . The unbiased probe is located at  $r = 0.2$  cm and  $z = 1$  cm from the gun.

# Bibliography

- [1] F. F. Chen, Electric Probes, in *Plasma Diagnostic Techniques*, Chap. 4, edited by R. H. Huddlestone and S. L. Leonard (Academic Press, N.Y., 1965)
- [2] S. C. Brown, *Basic Data of Plasma Physics*, (MIT Press, Cambridge, MA, 1966)
- [3] J. W. Sheldon, Phys. Rev. Lett. 8, 64 (1962)
- [4] F. F. Chen, *Introduction to Plasma Physics and Controlled Fusion*, 2<sup>nd</sup> edition, (Plenum Press, N.Y., 1984)
- [5] R. L. Stenzel, R. Williams, R. Agüero, A. Ling, T. McDonald. and J. Spitzer, Rev. Sci. Instrum. 53, 1027 (1982)
- [6] F. F. Chen, private communication
- [7] W. D. Getty and L. D. Smullin, J. Appl. Phys. 34, 3421 (1963); H. J. Hopman, T. Matitti and J. Kistemaker, Plasma Phys. 10, 1051 (1968); J. R. Apel, Phys. Fluids 12, 291 (1969); R. J. Briggs *Electron Stream Interaction with Plasmas* (MIT Press, Massachusetts, 1964)

- [8] T. Matitti, H. J. Hopman and A. Vermeer, *Proc. Eighth Int. Conf. on Ionization Phenomena in Gases*, 383 (1967)
- [9] A. Vermeer, T. Matitti, *Plasma Phys.* 9, 241 (1967)
- [10] K. Papadopoulos and P. Palmadesso, *Phys. Fluids* 19, 605 (1976)
- [11] Y. Kitagawa, T. Maekawa and S. Shigetoshi, *J. Phys. Soc. Jpn.* 41, 1041 (1976)
- [12] M. Yamada and D. K. Owens, *Phys. Rev. Lett.* 27, 1529 (1977)
- [13] D. N. Wall, P. H. Edglaey and R. N. Franklin, *Plasma Phys* 23, 145 (1981)
- [14] R. B. Boswell, *Plasma Phys. Cont. Fusion* 27, 405 (1985)
- [15] N. A. Krall and P. C. Liewer, *Phys. Rev.* A4, 2094 (1971)
- [16] E. Ott, J. B. McBride, J. H. Orens and J. P. Boris, *Phys. Rev. Lett* 28, 88 (1972)
- [17] A. Hirose and I. Alexeff, *Nuclear Fusion* 12, 315 (1972)
- [18] A. M. Fridman, *Sov. Phys. DOKLADY* 9, 75 (1964)
- [19] A. Simon, *Phys. Fluids* 6, 382 (1963)
- [20] F. C. Hoh, *Phys. Fluids* 6, 1184 (1963)
- [21] K. I. Thomassen, *Phys. Fluids* 9, 1836 (1966)
- [22] B. B. Kadomtsev, *Plasma Turbulence*, (Academic Press, N.Y., 1965)

- [23] P. K. Kaw, private communication
- [24] S. Ichimaru, *Basic Principles of Plasma Physics*, (W. A. Benjamin, Inc., Massachusetts, 1973)
- [25] N. A. Krall and A. W. Trivelpiece, *Principles of Plasma Physics*, (McGraw-Hill Book Co., 1973)
- [26] A. Simon, *Physical Review* 98, 317 (1955)
- [27] W. E. Drummond and M. N. Rosenbluth, *Phys. Fluids* 5, 1507 (1962)
- [28] G. A. Paulikas and R. V. Pyle, *Phys. Fluids* 5, 333 (1962)
- [29] B. B. Kadomtsev and A. V. Nedospasov, *J. Nucl. Energy* C1, 230 (1960)
- [30] S. Q. Mah, H. M. Sharsgard, and A. R. Strilchuk, *Phys. Rev. Lett.* 16, 1409 (1970)
- [31] M. Yamada, H. W. Hendel, S. Seiler and S. Ichimaru, *Phys. Rev. Lett.* 34, 650 (1975)
- [32] M. Yamada and D. K. Owens, *Phys. Rev. Lett.* 27, 1529 (1977)
- [33] M. Yamada and H. W. Hendel, *Phys. Fluids* 21, 1555 (1978)
- [34] S. Ichimaru, *J. Phys. Soc. Jpn.* 39, 1373 (1975)
- [35] W. L. Kruer, J. M. Dawson and R. N. Sudan, *Phys. Rev. Lett.* 23, 838 (1969)
- [36] M. V. Goldman, *Phys. Fluids* 13, 1281 (1970)

- [37] M. J. Alport, S. L. Cartier, and R. L. Merlino, *J. Geophys. Res.* 91, 1599 (1986); M. J. Alport and E. G. Van Nieker, *Proc. of the Workshop on the Current-Driven Electrostatic Ion-cyclotron Instability*, 106, edited by R. W. Schrittieser, (World Scientific, Singapore, 1988)
- [38] V. E. Zakharov, *Soviet Physics JETP* 35, 908 (1972)
- [39] see for example; H. L. Swinney, *Physica* 7D, 3 (1983)
- [40] G. Rosenthal, Ph. D. Thesis, University of California Los Angeles, 1991